이학박사 학위논문

플라즈모닉 귀금속 나노구조물의 합성 및 광학적 응용

Synthesis and Optical Application of

Plasmonic Noble Metal Nanostructures

2020 년 8 월

서울대학교 대학원

화학부 물리화학 전공

김 준 기

A Ph. D. Dissertation

Synthesis and Optical Application of

Plasmonic Noble Metal Nanostructures

By Joon Ki Kim

Supervisor: Professor Du-Jeon Jang

Major: Physical Chemistry

Department of Chemistry

Graduate School of Seoul National University

August 2020

Table of Contents

Appendices   153

Abstract (Korean)   157

Abstract of dissertation

In this dissertation, synthesis and optical application of plasmonic noble metal nanostructures are mainly discussed. Various methods to fabricate core-shell, nanoshells, nanospike, and nanoparticle arrays structures have been investigated. The optical and morphological properties of as-prepared nanostructures have been also studied by using UV/vis spectroscopy, Raman spectroscopy, and electron microscopy. A brief overview on preparation methods and the plasmonic resonance of noble metal nanostructures are presented in Chapter 1.

Chapter 2 presents the metal-enhanced fluorescence (MEF) of gold nanoclusters adsorbed onto Ag@SiO$_2$ core-shell nanoparticle. The static and time-resolved MEF of Au$_{25}$-adsorbed Ag@SiO$_2$ core-shell nanoparticles (NPs) has been studied systematically with variation of shell thicknesses, core sizes, and excitation wavelengths. The emission of Au$_{25}$-adsorbed Ag@SiO$_2$ NPs is blue-shifted and highly enhanced compared with that of free Au$_{25}$ clusters. The photoluminescence (PL) intensity of Au$_{25}$-adsorbed Ag@SiO$_2$ NPs is higher as much as 7.4 times than that of free Au$_{25}$ clusters. The increase of the radiative decay rate constant with separation is identical to that of PL enhancement, suggesting that the MEF of Au$_{25}$-adsorbed Ag@SiO$_2$ NPs arises from the increase of the radiative decay rate constant induced by the near-field enhancement of plasmonic Ag NPs.

Chapter 3 describes the fabrication of hollow and bumpy Au (HBA) NSs with rough surfaces using expanded silica mesopores as templates. Because some Au seeds were

located at the inner surfaces of silica mesopores, produced Au NSs have inherent inward-grown nanobumps. During seven successive reduction steps, the LSPR peak of Au nanostructures shifted progressively toward a longer wavelength as the sizes of Au seeds increased gradually. Measuring the cross-sections of HBA NSs milled by a focused ion beam, we have found that hollow and bumpy nanostructures arose from the pore structures of mSiO$_2$ NPs. HBA NSs confine Raman-probe molecules well owing to their hollow structures and have ragged surfaces due to their inward-bumpy morphologies, exhibiting highly efficient surface-enhanced Raman scattering activity.

Chapter 4 presents the fabrication of genuinely hollow Au nanourchins (HANUs) using SiO$_2$ NPs as hard templates. Ag-SiO$_2$ NPs were fabricated via amine-assisted reduction. Then, Au nanourchins (ANUs) were synthesized by the galvanic replacement reaction of Ag-SiO$_2$ NPs using L-3,4-dihydroxyphenylalanine (DOPA) as a reductant and a capping agent. The silica cores of ANUs were etched using HF*(aq)* to produce HANUs. Measuring cross sections, we have found that HANUs have well-defined hollow morphologies. Compared with nanourchins made via DOPA-mediated reduction, HANUs hardly contain residual silver because very tiny silver seeds were used as the initiation sites of galvanic replacement. HANUs have revealed large surface-enhanced Raman scattering enhancement and a significant photothermal effect under a weak illumination.

Chapter 5 describes that highly dense plasmonic silver NP arrays have been fabricated by laser-induced dewetting of commercially available silver paste as a starting bulk material. The first laser-scan mode has produced unprecedented intermediate structures, so called laser-induced fine silver nanostructures (LIFSNs) while the second laser-scan

mode has transformed LIFSNs into plasmonic silver NP arrays via the dewetting of the priorly formed nanostructures. The laser-induced fabrication of silver NP arrays has been found to be very sensitive to distance from secondly irradiated laser pulses, suggesting that the fine control of laser intensity is very important. As-prepared silver NP arrays have generated numerous hot spots to show highly strong surface-enhanced Raman scattering signals.

List of figures and tables

Figure 2-6. Extinction (dotted) and emission spectra (solid) of 50 nm silver NPs (blue) and BSA-capped Au_{25} clusters (red) suspended in water. The sample was excited at 355 nm for the emission spectrum.

Figure 2-7. PL spectra of Au_{25}-absorbed $Ag@SiO_2$ NPs suspended in water with excitation at 355 nm. The shell thickness of silica in the unit of nm is indicated near each spectrum, while 'free' stands for free Au_{25} clusters without $Ag@SiO_2$ NPs.

Table 2-1. Emission decay constants of free Au_{25} clusters and Au_{25}-adsorbed $Ag@SiO_2$ NPs with various silica shell thicknesses.

Figure 2-8. (a) $\Delta\lambda$ (= λ_{free} - λ_{NP}) as a function of separation between Au_{25} clusters and Ag NPs, where λ_{free} and λ_{NP} are the wavelengths at the PL maxima of Au_{25} clusters without and with $Ag@SiO_2$ NPs, respectively. The solid line is the best-fitted curve of $\Delta\lambda_0 \cdot \exp(-d/\delta)$; $\Delta\lambda_0$ and δ have been estimated as 21.5 and 18.5 nm, respectively, and $\Delta\lambda_0$ has been used to yield ΔE_0 of 67 meV. (b) PL enhancement factors (squares) of Au_{25}-absorbed $Ag@SiO_2$ NPs as a function of separation between Au_{25} clusters and Ag NPs. The solid and dashed lines are the curves best-fitted to $(\alpha + \beta d)^6$ and $(\alpha + \beta/d^3)$, respectively; the fitting details are provided in Table 2-2

Table 2-2. The fitting details of the PL enhancement factor of Au_{25}-adsorbed $Ag@SiO_2$ NPs as a function of separation between Au_{25} clusters and Ag NPs.

Figure 2-9. Emission decay profiles of indicated free Au_{25} clusters and Au_{25}-adsorbed $Ag@SiO_2$ NPs suspended in water, monitored at 550+ nm after excitation at 355 nm. Solid lines are best-fitted curves to extract kinetic constants.

Figure 2-10. (a) PL enhancement factors (circles) and lifetimes (squares) of Au_{25}-absorbed $Ag@SiO_2$ NPs as a function of separation. Note that the values at ∞ were obtained from free Au_{25} clusters. (b) PL enhancement factors (circles) and $(k_r + k_{rm})/k_r$ values (crosses) of Au_{25}-absorbed $Ag@SiO_2$ NPs as a function of the separation.

Figure 2-11. Contour plot for the PL enhancement factors of Au_{25}-adsorbed $Ag@SiO_2$ NPs

as functions of the separation and the excitation wavelength.

Figure 2-12. TEM images of Ag NPs with diverse average diameters indicated inside. Each scale bar indicates 50 nm.

Table 2-3. Diameters and extinction λ_{max} values of Ag NPs prepared at various concentrations of sodium citrate and tannic acid.

Figure 2-13. PL enhancement factors, with excitation at 355 nm, of Au_{25}-adsorbed $Ag@SiO_2(0)$ NPs as a function of the diameter of Ag NPs. The red line represents the best-fitted Gaussian curve, whose maximum is located at 90 nm.

Figure 2-14. Sensing selectivity of Au_{25}-adsorbed $Ag@SiO_2(6)$ NPs for Cu^{2+} over other heavy metal ions. The concentrations of the respective metal ions were 20 μM, and samples were excited at 370 nm. The gray bars stand for the PL intensities of free Au_{25} clusters while the red bars stand for the PL intensities of Au_{25}-adsorbed $Ag@SiO_2(6)$ NPs.

Figure 2-15. Sensing selectivity of Au_{25}-adsorbed $Ag@SiO_2(0)$ NPs for Cu^{2+} over other heavy metal ions. The concentrations of the respective metal ions were 20 μM, and samples were excited at 370 nm. The gray bars stand for the PL intensities of free Au_{25} clusters while the red bars stand for the PL intensities of Au_{25}-adsorbed $Ag@SiO_2(0)$ NPs.

Figure 3-1. (a) Schematic illustration for the fabrication of pore-expanded $mSiO_2$ NPs. (b,c) TEM images of (b) $mSiO_2$ NPs and (c) pore-expanded $mSiO_2$ NPs. The scale bar in the inset of Figure 3-1c indicates 50 nm.

Figure 3-2. (a) N_2 adsorption/desorption isotherms of pore-expanded $mSiO_2$ NPs, where closed and open circles correspond to adsorption and desorption points, respectively. (b) Pore-size distribution plot corresponding to the N_2 adsorption/desorption isotherm of pore-expanded $mSiO_2$ NPs.

Figure 3-3. (a) HRTEM image of Au-$mSiO_2$ NPs. (b) Size-histogram of Au seed in Au-$mSiO_2$ NPs. (c) UV-vis absorption and (d) XRD data of (black) mSiO2 NPs and (red) Au-

mSiO$_2$ NPs.

Figure 3-4. (a) Schematic illustration for the fabrication of HBA NS. (b-f) TEM images of progressively growing (b) mSiO$_2$ NPs, (c) Au-mSiO$_2$ NPs, (d) growth intermediates, (e) Au NSs, and (f) HBA NSs. (g) SEM image of HBA NSs. Each scale bar indicates 100 nm.

Figure 3-5. (a) UV-vis extinction spectra of Au NPs synthesized by (blue) the conventional method and (red) our sequential reduction method. (b) TEM image of irregular Au NPs synthesized by the conventional method.

Figure 3-6. (a) Extinction spectra measured at successive steps during the growth reaction of Au NSs. (b) UV-vis extinction spectra of (i) Au-mSiO$_2$ NPs, (ii) step-1 NPs, (iii) step-4 NPs, (iv) Au NSs, and (v) HBA NSs.

Figure 3-7. TEM images of progressively growing Au NSs. Each scale bar indicates 100 nm.

Figure 3-8. Particle size-distribution histograms of respectively indicated samples.

Figure 3-9. (top) HADDF-STEM image and EDX elemental map of a HBA NS. (bottom) Line-scanned elemental profiles of HBA NS.

Figure 3-10. Cross-section SEM images of (a,b) Au NSs and (c,d) HBA NSs obtained by the focused-ion-beam milling method.

Figure 3-11. TEM image of inward grown Au nanotips in mesoporous silica NPs.

Figure 3-12. (a) SERS spectra of 10 μM R6G(*ethanol*) adsorbed on HBA NSs, Au NSs, Au NPs, and Si. Note that 0.10 M R6G(*ethanol*) was used to record the Raman signal of the Si substrate. (b) The SERS enhancement factors of HBA NSs acquired via measuring relatvie Raman intensities at 1382 cm^{-1}. (c) SERS sepctra of R6G at concentrations ranging from 10^{-8} M to 10^{-3} M   (d) SERS intensity of R6G at 1382 cm^{-1} as a function of the logarithm of the R6G concentration. The inset shows a representative optical image of a HBA NSs-R6G SERS substrate on a Si piece (scale bar: 1 cm).

Figure 5-6. SEM images elucidating (a) laser melting, (b) laser dewetting, and (c) laser ablation, induced by nanosecond-laser irradiation. (d) Magnified SEM image of silver particles created from laser dewetting.

Figure 5-7. (a) SEM image of a laser-scanned silver paste film, where yellow arrows indicate scanned directions. (b) Schematic showing the laser-sanning process, where a laser beam with 6 ns pulses of 1.3 J/cm^2 was scanned on the film at a rate of 50 μm/s. SEM images of (c) the spot **i**, (d,e) the spot **ii**, (f) the spot **iii**, and (g,h) the spot **iv**.

Figure 5-8. (a) SEM image of a crossly line-scanned silver paste film (yellow arrows: scan directions). (b,c) SEM image of the spot **i**. (d.e) SEM image of the spot **ii**.

Figure 5-9. SEM images of silver nanostructures formed at the spot **v** of Figure 5-8.

Figure 5-10. (top) Spatial energy distribution of a nanosecond laser pulse and SEM image of a silver paste film bearing LIFSNs, which was irradiated again with a single laser pulse in the middle. (bottom) SEM images measured at the respectively indicated positions.

Figure 5-11. Low-magnified SEM image of silver nanostructures formed at the spot **iii** of Figure 5-10.

Figure 5-12. (top) SEM images with particle size-distribution histograms and (bottom) electric-field intensity distributions, calculated numerically by using the finite-difference time-domain method, of Ag NP arrays obtained by cross line scanning at rates of (left) 50 and (right) 200 μm/s. Each scale bar indicates 100 nm.

Figure 5-13. SEM images of Ag NP arrays formed by cross line scanning at rates of (a) 5 and (b) 20 μm/s. Insets: Particle size-distribution histograms of Ag NP arrays.

Figure 5-14. (a) Raman signals of R6G adsorbed on the spots **i**, **ii**, and **iii** of Figure 5-15. (b) Raman signals of R6G adsorbed to Ag NP arrays on the spot **iii**. The samples were excited at 532 nm, and the concentration of R6G is indicated near each spectrum.

Figure 5-15. SEM image of a crossly line-scanned silver paste film.

Figure 5-16. Real images of fishnet-likely scanned silver paste films on (a) a glass plate, (b) a PET sheet, and (c) a paper slip. The areas **i** and **ii** of the panel **a** indicate laser-scanned and pristine silver paste films, respectively. (d) SEM image of the laser-scanned area. (e) Magnified SEM image of the spot **iii** in the panel **d** with a size-distribution histogram. (f) Hyperspectral Raman mapping of the spot **iii**. (g) Raman intensity distribution with standard deviations of 19.1% on the spot **iii**.

Figure 5-17. Absorption spectrum of a fishnet-likely scanned silver paste film on a glass plate (the area **i** of Figure 5-16a). Inset: optical microscope image of the paste film.

Figure 5-18. SEM images of (a) pristine and silver paste films conventionally sintered at (b) 300, (c) 500, and (d) 700 ºC.

Chapter 1. General introduction

1.1. Preparation of noble metal nanostructures
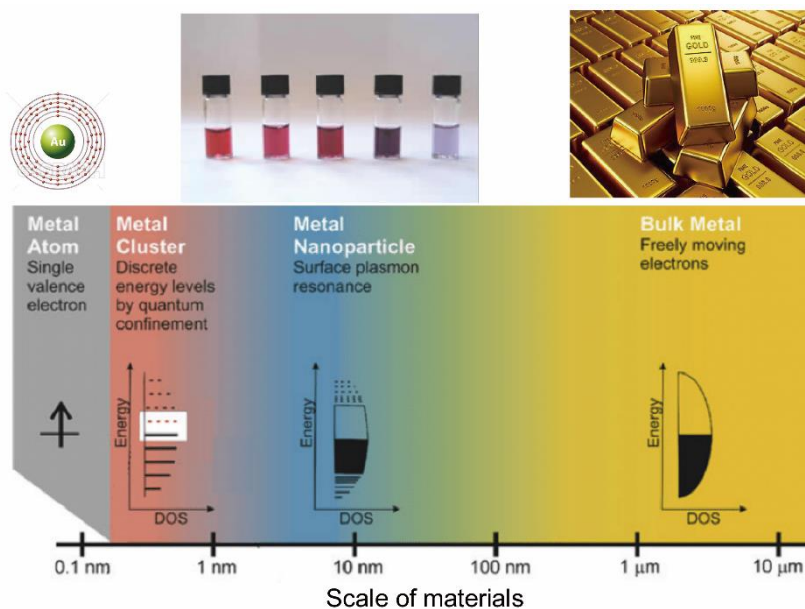
Figure 1-1. The size-effect on metal materials. While bulk metal and metal nanoparticles have a continuous band of energy levels, metal clusters having the confined number of atoms results in discrete energy levels. Reproduced from ref. 3

Various nanostructures having distinct functional properties have been widely studied recently.[1-5] As semiconductor materials become smaller in nano-size, it can be synthesized in the form of quantum dot emitting light. As size of metal materials decreases, it may have a low melting point below 200 °C.[6] In addition, dielectric materials generally have a maximum dielectric constant of 1 micrometer-size or less. Since these properties are very different depending on the size and shape of nanostructures, it is very important to study the morphological properties for nanochemistry (Figure 1-1). In particular, noble metal nanoparticles (NPs) attract scientific potential because they can be used in diverse and

wide applications such as surface-enhanced Raman spectroscopy (SERS), catalysts, devices, and diagnostic biological probes.[7-10] Morphology and size provide important factors over many of the physical and chemical properties of nanomaterials.
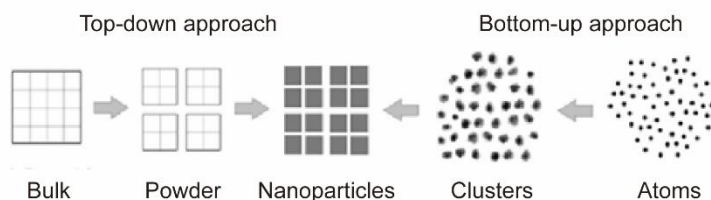
Figure 1-2. The illustration scheme of nanoparticles synthesis by top-down and bottom-up methods.

A variety of synthesis methods have been reported for preparing noble metal nanostructures. These can be broadly classified into two categories; (i) top-down and (ii) bottom-up approach (Figure 1-2).[6] The top-down method carves nanostructures by confined etching of large and bulk materials. In top-down nanofabrication, nanoscale features are fabricated via commonly lithographic techniques; optical, electron, or ion beam lithography. However, these techniques have various disadvantages. One of the alternative methods for producing nanostructures is laser-induced heating via laser-direct-writing (LDW) processing.[11-14] This processing is based on the photothermal effect induced by a laser pulse that offers a confined area with high temporal and spatial accuracy. Several laser process parameters, such as laser beam fluence, laser pulse width, and scan rate can be considerable. This processing has advantage on high process rate and special accuracy, allowing precise and fast fabrication of the desired material. As laser-induced

heat can be confined to a specific area, it is possible to selectively anneal the desired part or area without any thermal side effect with the substrates and adjacent nanostructures.

In bottom-up method, the common method is chemical reduction of soluble metal salts.[1-2] The fabrication of NPs makes use of a metal ion salts, reducing agents, and stabilizing or capping agents. The stabilizing agent adsorbs the NPs and prevent further growth of specific facet. The control of crystal lattice planes of noble metal NPs has become important factor for surface modification, passivation, and morphological parts arising from the surface plasmon resonance (SPR) effects. Polymer, organic compound, and proteins also bind to the NPs' surface and thus serve the role of stabilizer. Many NPs can be fabricated with a pretty good degree of shapes and sizes. A number of morphologies including cubes, belts, triangle, and stars can be generated by chemical reduction method. The interest of nanoscience now shifts to the preparation of more complex morphologies such as core-shell and hollow forms for various application. Hollow structures, a class of NPs with empty spaces inside solid shells, have greatly attracted attention because of their unique properties associated with the hollow morphology. Hollow NPs can be employed as nano-containers to load pharmaceutical compounds, proteins, and DNA. Also, plasmon resonances of noble metal NSs can be effectively tuned to a wavelength ranging from the visible to the infrared region by varying the ratio of cavity diameter to metallic shell thickness.[15-18]

Recently, many intensive techniques are available to prove the morphology of NPs and overall composition. Advanced characterization techniques for NPs include scanning electron microscopy (SEM), high-resolution transmission electron microscopy (HRTEM),

focused ion-beam (FIB) milling, energy-dispersive X-ray spectroscopy (EDX), X-ray photoelectron spectroscopy (XPS) but also traditional method such as UV/vis spectroscopy, infrared spectroscopy, X-ray diffraction (XRD), Brunauer-Emmett-Teller (BET) analysis, and Raman spectroscopy.

1.2. Surface plasmons on noble metal nanoparticles

Surface-enhanced Raman scattering (SERS) can have an ultrahigh sensitivity down to the single-molecule level by using noble metal NPs. The SERS effect is owing to the enhancement of Raman signal of analytes by several orders of magnitude when the Raman probes are located at close to noble metal NPs.[8] The enhancement of Raman signal strongly due to the surface plasmon resonance (SPR) properties of noble metal NPs, which can strong amplify the local electromagnetic field because of the excitation of SPR (Figure 1-3).
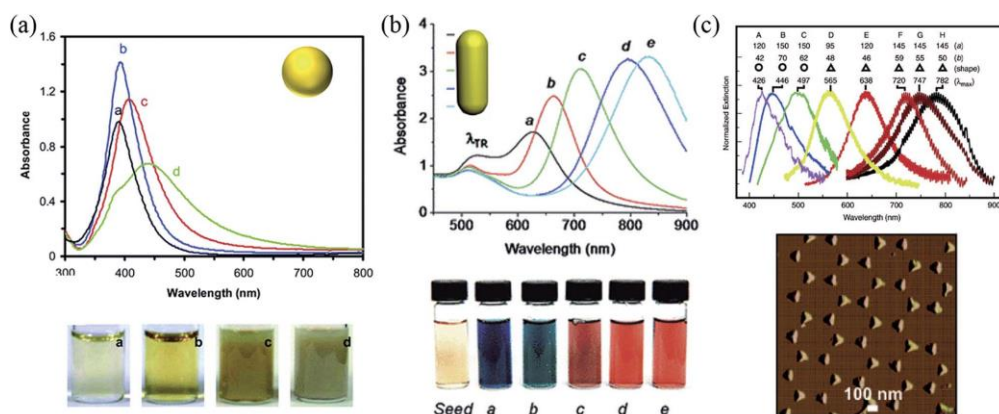
Figure 1-3. (a) Absorption spectra and optical images of Ag NPs with different size. (b) Absorption spectra and optical images of Au nanorods. (c) Size and shape dependency of localized SPR of various Ag NPs and Ag triangle arrays. (down) the representative AFM image of silver triangle arrays. Reproduced from ref. 2

Unlike semiconductor materials made of covalent bonds, the metal nanostructures cause the electrons to collectively fluctuate by the incident electromagnetic field. This oscillation of free electron density generates a dipole moment and amplifies the surrounding electromagnetic field. The free electrons are affected by a columbic force opposite to that of the changing incident electromagnetic field. The result of the free electrons will have oscillatory motion. Thus, the free electrons have a distinct plasma frequency. The degree of incident electromagnetic field will be constant in the NPs if they are smaller than the incident wavelength, inducing a uniform oscillation motion of the dipole moment. Due to SPR of noble metal nanostructures, the local electromagnetic field is amplified, and this phenomenon is called plasmonic properties. Since the metal has a negative dielectric by free electrons, it reflects the incident electromagnetic field and can concentrate locally. Quality factor for plasmonics can be obtained through the metal dielectric, and the most common plasmonic metals are gold and silver. The surrounded environment-induced change in noble metal NPs can be detected using a UV-vis absorption spectrometer.

Since the SPR is very dependent on the size and shape of metal nanoparticles, the phenomenon that occurs in these isotropic particles and the SPR phenomenon resulting from anisotropic morphologies such as triangle, cube shape, and nanorod are very different. In addition, the main reason that SPR phenomenon is attracting attention is that they cause plasmonics. Plasmonic properties have the effect of overcoming the diffraction limit of light by focusing and amplifying light through interaction between light and free metals. The plasmonic field first proceeds by synthesizing original and functional metal nanostructures and studying the optical properties. The research direction for synthesizing

complex, high-dimensional nanoparticles that have hollow or sharp, tip structure.

1.3. Near-field enhancement on hotspot
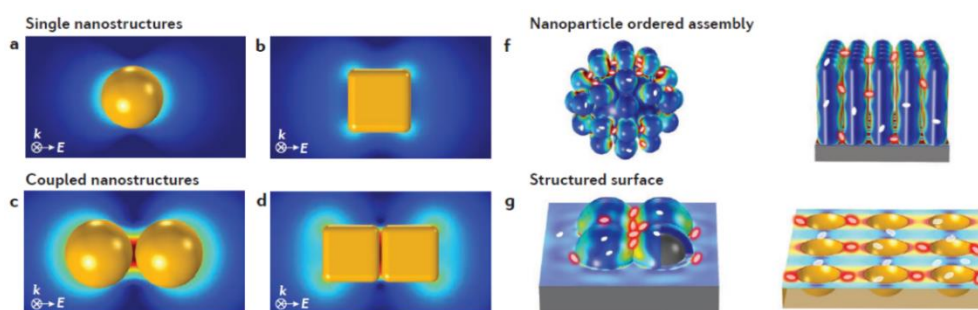
Figure 1-4. Generation of plasmonic hotspot. (a-d) single and coupled nanostructures. (f,g) nanostructured assembly and controlled noble metal surface. Reproduced from ref. 8

Controlling surface morphologies of nanostuructures is a key issue in enhancing their structural and optical properties.[19-21] There are two major approach to maximize the SPR. When the NPs are spaced between the NPs and maintained in the form of nanosized gap, there structures can confine and amplify the electromagnetic field like complete mirrors. In addition, the surface of the structure has a rough or curved curvature shape, that is, the shape of nanotips can also localize the electromagnetic field. As such, the study of concentrating and using light locally through a nanotip or nanogap structure can be defined

as plasmonics. Roughnesses, spikes, and tips in nanoscale are interesting structures owing to the anisotropic enhancement of the electromagnetic field, an effect similar to the lightning rod effect. Their local plasmonic features allow the modulation of localized surface plasmon resonance (LSPR) modes by tuning their lengths, densities, and aspect ratios. The reason for synthesizing the particles with nanotips is to concentrate the electromagnetic field around the nanotips to create an plasmonic effect and use them to improve optical, catalytic, and electrical properties. When the electromagnetic wave moves, the photons have a near-field enhancement phenomenon locally due to the lightning rod effect that collects in the nanotip structure. Precious metal nanoparticles have a negative dielectric constant by free electrons, which reflect and confine the electromagnetic field like an ideal mirror rather than passing through the electric field.

In addition noble metal nanostructures with nanogaps have been of special interest due to their extremely electromagnetic fields and controllable optical properties that can be useful for plasmonic application.[22-24] More specifically, the coupled metallic morphologies with small nanogaps can generate strong and tunable near-field enhancement that can generate significant SERS signals.

1.4. References

1   N. J. Halas, S. Lal, W.-S. Chang, S. Link and P. Nordlander, Chem. Rev., 2011, 111, 3913-3961.

2   J. Olson, S. D.-Medina, A. Hoggard, L.-Y. Wang, W.-S. Chang and S. Link, Chem. Soc. Rev., 2015, 44, 40-57.

3   M. Li, S. K. Cushing and N. Wu, Analyst, 2015, 140, 386-406.

4   S. T. Kochuveedu and D. H. Kim, Nanoscale, 2014, 6, 4966-4984.

5   A. Kinkhabwala, Z. Yu, S. Fan, Y, Avlasevich, K. Mullen and W. E. Moerner, Nat. Photonics, 2009, 3, 654-657

6   H. Palneedi, J. H. Park, D. Maurya, M. Peddigari, G. -T. Hwang, V. Annapureddy, J.-W. Kim, J. -J. Choi, B. -D. Hahn, S. Priya, K. J. Lee and J. Ryu, Adv. Mater., 2018, 30, e1705148

7   G. Jean-Michel and C. Antonino. Nat. Comm. 2017, 8, 16095.

8   S.-Y. Ding, J. Yi, J.-F. Li, R. Panneerselvam, B. Ren, D.-Y. Wu and Z.-Q. Tian. Nat. Rev. Mater., 2016, 1, 1.

9   L. Zhen, Y. Zhongbo, P. Bo, C. Cuong, Z. Chao, Y. Hongjun, X. Qihua, L. Zhiyuan and F. Jixiang. Adv. Mater., 2014, 26, 2431.

10   Makarov, S. V.; Milichko, V. A.; Mukhin, I. S.; Shishkin, I. I.; Zuev, D. A.; Mozharov, A. M.; Krasnok, A. E.; Belov, P. A. Laser Photonics Rev., 2016, 10, 91.

11   A.N. Severyukhina, B.V. Parakhonskiy, E.S. Prikhozhdenko, D.A. Gorin, G.B. Sukhorukov, H. Mohwald, A.M. Yashchenok, ACS Appl. Mater. Inter., 2015, 7, 15466-15473.

12   D. Lin, Z. Wu, S. Li, W. Zhao, C. Ma, J. Wang, Z. Jiang, Z. Zhong, Y. Zheng, X. Yang, ACS Nano, 2017, 11, 1478-1487.

13   W.J. Cho, Y. Kim, J.K. Kim, ACS Nano, 2012, 6, 249-255.

14   Y.J. Oh, K.H. Jeong, Adv. Mater., 2012, 24, 2234-2237.

15   C. R. E. Prodan, N. J. Halas, P. Nordlander, Science, 2003, 302, 419.

16   A. Genç, J. Patarroyo, J. Sancho-Parramon, R. Arenal, M. Duchamp, E. E. Gonzalez, L. Henrard, N. G. Bastús, R. E. Dunin-Borkowski, V. F. Puntes and J. Arbiol, ACS

Photonics, 2016, 3, 770-779.

17   T. H. Park and D. J. Jang, Nanoscale, 2018, 10, 20108-20112.

18   W. Xiong, D. Sikdar, L. W. Yap, P. Guo, M. Premaratne, X. Li and W. Cheng, Nano Research, 2016, 9, 415-423.

19   Y. Xia, Z. Gao, X. Liao, C. Pan, Y. Zhang and X. Feng, CrystEngComm, 2017, 19, 6547-6555.

20   A. J. Blanch, M. Doblinger and J. Rodriguez-Fernandez, Small, 2015, 11, 4550-4559.

21   M. N. Sanz-Ortiz, K. Sentosun, S. Bals and L. M. Liz-Marzan, ACS Nano, 2015, 9, 10489-10497.

22   A. Kuchmizhak, E. Pustovalov, S. Syubaev, O. Vitrik, Y. Kulchin, A. Porfirev, S. Khonina, S. Kudryashov, P. Danilov, A. Ionin, ACS Appl. Mater. Inter., 2016, 8, 24946-24955.

23   M.L. Tseng, Y.-W. Huang, M.-K. Hsiao, H. Huang, H.M. Chen, Y.L. Chen, C.H. Chu, N.-N. Chu, Y.J. He, C.M. Chang, W.C. Lin, D.-W. Huang, H.-P. Chiang, R.-S. Liu, G. Sun, D.P. Tsai, ACS Nano, 2012, 6, 5190-5197.

24   Y. Oh, M. Lee, Appl. Surf. Sci., 2017, 399, 555-564.

Chapter 2. Metal-enhanced fluorescence of gold nanoclusters adsorbed onto Ag@SiO$_2$ core-shell nanoparticle

2.1. Abstract

The static and time-resolved metal-enhanced fluorescence (MEF) of Au_{25}-adsorbed $Ag@SiO_2$ core-shell nanoparticles (NPs) has been studied systematically with variation of shell thicknesses, core sizes, and excitation wavelengths. The emission of Au_{25}-adsorbed $Ag@SiO_2$ NPs is blue-shifted and highly enhanced compared with that of free Au_{25} clusters. The blue shift arises from the plasmonic coupling of Au_{25} clusters with Ag NPs, which decreases exponentially with the increase of separation between Au_{25} clusters and Ag NPs. The photoluminescence (PL) intensity of Au_{25}-adsorbed $Ag@SiO_2$ NPs is higher by a factor of 7.4 times than that of free Au_{25} clusters. The PL enhancement of Au_{25}-adsorbed $Ag@SiO_2$ NPs is determined by two competing processes of near-field enhancement and fluorescence resonance energy transfer (FRET). The increase of the radiative decay rate constant with separation is identical to that of PL enhancement, suggesting that the MEF of Au_{25}-adsorbed $Ag@SiO_2$ NPs arises from the increase of the radiative decay rate constant induced by the near-field enhancement of plasmonic Ag NPs. Au_{25}-adsorbed $Ag@SiO_2$ NPs have also been found as a highly sensitive and selective 'turn-off' sensor for Cu^{2+} ions.

2.2. Introduction

Plasmonic noble-metal nanoparticles (NPs) have ability to localize and enhance an incident electric field when their surface plasmon resonance (SPR) is excited.[1,2] Confined electron oscillations of SPR lead to an intense local electric field, which can be several orders of magnitude stronger than the incident field. SPR is extremely sensitive to change in distance from the surface of metal NPs so that its electric field decays in 10-30 nm.[3] The understanding of spatial interactions between SPR and nearby excited fluorophores helps to build a model for fluorescence-based biological detectors and sensors.[4,5] It is well known that excitation and emission processes can be altered when a fluorophore is near a metal NP.[3-5] Metal-enhanced fluorescence (MEF), occurring between the SPR-induced near-field and an excited fluorophore located in close proximity to the plasmonic metal surface, has been widely studied because it is an efficient way to amplify fluorescence signals.[6-8] There are two mechanisms for MEF related to near-field enhancement.[4,9] One is that a metal NP can concentrate and enhance the local electric field, so fluorophores around the metal NP can effectively absorb more light. This effect is called the nanoantenna effect,[4] which can increase the rate of excitation. The second is that the metal NPs can generate an additional metal-modified radiative decay process, which can increase the total radiative decay rate. As a result, MEF induced by near-field enhancement is determined by the combination of excitation enhancement and emission enhancement. MEF depends strongly on the size and the shape of the metal NP and on separation between the fluorophore and the metal NP.

Especially, the dependence of fluorescence on the distance of the metal NP from the fluorophore is crucial to the MEF effect. At a close distance, fluorescence quenching can be observed due to nonradiative energy transfer from the fluorophore to the metal NP. However, at a certain distance from the plasmonic metal surface, energy transfer into the plasmon resonance is reduced and the electric-field strength can be great enough to enhance fluorescence emission.[4,5] There have been many attempts to measure the distance dependence of fluorescence enhancement and quenching employing diverse fluorophores such as organic dyes, quantum dots, and conjugated polymers.[6-11] However, it is still necessary to predict and measure the change of fluorescence using new types of fluorophores for wide scientific applications. In addition, enhancement factors reported in the literature are highly inconsistent and the mechanism of MEF due to near-field enhancement is still not clear. Therefore, it is necessary to understand the distance-dependent MEF effect with a new type of fluorophores.

As plasmonic metal NPs are smaller than the exciton Bohr radius, they can become fluorescent noble-metal nanoclusters (NCs), which consist of only a few to several tens of atoms with a size smaller than 2 nm. NCs are placed between atoms having discontinuous electronic energy levels and nanoparticles having continuous SPR bands, so they show molecule-like characteristics in fluorescence resulting from discrete and size-tunable electronic transitions.[12,13] Thus, fluorescent metal NCs have been developed as a new class of fluorophores. Compared with conventional quantum dots, noble-metal NCs do not contain toxic heavy metals. In addition, unlike organic dyes, they are photostable and can be readily incorporated with various biological molecules, extending their applications

further in the biotechnology.[13] Especially, protein-protected-Au$_{25}$ NCs have attracted particular interest due to their facile synthesis, low cost, stability, and easy bio-conjugation.[14-17] Because metal NCs are chosen as promising luminescent materials, it is highly valuable to enhance their optical properties for practical applications. As noble-metal NCs possess a low quantum yield, they are not used currently for practical sensing and detecting applications. A lot of efforts have been made to enhance optical properties of the emitters.[18-20] However, up to now, there have been few studies on the photoluminescence (PL) enhancement of noble-metal NCs by the presence of plasmonic NPs. While Muhammed et al. have briefly reported the MEF of Au NCs in the presence of Ag NPs,[21] Qin et al. have studied fluorescence resonance energy transfer (FRET) between Au NCs and Au nanorods.[22]
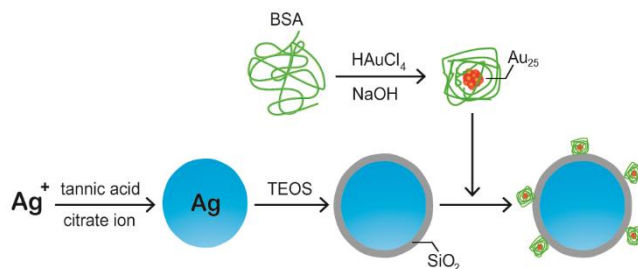
Figure 2-1. Schematic for the preparation process of a Au$_{25}$-adsorbed Ag@SiO$_2$ core-shell nanoparticle, where BSA and TEOS stand for bovine serum albumin and tetraethyl orthosilicate, respectively.

In this paper, we are reporting that the MEF of Au_{25}-adsorbed $Ag@SiO_2$ core-shell NPs, prepared via the schematically shown procedure of Figure 2-1, depends on the thickness of SiO_2 shells as well as the size of Ag cores and the wavelength of excitation. In order to gain a deeper understanding of the MEF mechanism, we have compared the PL intensity and decay time of adsorbed Au_{25} on $Ag@SiO_2$ NPs with the respective ones of free Au_{25} clusters. The PL quantum yield of Au_{25}-adsorbed $Ag@SiO_2$ nanoparticles with a shell thickness of 6 nm are higher by a factor of 9.3 times than that of free Au_{25} clusters, arising from the increase of the radiative decay rate constant by a factor of 17. In addition, we have found that Au_{25}-adsorbed $Ag@SiO_2$ NPs can be exploited as a "turn-off" sensor for the sensitive and selective detection of Cu^{2+} ions.

2.3. Experimental section

2.3.1. Chemicals

Silver nitrate (s, 99.9%), $HAuCl_4 \cdot 3H_2O$ (s, 99%), trisodium citrate dihydrate (s, 99%), tannic acid (s, ACS reagent), tetraethyl orthosilicate (TEOS, l, >98%), bovine serum albumin (BSA, s, 98%), $CuCl_2 \cdot 2H_2O$ (s, ACS reagent), $CoCl_2 \cdot 6H_2O$ (s, ACS reagent), $Fe(NO_3)_3 \cdot 9H_2O$ (s, ACS reagent), $ZnCl_2$ (s, >98%), %), $HgCl_2$ (s, ACS reagent), $Cr(NO_3)_3 \cdot 9H_2O$ (s, 99%) and $PbCl_2$ (s, 98%) were purchased from Sigma-Aldrich. Sodium hydroxide (s, 99%), 25% ammonia(aq), and $NiCl_2 \cdot 6H_2O$ (s, 99.9%) were obtained from

MERCK, and absolute ethanol(l) was purchased from Daejung Chemicals. Deionized water (>15 MΩ cm) from an Elga PURELAB option-S system was used throughout the experiments.

2.3.2. Synthesis of Ag NPs

Ag NPs were prepared according to the reported procedure with slight modification.[23] To prepare 50 nm Ag NPs, 8.4 mg of silver nitrate was dissolved in 100 mL water. Another solution is prepared by dissolving 20.0 mg of tannic acid and 19.8 mg of trisodium citrate dihydrate in 25 mL water. Both solutions were heated to 60 °C before being combined together under vigorous stirring. The mixed solution was boiled for 30 min, then left to cool until room temperature was reached. The resulting solution was centrifuged with a 68 mM aqueous citrate solution (8000 rpm, 10 min) three times and dispersed in 30 mL of water. The concentration of the resulting Ag colloid was calculated to be 0.28 nM (1.7×10^8 NPs/μL).

2.3.3. Synthesis of Ag@SiO$_2$ core-shell NPs

The coating of SiO$_2$ shells on Ag NPs was realized by the Stober method.[10] 1.0 mL of the as-prepared Ag colloidal solution was added into 8.0 mL of ethanol under vigorous stirring. And then a specified 5.0-25 μL amount of a 20% (v/v) TEOS ethanol solution was added in the ethanol-added Ag colloidal solution. After 20 min of stirring, 0.30 mL of 25% ammonia(aq) was added dropwise to the reaction mixture. After being stirred for overnight at room temperature, the solution was centrifuged with ethanol (9000 rpm, 10 min) five

times and dispersed in 10 mL of water. Note that Ag NPs coated with a SiO_2 shell having a thickness of L nm will be designated hereafter as $Ag@SiO_2(L)$ NPs.

2.3.4. Synthesis of Au$_{25}$ clusters

Au$_{25}$ clusters were prepared according to the procedure published elsewhere.[14] 5.0 mL of an aqueous 10 mM $HAuCl_4$(aq) at 37 °C was added to 5.0 mL of an aqueous 50 mg/mL BSA solution at 37 °C under vigorous stirring. 5.0 min later, 0.50 mL of 1.0 M NaOH(aq) was added dropwise to the mixture, and the reaction was allowed to proceed under vigorous stirring at 37 ℃ for overnight. The color of the solution became deep brown.

2.3.5. Preparation of samples for optical characterization

For static and time-resolved emission measurements, each colloidal solution of Ag NPs and $Ag@SiO_2$ NPs was diluted so that the maximum optical density of the SPR band became 0.3. Then, 5.0 mL of the colloidal solution was added with 5.0 μL of the as-prepared Au$_{25}$ solution and stirred gently for 3 h. 5.0 μL of the as-prepared Au$_{25}$ solution was also added to 5.0 mL of water as a reference. For the evaluation of the sensing selectivity of heavy-metal ions such that Cu^{2+}, Ni^{2+}, Co^{2+}, Fe^{3+}, Zn^{2+}, Ag^+, Au^{3+}, Hg^{2+}, Cr^{3+} and Pb^{2+}, 0.10 mL of an aqueous 0.70 mM solution of each cationic species was added to 3.4 mL of the diluted colloidal solution of Au$_{25}$-adsorbed $Ag@SiO_2$ NPs. Note that the final concentrations of Ag or $Ag@SiO_2$ NPs, Au$_{25}$ clusters, and an ionic heavy metal were 1.1 pM, 0.18 μM, and 20 μM, respectively.

2.3.6. Characterization

For transmission electron microscopy (TEM) measurements, 7.0 µL of a colloid was dropped on a carbon-coated copper grid, air-dried, and then examined with a Hitachi H-7600 microscope. While energy-filtering TEM (EFTEM) images were recorded using a Carl Zeiss LIBRA 120 microscope, high-resolution TEM (HRTEM) images were measured using a JEOL JEM-2100F microscope. Matrix-assisted laser desorption ionization time-of-flight (MALDI-TOF) mass spectra were measured using a Bruker Daltonics Bruker Autoflex III mass spectrometer; all the spectra were collected in the positive mode using α-cyano-4-hydroxycinnamic acid as the matrix. While UV/vis absorption spectra were measured with a Scinco S3100 UV/vis. spectrophotometer, emission spectra were obtained using a homebuilt fluorometer consisting of a 75 W Acton Research XS 432 Xe lamp with an Acton Research Spectrapro150 monochromator of 0.15 m and an Acton Research PD438 photomultiplier tube attached to an Acton Research Spectrapro300 monochromator of 0.30 m. Picosecond time-resolved photoluminescence kinetic profiles with excitation of third harmonic pulses (355 nm) from a mode-locked Quantel YG901-10 Nd:YAG laser of 25 ps were detected using a Hamamatsu C2830 streak camera of 10 ps attached to a Princeton Instruments RTE128H CCD detector. Emission wavelengths were selected by cut-off filters (550+ nm). Emission kinetic constants were extracted by fitting measured kinetic profiles to computer-simulated kinetic curves convoluted with instrument temporal response functions.

2.4. Results and discussion
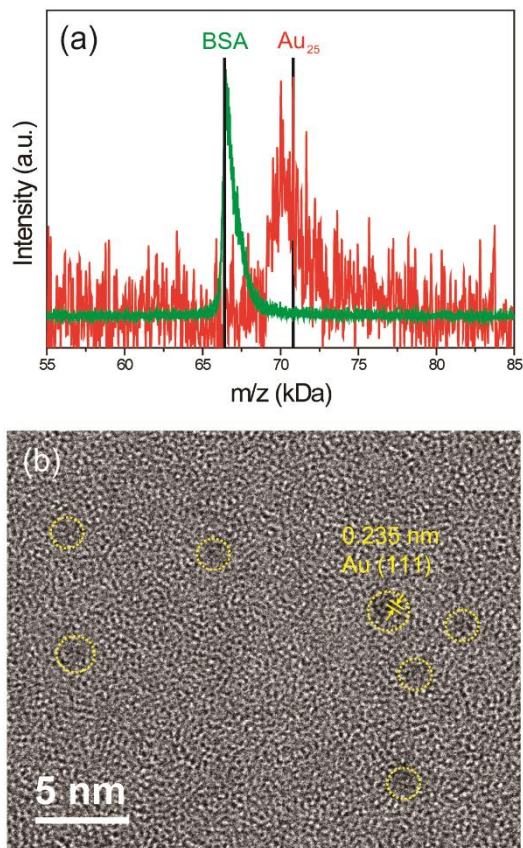
Figure 2-2. (a) MALDI-TOF MS of BSA (green) and BSA-capped Au NCs (red). (b) HRTEM image of BSA-capped Au_{25} NCs.

We have synthesized BSA-stabilized Au_{25} clusters in basic aqueous conditions.[14] Mass spectrometric analysis was carried out with a MALDI-TOF mass spectrometer to understand the number of gold atoms in a Au cluster. While the pure BSA protein showed

the peak at 66.3 kDa, as-prepared Au clusters showed the peak at 71.2 kDa (Figure 2-2),

supporting that a typical Au cluster consists of 25 gold atoms. Our result agrees with the

previous reports that Au NC with 25 Au atoms is thermodynamically most stable and

corresponds to the most common magic cluster size.[14,21] Meanwhile, the HRTEM image

of Figure 2-2b displays that the average diameter of Au_{25} clusters is 1.7 nm and the average

d-spacing value of 0.235 nm agrees well with the standard spacing of 0.2355 nm between

the (111) planes of the fcc gold crystal (JCPDS-04-0784). Overall, Figure 2-2 indicates

that BSA-protected Au_{25} clusters have been prepared well.
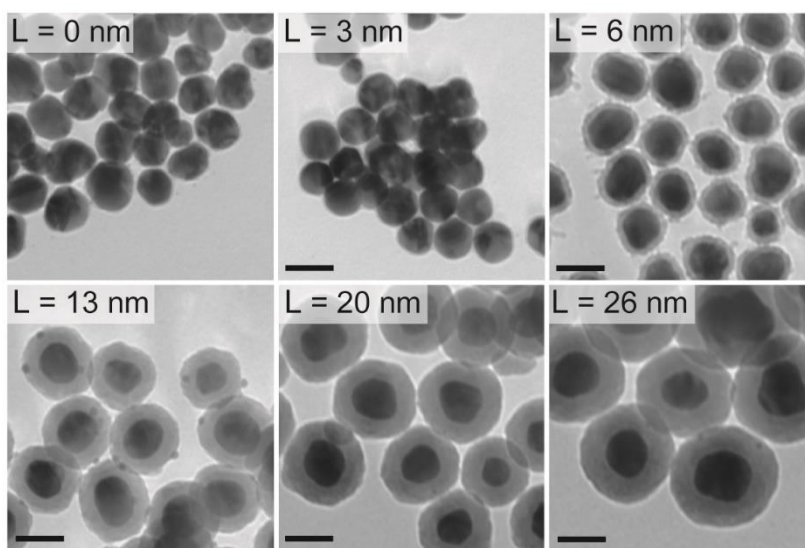
Figure 2-3. TEM images of Ag@SiO$_2$(L) NPs, whose L values are indicated inside. Each scale bar indicates 50 nm.

Ag NPs have been prepared via the co-reduction method.[23] If not specified otherwise, the average diameter of as-prepared Ag NPs is 50±6 nm, which is suitable to induce the MEF effect.[24] Ag@SiO$_2$ core-shell NPs with various shell thicknesses (L) were obtained through the Stober method by changing the amount of added TEOS (Figure 2-3). The core−shell structure has been reported as an effective mean to provide spatial separation between a noble metal and a fluorophore for the metal enhancement of fluorescence and the high stability of metal NPs.[7,10] In particular, silica shells are eco-friendly and optically transparent.
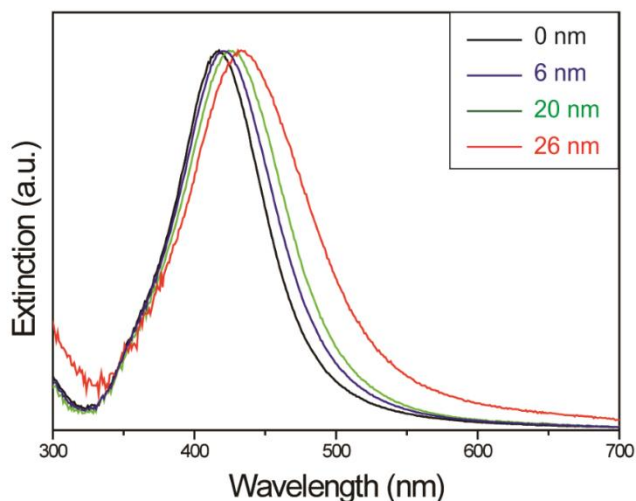
Figure 2-4. Extinction spectra Ag@SiO$_2$(L) NPs, whose L values are indicated inside.

Figure 2-4 shows that the SPR of Ag NPs is shifted gradually to the red as the thickness of SiO$_2$ increases. The red shift with silica coating has been attributed to the increase of

the refractive index of the surrounding medium;[25] the refractive indices of water and silica are 1.33 and 1.45, respectively.
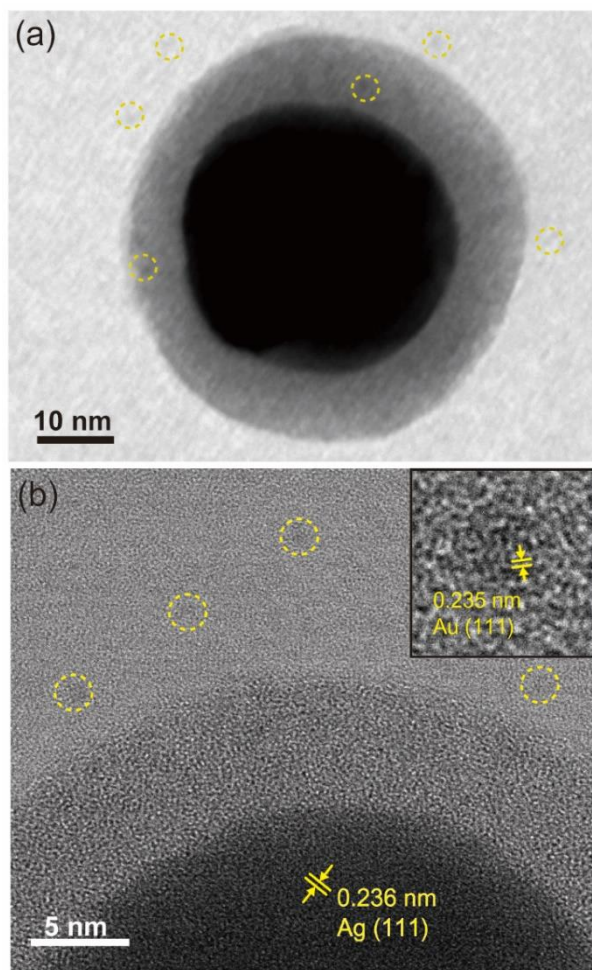
Figure 2-5. (a) EFTEM and (b) HRTEM images of Au_{25}-adsorbed $Ag@SiO_2(6)$ NPs. While dotted circles designate Au_{25} clusters, the inset shows the enlarged HRTEM image of a Au_{25} cluster. Note that the NP of Figure 2-5a is different from the NP of Figure 2-5b.

The EFTEM and HRTEM images of Figure 2-5 reveal the structure of Au_{25}-adsorbed $Ag@SiO_2(6)$ NP. While the EFTEM image of Figure 2-5a indicates that Au NCs with an average diameter of 1.5 nm are adsorbed on the surface of a $Ag@SiO_2$ NP with a core diameter of 43 nm and a shell thickness of 7.4 nm, the HRTEM image of Figure 2-5b shows that Au NCs with a typical diameter of 1.7 nm are adsorbed on a $Ag@SiO_2$ NP with a shell thickness of 5.9 nm. Note that only a small fraction of Au NCs can be seen due to the phase-contrast problem of EFTEM and HRTEM images. In particular, the images of Au NCs are too weak to be observed on the image of a Ag core. The d-spacing value of 0.236 nm observed in the core HRTEM image of Figure 2-5b agrees very well with the standard spacing of 0.2359 nm between the (111) planes of the fcc silver crystal (JCPDS-04-0783). In addition, the d-spacing value of 0.235 nm shown in the inset image of Figure 2-5b matches well with the standard spacing of 0.2355 nm between the (111) planes of the cubic gold crystal (JCPDS-04-0784). In the meantime, lattice fringes have not been observed at all in the shell HRTEM image of Figure 2-5b, suggesting that the silica shell has an amorphous structure. Overall, Figure 2-5 indicates a Au_{25}-adsorbed $Ag@SiO_2(6)$ NP consists of fcc Au NCs with an average diameter of 1.6 nm, an amorphous silica shell, and an fcc silver core. We suggest that for a Au_{25}-adsorbed $Ag@SiO_2$ NP, 2 x 10^5 BSA-capped Au NCs bind to the surface of a silica shell by electrostatic attraction between the positive amine groups of BSA and the negative charges of the silica shell surface.[26,27] A silica shell can offer specific sites to bind protein molecules via electrostatic interactions and hydrogen bonding. Yu et al. have reported that $Fe_3O_4@SiO_2$ NPs can uptake a high loading of BSA molecules.[45] NPs covered with silanol groups assist the immobilization of

BSA primarily through electrostatic interactions. The adsorption of BSA to NPs is also attributed to hydrogen-bonding interactions between C=O and N-H functional groups of BSA and surface hydroxyl groups of $Fe_3O_4@SiO_2$ NPs. In case of bare Ag NPs, Bardhan et al. have reported that BSA binds to NPs by electrostatic and salt-bridge interactions between the amino acid groups of the protein and the negative charges of the metal surfaces.[26,46]
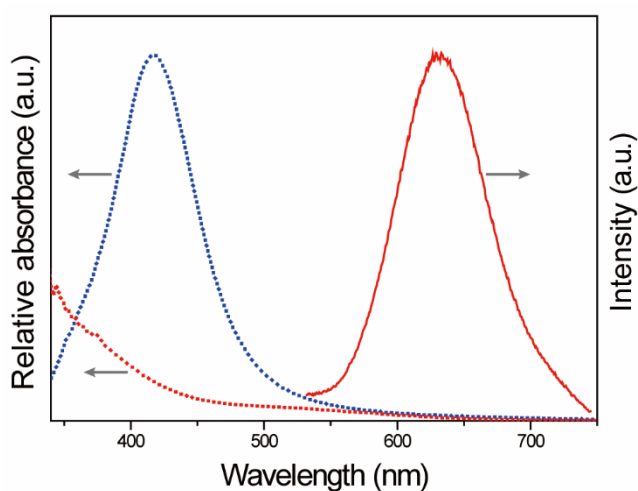
Figure 2-6. Extinction (dotted) and emission spectra (solid) of 50 nm silver NPs (blue) and BSA-capped Au_{25} clusters (red) suspended in water. The sample was excited at 355 nm for the emission spectrum.

On one hand, the UV/vis. extinction spectrum of a 50±6 nm Ag colloidal solution in Figure 2-6 indicates that the maximum of its SPR band is located at 433 nm. The extinction of light by a metal colloid is composed of absorption, leading to fluorescence quenching, and scattering, leading to fluorescence enhancement.[3] Among noble-metal NPs, Ag NPs

have been recognized as an attractive fluorescence enhancer because of their narrow plasmon band and high scattering efficiency.[10] On the other hand, BSA-capped Au_{25} clusters show a featureless absorption band, whose slope changes at 450 nm, and an emission band with the peak at 640 nm. The emission of Au_{25} clusters may be attributed to interband transitions between the $6(sp)^1$ conduction band and the filled $5d^{10}$ band.[28] The calculated quantum yield (QY) of the BSA-capped Au_{25} clusters has been measured as 5.2% by taking rhodamine B as a reference (QY = 65% at 355 nm excitation in ethanol), which is similar to the QY of the previous report.[14] Whereas the SPR band of Ag NPs overlaps significantly with the absorption band of Au_{25} clusters, it does not overlap sufficiently with the emission band of Au_{25} clusters. Therefore, excitation enhancement can be expected to occur due to the near-field enhancement induced by the SPR of Ag NPs while energy transfer from excited Au_{25} clusters to the SPR band of Ag NPs would hardly take place.
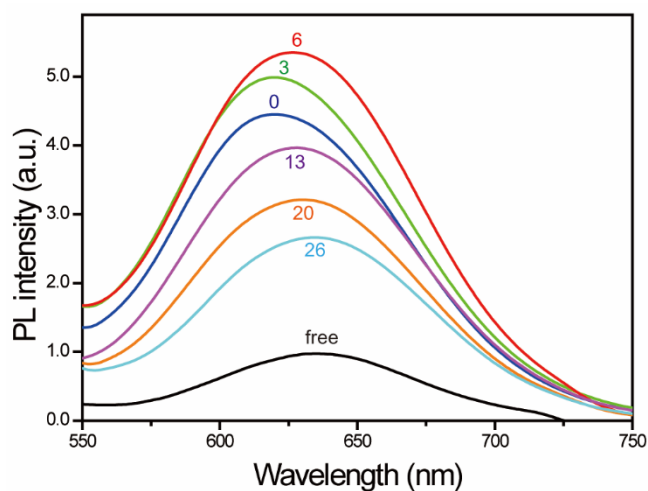
Figure 2-7. PL spectra of Au_{25}-absorbed $Ag@SiO_2$ NPs suspended in water with excitation at 355 nm. The shell thickness of silica in the unit of nm is indicated near each spectrum, while 'free' stands for free Au_{25} clusters without $Ag@SiO_2$ NPs.

Figure 2-7 shows that the emission of Au_{25}-adsorbed $Ag@SiO_2$ NPs is highly enhanced and blue-shifted with respect to that of free Au_{25} clusters. First of all, the PL intensity of Au_{25}-adsorbed $Ag@SiO_2(0)$ NPs is higher 5.5 times in intensity than that of free Au_{25} clusters. It has been widely reported that PL quenching instead of PL enhancement takes place in close proximity (<3 nm) to the metal NP surface due to energy transfer from excited fluorophores to metal NPs.[10,29] In fact, an intrinsic distance of 3.32 nm exists between the $Ag@SiO_2(0)$ NPs and Au_{25} clusters because the hydrodynamic diameter of BSA is reported to be 6.64 nm.[18] Thus, PL enhancement rather than PL quenching has been observed for Au_{25}-adsorbed $Ag@SiO_2(0)$ NPs. For a close examination of PL enhancement as a function of separation between Au_{25} clusters and Ag NPs, from now on, optical

28

properties such as wavelength shifts and enhancement factors (EFs) will be expressed as the variation of separation, which is (L + 3.32) nm.

Table 2-1. Emission decay constants of free Au_{25} clusters and Au_{25}-adsorbed Ag@SiO$_2$ NPs with various silica shell thicknesses.

Sample [a]	EF	λ_{max}/nm	Decay time/ps	QY/%	k_r /ns^{-1}	k_{nr} /ns^{-1}	k_{rm} /ns^{-1}	$(k_r+k_{rm})/k_r$
Au_{25}	1.00	640	799	5.2	0.065	1.19	0.00	1.0
Au_{25}-Ag@SiO$_2$(0)	5.54	622	476	43.5	0.065	1.19	0.846	14
Au_{25}-Ag@SiO$_2$(3)	6.46	623	450	46.5	0.065	1.19	0.967	16
Au_{25}-Ag@SiO$_2$(6)	6.76	628	432	48.6	0.065	1.19	1.060	17
Au_{25}-Ag@SiO$_2$(13)	4.48	630	517	38.4	0.065	1.19	0.679	12
Au_{25}-Ag@SiO$_2$(20)	3.78	633	559	33.2	0.065	1.19	0.534	9.2
Au_{25}-Ag@SiO$_2$(26)	3.05	637	597	28.8	0.065	1.19	0.420	7.5

[a] Suspended in water, excited at 355 nm, and monitored at 550+ nm.

Figure 2-8. (a) $\Delta\lambda$ (= λ_{free} - λ_{NP}) as a function of separation between Au_{25} clusters and Ag NPs, where λ_{free} and λ_{NP} are the wavelengths at the PL maxima of Au_{25} clusters without and with $Ag@SiO_2$ NPs, respectively. The solid line is the best-fitted curve of $\Delta\lambda_0 \cdot exp(-d/\delta)$; $\Delta\lambda_0$ and δ have been estimated as 21.5 and 18.5 nm, respectively, and $\Delta\lambda_0$ has been used to yield ΔE_0 of 67 meV. (b) PL enhancement factors (squares) of Au_{25}-absorbed $Ag@SiO_2$ NPs as a function of separation between Au_{25} clusters and Ag NPs. The solid and dashed lines are the curves best-fitted to $(\alpha + \beta d)^6$ and $(\alpha + \beta/d^3)$, respectively; the fitting details are provided in Table 2-2

Table 2-2. The fitting details of the PL enhancement factor of Au_{25}-adsorbed $Ag@SiO_2$ NPs as a function of separation between Au_{25} clusters and Ag NPs.

Separation region	Fitting equation	α	β
$d < d_c$ [a]	$EF_1 = (\alpha + \beta d)^6$	1.3	7.5×10^{-3} nm^{-1}
$d > d_c$	$EF_2 = \alpha + \beta/d^3$	3.0	6.7×10^3 nm^3

[a] Maximum enhancement distance (d_c, 11.5 nm) when $EF_1 = EF_2$ = maximum enhancement factor (EF_{max}, 7.4).

Figure 2-7 and Table 2-1 have indicated that the wavelength at the PL maximum (λ_{max}) of Au_{25}-adsorbed $Ag@SiO_2$(L) NPs (λ_{NP}) is shifted to the blue from the λ_{max} of free Au_{25} clusters (λ_{free}) and that the shift decreases as L increases. We consider that the wavelength shifts of PL spectra arise from the plasmonic coupling of Au_{25} clusters with Ag NPs.[30] To examine the wavelength shifts closely, we have plotted $\Delta\lambda$ as a function of separation in Figure 2-8a; $\Delta\lambda$ decreases exponentially with the increase of separation. Figure 2-8a displays that the values of $\Delta\lambda$ have been fitted to $\Delta\lambda_0 \cdot \exp(-d/\delta)$ with $\Delta\lambda_0$ of 21.5 nm and δ of 18.5 nm. The result suggests that the coupling strength (ΔE_0) and the coupling distance (δ) of hybridization between Au_{25} clusters and Ag NPs are 67 meV and 18.5 nm, respectively, as the spectral shifts of Au_{25}-adsorbed $Ag@SiO_2$ NPs can be explained by the plasmon hybridization. The plasmon hybridization theory has been developed to understand how the SPRs of elementary geometries interact with each other to generate the hybridized plasmon modes of a nanocomposite.[31-33] This interaction results in the splitting of the plasmon resonances into two new resonance bands: the lower-energy

31

bonding plasmon band and the higher-energy antibonding plasmon band. Thus, the emission property of Au_{25}-adsorbed $Ag@SiO_2$ NPs has been modified due to the plasmon coupling, which leads to the increase of the emission energy and decreases exponentially with the increase of separation. Nevertheless, Figure 2-8a indicates directly that the SPR of Ag NPs interacts with Au_{25} clusters to increase the PL intensity of Au_{25} clusters enormously as shown in Table 1 and Figure 2-8b (see below).

Figure 2-7 and Table 2-1 indicate that the PL intensity of Au_{25}-adsorbed $Ag@SiO_2(L)$ NPs increases in the beginning and then decreases as L increases. In order to have an insight into the distance-dependent MEF of Au_{25}-adsorbed $Ag@SiO_2$ NPs, the enhancement factor (EF) of PL, which is the PL ratio of adsorbed Au_{25} clusters on $Ag@SiO_2$ NPs to free Au_{25} clusters, has been plotted as a function of separation in Figure 2-8b. On one hand, EF values before the maximum enhancement distance (d_c) have been fitted to a d^6 dependency, which is in agreement with the fluorescence resonance energy transfer (FRET).[3,34,35] On the other hand, EF values after d_c have been fitted to a d^{-3} dependency, which is in agreement with the MEF effect.[34,35] The obtained constants of the fitting equations in Table S1 are found to be similar to the respective values of the previous report.[35] The maximum enhancement factor (EF_{max}) and d_c were estimated as 7.4 and 11.5 nm, respectively. This suggests that as supported by the plasmonic coupling of Figure 2-8b, MEF increases due to the increase of the near-field enhancement as a silver nanosphere approaches to a Au_{25} cluster. However, within a distance shorter than 11.5 nm, MEF decreases with the decrease of separation because the d^{-3}-dependent increase of MEF is overwhelmed by the d^6-dependent decrease of FRET. It is interesting to note that our

estimated optimal MEF distance of 11.5 nm is consistent with the fact that the maximum

PL enhancement generally occurs in a range of 10-12 nm from a plasmonic surface.[6,7,29]

Overall, Figures 2-7 and 2-8 have revealed that the MEF effect of Au_{25}-adsorbed $Ag@SiO_2$

NPs is determined by two competing processes of FRET and the near-field enhancement

via the plasmonic coupling.
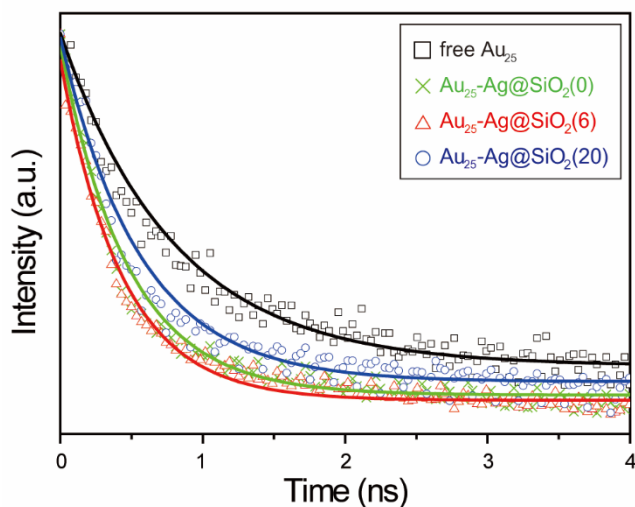
Figure 2-9. Emission decay profiles of indicated free Au_{25} clusters and Au_{25}-adsorbed $Ag@SiO_2$
NPs suspended in water, monitored at 550+ nm after excitation at 355 nm. Solid lines are best-fitted
curves to extract kinetic constants.

In order to gain a deeper understanding of the MEF effect, we have compared the PL

decay kinetics of Au_{25} clusters adsorbed on $Ag@SiO_2$ NPs with that of free Au_{25} clusters.

Figure 2-9 and Table 2-1 indicate that each picosecond emission kinetic profile of free Au_{25}

clusters and Au_{25}-adsorbed $Ag@SiO_2$ NPs can be fitted into a single exponential decay;

33

the lifetime is attributed to singlet transitions between excited sp bands and low-lying d bands of Au_{25} clusters.[18,28,36] The decay time of Au_{25}-adsorbed $Ag@SiO_2$ NPs is not only significantly shorter than that of free Au_{25} clusters but also dependent on the value of L; while the lifetime of free Au_{25} clusters is 799 ps, the lifetimes of Au_{25}-adsorbed $Ag@SiO_2$ NPs with L values of 0, 6, and 20 are 476, 432, and 559 ps, respectively. In other words, although the lifetime of Au_{25}-adsorbed $Ag@SiO_2$ NPs is always shorter than that of free Au_{25} clusters, it decreases in the beginning and then increases as the shell thickness increases. It is noteworthy from Figure 2-7 that the PL intensity of Au_{25}-adsorbed $Ag@SiO_2$ NPs increases in the beginning and then decreases as the shell thickness increases, although it is always stronger than the PL intensity of free Au_{25} clusters. These results apparently suggest that the increase of the PL intensity is related to the decrease of the PL decay time, as presented in Figure 2-10.
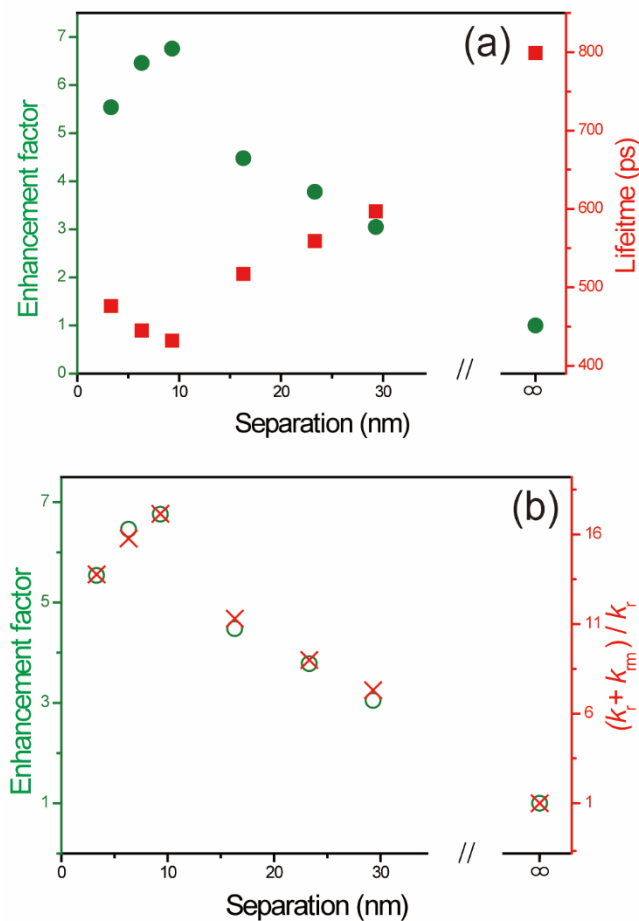
Figure 2-10. (a) PL enhancement factors (circles) and lifetimes (squares) of Au_{25}-absorbed $Ag@SiO_2$ NPs as a function of separation. Note that the values at ∞ were obtained from free Au_{25} clusters. (b) PL enhancement factors (circles) and $(k_r + k_{rm})/k_r$ values (crosses) of Au_{25}-absorbed $Ag@SiO_2$ NPs as a function of the separation.

Figure 2-10 indicates that the behavior of EF with separation is almost opposite to that of the lifetime, suggesting that the MEF of Au_{25}-adsorbed $Ag@SiO_2$ NPs arises from the increase of the decay rate constant of Au_{25} clusters due to the presence of Ag NPs (see

below). This is very unusual; for an ordinary fluorophore, the PL intensity decreases as the PL lifetime decreases due to the increase of the nonradiative decay rate constant of the excited fluorophore. Figures. 2-8b and 2-11a suggest that as a plasmonic Ag NP approaches to a Au_{25} cluster, the lifetime decreases to increase the MEF effect due to the increase of the near-field enhancement. However, within a separation shorter than the maximum enhancement distance, the lifetime increases to decrease the MEF with the decrease of separation because the increase of the MEF effect is suppressed by the decrease of the FRET effect. Furthermore, a close examination of PL intensities and lifetimes reveals that the MEF effect of Au_{25}-adsorbed $Ag@SiO_2$ NPs is due to the increase of the radiative decay rate constant of Au_{25} clusters due to the near-field enhancement of Ag NPs, as shown in Figure 2-10b.

The PL decay time (τ_0) and the PL quantum yield (Q_0) of free fluorophores can be given by Eqs. (1) and (2), respectively,[37]

$$\tau_0 = \frac{1}{k_r + k_{nr}} \tag{1}$$

$$Q_0 = \frac{k_r}{k_r + k_{nr}} = \tau_0 \cdot k_r \tag{2}$$

where k_r and k_{nr} are the radiative and the nonradiative decay rate constants, respectively. Because Q_0 and τ_0 of free Au_{25} clusters have already been measured as 5.2% and 799 ps, respectively, k_r and k_{nr} can be calculated as 0.065 and 1.2 ns^{-1}, respectively, using Eqs. (1) and (2). The relaxation dynamics of Au_{25}-adsorbed $Ag@SiO_2$ NPs is complex because plasmonic Ag NPs increase the radiative decay rate of the emitters. For Au_{25} clusters in

close proximity to Ag NPs, the metal-modified decay time (τ_m) and quantum yield (Q_m) and of the Au$_{25}$ clusters can be given by Eqs. (3) and (4), respectively,[26,34]

$$\tau_m = \frac{1}{k_r + k_{rm} + k_{nr}} \tag{3}$$

$$Q_m = \frac{k_r + k_{rm}}{k_r + k_{rm} + k_{nr}} = (k_r + k_{rm}) \cdot \tau_m \tag{4}$$

where k_{rm} is a new radiative decay rate constant added due to the presence of Ag NPs. When Au$_{25}$ clusters are near Ag NPs, the enhanced near-field of the Ag NPs increases the amount of light absorbed by the clusters. In addition, plasmonic coupling occurs between Au$_{25}$ clusters and Ag NPs, causing an increase in the radiative decay rate constant of Au$_{25}$ clusters.[26] In this case, the total emission rate constant increases by addition of k_{rm} to k_r.[38] Assuming that the change of k_{nr} in Au$_{25}$-absorbed Ag@SiO$_2$ NPs is negligible because PL quenching is not detected,[26] we can calculate k_{rm} according to Eq. (3) with the experimentally obtained PL decay time of Au$_{25}$-absorbed Ag@SiO$_2$ NPs. On the basis of this analysis, it is possible to quantitatively estimate the emission enhancement, $(k_r+k_{rm})/k_r$, and the Q_m of the Au$_{25}$-adsorbed Ag@SiO$_2$ NPs,[38] as shown in Table 1. The results indicate that as the shell thickness becomes near optimal, $(k_r+k_{rm})/k_r$ becomes as large as 17 to enhance QY as highly as 49%, suggesting that Au$_{25}$-adsorbed Ag@SiO$_2$ NPs can be used for biomarkers and sensors as conventionally well-known visible dyes. Figure 2-10b indicates that the behavior of emission enhancement with separation is almost identical to that of EF, suggesting that the MEF of Au$_{25}$-adsorbed Ag@SiO$_2$ NPs arises from the

emission enhancement of Au_{25} clusters due to the presence of Ag NPs. As a plasmonic Ag NP approaches to a Au_{25} cluster, the total emission rate constant increases to enhance the MEF effect due to the near-field enhancement. However, within a separation shorter than the maximum enhancement distance, the emission rate constant decreases to diminish the MEF effect with the decrease of separation. Therefore, we can conclude that the PL enhancement arises from the increase of the radiative decay rate constant induced by the near-field enhancement of plasmonic Ag NPs.
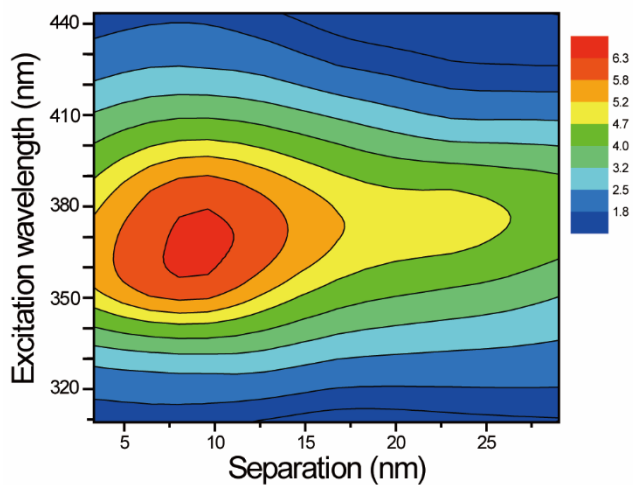
Figure 2-11. Contour plot for the PL enhancement factors of Au_{25}-adsorbed $Ag@SiO_2$ NPs as functions of the separation and the excitation wavelength.

The contour plot of Figure 2-11 shows the dependence of the PL enhancement of Au_{25}-adsorbed Ag@SiO_2 NPs on the excitation wavelength as well as on the separation.[39] The highest PL enhancement can be found from the dark-red 'hot-spot' region with the separation of 7-11 nm and the excitation wavelength of 360-380 nm. In particular, along with the excitation wavelength of 370 nm, the yellow region extends as long as 26 nm in separation. In fact, the coupling distance of hybridization between Au_{25} clusters and Ag NPs has been found to be 24.6 nm with excitation at 370 nm, which is significantly longer than the coupling distance of 18.5 nm with excitation at 355 nm. We consider that our finding would be beneficial for the efficient luminescence applications of BSA-capped Au_{25} clusters.
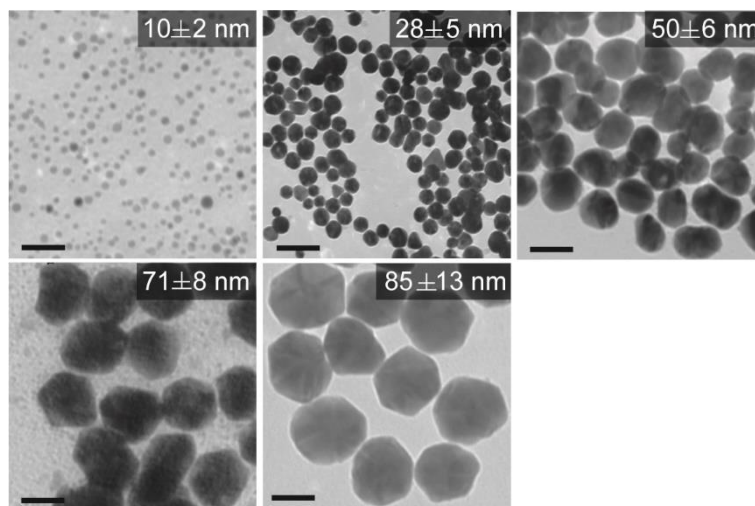
Figure 2-12. TEM images of Ag NPs with diverse average diameters indicated inside. Each scale bar indicates 50 nm.

Table 2-3. Diameters and extinction λ_{max} values of Ag NPs prepared at various concentrations of sodium citrate and tannic acid.

Diameter/nm	λ_{max}/nm	Sodium citrate/mM	Tannic acid/mM
10±2	398	0.81	30.6
28±5	414	0.54	56.4
50±6	433	0.54	94.1
71±8	454	0.27	94.1
85±13	464	0.09	94.1
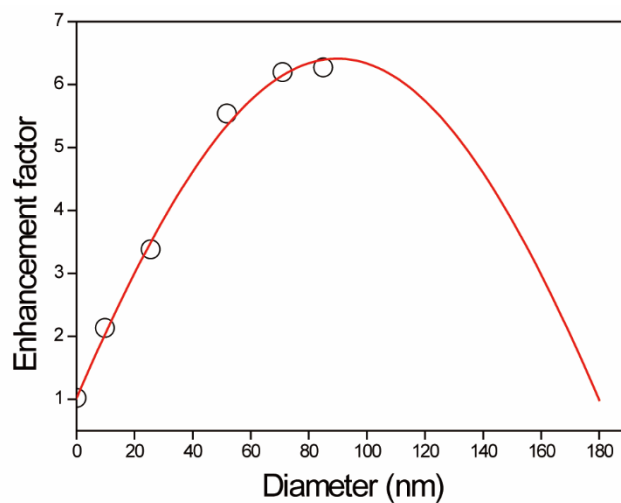
Figure 2-13. PL enhancement factors, with excitation at 355 nm, of Au_{25}-adsorbed Ag@SiO$_2$(0) NPs as a function of the diameter of Ag NPs. The red line represents the best-fitted Gaussian curve, whose maximum is located at 90 nm.

MEF depends strongly on the sizes of metal NPs. Especially, Ag NPs have high scattering efficiencies, and their optical properties are highly dependent upon their diameters. Thus, we have also measured how the PL enhancement of Au_{25}-adsorbed Ag NPs is dependent on the diameters of Ag NPs. The diameters of Ag NPs were controlled in the range of 10-85 nm by altering the respective concentrations of tannic acid and sodium citrate; the diameters of Ag NPs have been found to increase with the concentration increase of tannic acid and the concentration decrease of sodium citrate, as shown in Figure 2-12 and Table 2-3. Figure 2-13 indicates that the PL intensity of Au_{25}-adsorbed Ag NPs increases initially with the sizes of Ag NPs. Although we could not synthesize Ag NPs with diameters of >90 nm via the co-reduction method,[23] we have been able to estimate the dependence of the PL enhancement on diameters longer than 90 nm by fitting our diameter-dependent EF values to a Gaussian curve, whose maximum is located at a diameter of 90 nm. As the average diameter of Ag NPs increases in the beginning, a scattering portion of Ag NPs increases, enhancing the MEF effect. However, the intensity of the electric field near plasmonic metal NPs has been reported to decrease with a further increase of particle sizes,[24] supporting our estimation that the PL enhancement of Au_{25}-adsorbed Ag NPs would reach the maximum at a particle diameter of 90 nm.

Figure 2-14. Sensing selectivity of Au_{25}-adsorbed $Ag@SiO_2(6)$ NPs for Cu^{2+} over other heavy metal ions. The concentrations of the respective metal ions were 20 μM, and samples were excited at 370 nm. The gray bars stand for the PL intensities of free Au_{25} clusters while the red bars stand for the PL intensities of Au_{25}-adsorbed $Ag@SiO_2(6)$ NPs.

Metal-selective colloidal nanosensors have attracted intense attention in environmental issues.[40] The PL of Au_{25} clusters can be used be as a highly sensitive and selective "turn-off" sensor for Cu^{2+} ions.[41,42] The PL quenching occurs due to interactions between a Cu^{2+} ion and the carboxyl group of BSA adsorbed to a Au_{25} cluster because the Cu^{2+} ion has more affinity toward BSA than any other types of ions.[21] When Cu^{2+} ions are added to an aqueous solution of Au_{25} clusters, the ions mediate attractive protein–protein interactions and lead to PL quenching due to the aggregation of BSA-capped Au_{25} clusters; this effect is called aggregation-induced PL quenching.[43] Figure 2-14 shows the PL intensities of free Au_{25} clusters and Au_{25}-adsorbed $Ag@SiO_2(6)$ NPs upon exposure to six heavy metal ions in water, where F_0 and F are PL intensities in the absence and presence of metal ions,

respectively. The concentration of each ionic metal is 20 μM, which is the maximum safety level of Cu^{2+} in drinking water defined by the US Environmental Protection Agency.[42] Sensing selectivity was measured with excitation at 370 nm, the excitation wavelength yielding the maximum MEF effect in Figure 2-11
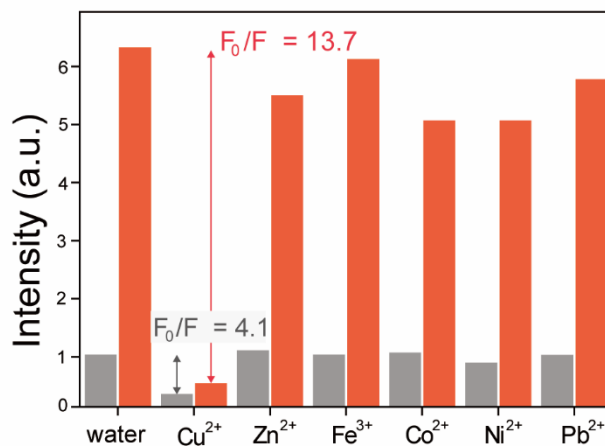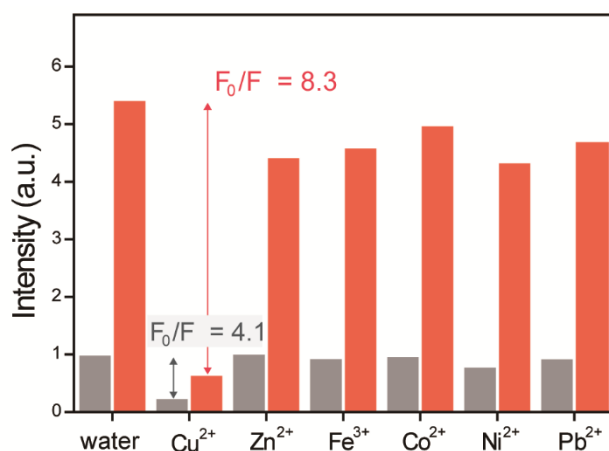

Figure 2-15. Sensing selectivity of Au_{25}-adsorbed $Ag@SiO_2(0)$ NPs for Cu^{2+} over other heavy metal ions. The concentrations of the respective metal ions were 20 μM, and samples were excited at 370 nm. The gray bars stand for the PL intensities of free Au_{25} clusters while the red bars stand for the PL intensities of Au_{25}-adsorbed $Ag@SiO_2(0)$ NPs.

The gray bars in Figures 2-14 and 2-15 stand for the PL intensities of free Au_{25} clusters. The emission was quenched almost completely only in the presence of Cu^{2+} and remained almost invariant in the presence of the other metal ions; the PL intensity was decreased 4.1-fold in the presence of Cu^{2+}. The PL of Au_{25}-adsorbed $Ag@SiO_2$ NPs was drastically

quenched by Cu^{2+} with respect to that of free Au_{25} clusters. As already presented, Au_{25} clusters emit enhanced PL when they interact with $Ag@SiO_2$ NPs. Thus, when Au_{25} clusters having the MEF effect were aggregated by Cu^{2+} ions, their emission was more severely quenched. Figure 2-15 shows that the PL intensity of Au_{25}-adsorbed $Ag@SiO_2(0)$ NPs decreases 8.3-fold in the presence of Cu^{2+}; the turn-off ratio for Au_{25}-adsorbed $Ag@SiO_2(0)$ NPs is two times larger than that of free Au_{25} clusters. In the presence of Hg^{2+} ions, the PL intensity of Au_{25}-adsorbed $Ag@SiO_2(0)$ NPs decreases 5.5-fold. It is reported that the emission of BSA-capped Au clusters can be used be as a sensitive and selective sensor for Hg^{2+} ions based on high-affinity metallophilic Hg^{2+}-Au^+ interactions; Hg^{2+} ions have a very high affinity for thiol-containing biomolecules so that Hg^{2+} ions can coordinate to amino acids of BSA-protected Au_{25} clusters, inducing the aggregation of Au clusters.[43,47] However, the turn-off ratio of Hg^{2+} ions for Au_{25}-adsorbed $Ag@SiO_2(0)$ NPs is just 1.7 times larger than that for free Au_{25} clusters, indicating that the sensing selectivity of Au_{25}-adsorbed $Ag@SiO_2(0)$ NPs is lower for Hg^{2+} ions than for Cu^{2+} ions. Meanwhile, the sensing selectivity for Au^{3+} ions is very unusual. The PL emission of free Au_{25} clusters remained almost invariant in the presence of the Au^{3+} ions. However, the PL emission of Au_{25}-adsorbed $Ag@SiO_2(0)$ NPs was drastically quenched in the presence of Au^{3+} ions. The colloidal color of Au_{25}-adsorbed $Ag@SiO_2(0)$ NPs changed from yellow to blue upon addition of $Au^{3+}(aq)$. Thus, we suggest that the color change of the plasmonic metal colloid resulted from galvanic replacement; silver-gold alloy nanoparticles were generated and aggregated together with adsorbed Au_{25} clusters.[48] Surprisingly, the PL intensity of Au_{25}-adsorbed $Ag@SiO_2(6)$ NPs decreases 13.7-fold by Cu^{2+}; the turn-off ratio for Au_{25}-

adsorbed Ag@SiO$_2$(6) NPs is 3.3 times larger than that of free Au$_{25}$ clusters. It has already been shown that Au$_{25}$-adsorbed Ag@SiO$_2$(6) NPs have the most effective PL enhancement. In addition, electrostatic attraction between Au$_{25}$ clusters and Ag@SiO$_2$ NPs is known to be weaker than attraction between Au$_{25}$ clusters and Ag NPs, suggesting that aggregation-induced PL quenching by Cu^{2+} ions would be more prominent in Au$_{25}$-adsorbed Ag@SiO$_2$(6) NPs than in Au$_{25}$-adsorbed Ag NPs.[8,44] Overall, our results have shown that Au$_{25}$-adsorbed Ag@SiO$_2$(6) NPs with the strongest MEF effect also become the most sensitive and selective 'turn-off' sensor for Cu^{2+} ions.

2.5.   Conclusions

The MEF effect of Au$_{25}$-adsorbed Ag@SiO$_2$ core-shell NPs depends on the thickness of silica shells as well as the wavelength of excitation, and the diameter of Ag NPs. The emission of Au$_{25}$-adsorbed Ag@SiO$_2$ NPs is blue-shifted and highly enhanced compared with that of free Au$_{25}$ clusters. The emission wavelength shift arises from the plasmonic coupling of Au$_{25}$ clusters with Ag NPs, which decreases exponentially with the increase of separation between Au$_{25}$ clusters and Ag NPs. The PL intensity of Au$_{25}$-adsorbed Ag@SiO$_2$ NPs is higher by a factor of 7.4 times than that of free Au$_{25}$ clusters. The PL enhancement of Au$_{25}$-adsorbed Ag@SiO$_2$ NPs is determined by two competing processes of FRET and the near-field enhancement via the plasmonic coupling. A close examination of PL lifetimes has revealed that the MEF effect of Au$_{25}$-adsorbed Ag@SiO$_2$ NPs is due to the

increase of the radiative decay rate constant of Au_{25} clusters resulting from the near-field enhancement of Ag NPs. Au_{25}-adsorbed $Ag@SiO_2$ NPs have also been found as a highly sensitive and selective 'turn-off' sensor for Cu^{2+} ions.

2.6. Acknowledgements

2.7. References

1   N. J. Halas, S. Lal, W.-S. Chang, S. Link and P. Nordlander, Chem. Rev., 2011, 111, 3913-3961.

2   J. Olson, S. D.-Medina, A. Hoggard, L.-Y. Wang, W.-S. Chang and S. Link, Chem. Soc. Rev., 2015, 44, 40-57.

3   M. Li, S. K. Cushing and N. Wu, Analyst, 2015, 140, 386-406.

4   S. T. Kochuveedu and D. H. Kim, Nanoscale, 2014, 6, 4966-4984.

5   W. Deng, F. Xie, H. T. M. C. M. Baltar and E. M. Goldys, Phys. Chem. Chem. Phys., 2013, 15, 15695-15708.

6   L. Wang, X. Wang, S. Mao, H. Wu, X. Guo, Y. Ji and X. Han, Nanoscale, 2016, 8, 4030-4036.

7   C. Liao, L. Tang, X. Gao, R. Xu, H. Zhang, Y. Yu, C. Lu, Y. Cui and J. Zhang,

Nanoscale, 2015, 7, 20607-20613.

8   X. Wang, F. He, X. Zhu, F. Tang and L. Li, Sci. Rep., 2014, 4, 4406.

9   K. Munechika, Y. Chen, A. F. Tillack, A. P. Kulkarni, I. J.-L. Plante. A. M. Munro and D. S. Ginger, Nano Lett., 2010, 10, 2598-2603.

10   Z. Bai, R. Chen, P. Si, Y. Huang, H. Sun and D.-H. Kim, ACS Appl. Mater. Interfaces, 2013, 5, 5856-5860.

11   M. L.-Viger, D. Brouard and D. Boudreau, J. Phys. Chem. C, 2011, 115, 2974-2981.

12   P. Yu, X. Wen, Y.-R. Toh, X. Ma and J. Tang, Part. Part. Syst. Charact., 2015, 32, 142-163.

13   L. Zhang and E. Wang, Nano Today, 2014, 9, 132-157.

14   J. Xie, Y. Zheng and J. Y. Ying, J. Am. Chem. Soc., 2009, 131, 888-889.

15   Y.-S. Chen, H. Choi and P. V. Kamat, J. Am. Chem. Soc., 2013, 135, 8822-8825.

16   Y. Negishi, M. Mizuno, M. Hirayama, M. Omatoi, T. Takayama, A. Iwase and A. Kudo, Nanoscale, 2013, 5, 7188-7192.

17   S. Liu and Y.-J. Xu, Sci. Rep., 2016, 6, 22742.

18   T. Das, P. Ghosh, M. S. Shanavas, A. Maity, S. Mondal and P. Purkayastha, Nanoscale, 2012, 4, 6018-6024.

19   S. Wang, X. Meng, A. Das, T. Li, Y. Song, T. Cao, X. Zhu, M. Zhu and R. Jin, Angew. Chem. Int. Ed., 2014, 53, 2376 –2380.

20   X. Zhang, F.-G. Wu, P. Liu, N. Gu and Z. Chen, Small, 2014, 10, 5170-5177.

21   M. A. H. Muhammed, P. K. Verma, S. K. Pal, A. Retnakumari, M. Koyakutty, S. Nair and T. Pradeep, Chem. Eur. J., 2010, 16, 10103-10112.

22   L. Qin, X. He, L. Chen and Y. Zhang, ACS Appl. Mater. Interfaces, 2015, 7, 5965-5971.

23   L. Rainville, M.-C. Dorais and D. Boudreau, RSC Adv., 2013, 3, 13953-13960.

24   J. Zhang, Y. Fu, M. H. Chowdhury and J. R. Lakowicz, J. Phys. Chem. C, 2008, 112, 18-26.

25   M. Son, J. Lee and D.-J. Jang, J. Mol. Catal. A: Chem., 2014, 385, 38-45.

26   R. Bardhan, N. K. Grady, J. R. Cole, A. Joshi and N. J. Halas, ACS Nano, 2009, 3,

744-752.

27   P. Yu, X. Wen, Y.-R. Toh, Y.-C. Lee and J. Tang, RSC Adv., 2013, 3, 19609-19616.

28   P.-C. Chen, C.-K. Chiang and H.-T. Chang, J. Nanopart. Res., 2013, 15, 1336.

29   S. T. Kochuveedu, T. Son, Y. Lee, M. Lee, D. Kim and D. H. Kim, Sci. Rep., 2014, 4, 4735.

30   H.-Y. Chen, K.-W. Liu, M.-M. Jiang, Z.-Z. Zhang, L. Liu, B.-H. Li, X.-H. Xie, F. Wang, D.-X. Zhao, C.-X. Shan and D.-Z. Shen, J. Phys. Chem. C, 2014, 118, 679-684

31   S. J. Kim and D.-J. Jang, Mater. Lett., 2008, 62, 4500-4502

32   E. Prodan, C. Radloff, N. J. Halas and P. Nordlander, Science, 2003, 302, 419-422

33   D. Melnikau, R. Esteban, D. Savateeva, A. Sanchez-Iglesias, M. Grzelczak, M. K. Schmidt, L. M. Liz-Marzan, J. Aizpurua and Y. P. Rakovich, J. Phys. Chem. Lett., 2016, 7, 354-362.

34   C. D. Geddes and J. R. Lakowicz, J. Fluoresc., 2002, 12, 121-129.

35   Z. Zhou, H. Huang, Y. Chen, F. Liu, C. Z. Huang and N. Li, Biosens. Bioelectron., 2014, 52, 367-373.

36   J. Zheng, J. T. Petty and R. M. Dickson, J. Am. Chem. Soc., 2003, 125, 7780-7781.

37   D. Choi, J-Y. Pyo, Y. Kim and D.-J. Jang, J. Mater. Chem. C, 2015, 3, 3286-3293.

38   J.-H. Song, T. Atay, S. Shi, H. Urabe and A. V. Nurmikko, Nano Lett., 2005, 5, 1557-1561.

39   N. S. Abadeer, M. R. Brennan, W. L. Wilson and C. J. Murphy, ACS Nano, 2014, 8, 8392-8406.

40   P. D. Howes, R. Chandrawati and M. M. Stevens, Science, 2014, 346, 1247390.

41   Z. Lin, F. Luo, T. Dong, L. Zheng, Y. Wang, Y. Chi and G. Chen, Analyst, 2012, 137, 2394-2399.

42   T. Shu, L. Su, J. Wang, X. Lu, F. Liang, C. Li and X. Zhang, Anal. Chem., 2016, 88, 6071-6077.

43   P. Yu, X. Wen, Y.-R. Toh, J. Huang and J. Tang, Part. Part. Syst. Charact., 2013, 30, 467-472.

44   C. Li, Y. Zhu, X. Zhang, X. Yang and C. Li, RSC Adv., 2012, 2, 1765-1768.

45   C. H. Yu, A. A-Saadi, S.-J. Shih, L. Qiu, K. Y. Tam and S. C. Tsang, J. Phys. Chem. C, 2009, 113, 537-543.

46   S. H. Brewer, W. R. Glomm, M. C. Johnson, M. K. Knag and S. Franzen, Langmuir, 2005, 21, 9303-9307.

47   F. Chai, T. Wang, L. Li, H. Liu, L. Zhang, Z. Su and C. Wang, Nanoscale Res Lett, 2010, 5, 1856-1860.

48   T.-H. Park, H. Lee, J. Lee and D.-J. Jang, RSC Adv., 2017, 7, 7718-7724.

Chapter 3. Hollow and inward-bumpy gold nanoshells fabricated using expanded silica mesopores as templates

3.1. Abstract

Plasmonic nanoparticles can produce an enhanced electromagnetic field in their vicinity due to their localized surface plasmon resonance (LSPR). In particular, gold nanoshells (NSs) are of great interest due to their tunable LSPR absorption band ranging from the visible to the infrared region with superior bio-compatibility. We have fabricated hollow and bumpy Au (HBA) NSs with rough surfaces using expanded silica mesopores as templates. Because some Au seeds were located at the inner surfaces of silica mesopores, produced Au NSs have inherent inward-grown nanobumps. During seven successive reduction steps, the LSPR peak of Au nanostructures shifted progressively toward a longer wavelength as the sizes of Au seeds increased gradually. Measuring the cross-sections of HBA NSs milled by a focused ion beam, we have found that hollow and bumpy nanostructures arose from the pore structures of $mSiO_2$ nanotemplates. HBA NSs confine Raman-probe molecules well owing to their hollow structures and have ragged surfaces due to their inward-bumpy morphologies, exhibiting highly efficient surface-enhanced Raman scattering activity.

3.2. Introduction

Plasmonic nanoparticles (NPs) have been actively investigated for their unique optical properties as their localized surface plasmon resonance (LSPR) is excited.[1,2] They can produce an enhanced electromagnetic (EM) field in their vicinity due to their LSPR; in particular, gold NPs have shown a great promise in wide scientific fields, including surface-enhanced Raman scattering (SERS), catalysis, and optoelectronic applications.[3-7] The performance of SERS analysis depends on the degree of 'hotspots', spatially localized regions with extremely strong near-fields, which are critically important to get enhanced performances in the application of plasmonic NPs.[8] Another contribution of Raman signal enhancement is known as the chemical mechanism or charge transfer mechanism, which involves the bonding of the analytes to the substrate surfaces. This bonding increases the polarizability, and thereby Raman scattering intensity.[43] There are generally two structural strategies to introduce strong hotspots in plasmonic NPs; hotspots can be revealed by nanogaps on inter-particle or intra-particle structures[9,10] or created by sharp tips and high-curvature surfaces obtained by morphologically controlled synthesis.[9,11,12] In particular, the structures with high curvatures or rough surfaces have been paid attention to create hotspots.[13-15] Rough or bumpy surfaces which can induce a stronger near-field enhancement in the vicinity of NPs are more desirable than smooth metal surfaces for SERS analysis.[16-18]

Gold nanoshells (NSs) composed of a dielectric core and a gold-metal shell are of great interest due to their tunable LSPR band ranging from the visible to the IR region with superior bio-compatibility.[19,20] Numerous works on the synthesis or tunability of optical properties have been reported.[17,21-23] Especially, for the past two decades, various efforts have been reported to increase the near-field enhancement effect of Au NSs. Kang et al. have reported a seedless and one-step synthetic route to produce bumpy Ag NSs, which can be a NIR-sensitive SERS substrate.[16] Sauerbeck et al. investigated the strong near-field enhancement of an incomplete nanoshell morphology arising from hotspots at gaps between isolated islands[19] while Fan et al. reported the synthesis of high-density Au-Ag alloy nanoislands as secondary nanostructures on the surfaces of Au NSs.[11] However, SERS effect due to contribution from the inner surfaces of Au NSs has been hardly discussed. Clearly, if the inside surfaces of plasmonic nanoshells also have roughness, hotspots can be present at the inner surfaces of Au NSs as well. In addition, if hollow structures are employed, it will be possible to detect biomolecules of an extremely low concentration by the structural trapping effect of Raman probes.[24]

Herein, we report that hollow and inward-bumpy Au (HBA) NSs have been synthesized on mesoporous silica NPs by a templated-growth method. While these nanostructures cannot be obtained by the conventional shell-growth method, they can be synthesized by the sequential reduction-growth method. The synthesis of significantly rough surfaces on the inside as well as the outside of nanoshells has adopted a templated-growth method, which is an easy way to create the shape replica of mesoporous silica templates.[18,25] The method does not use structure-directed molecules such as capping agents or surfactants,

which prevent Raman probes from accessing plasmonic metal surfaces. Also, the method can be employed to fabricate very complex plasmonic structures that are difficult to be produced via a conventional way. In fact, although the synthesis of Au nanostructures using mesopores silica has been already reported, Au nanoshell structures have not been synthesized yet.[26,27] However, we have fabricated hollow and inward-bumpy nanoshells with rough surfaces using expanded silica mesopores as templates. The nanoshells confine Raman-probe molecules well due to their hollow structures and have ragged surfaces due to their inward-bumpy morphologies. Thus, fabricated HBA NSs have revealed large SERS enhancement in the detection of rhodamine 6G.

3.3. Experimental section

3.3.1. Materials

Chemicals were used as purchased without further purification: $HAuCl_4 \cdot 3H_2O$ (*s,* ≥99.9%), tetraethylorthosilicate (TEOS, *l,* ≥99.0%), (3-aminopropyl)triethoxysilane (APTES, *l,* 99%), trimetylbenzene (TMB, *l,* 98.0%), HCl (*aq,* 35%), NaOH (*s,* 99.99%), K_2CO_3 (*s,* 99.5%), $NaBH_4$ (*s,* ≥99.0%), ascorbic acid (*s,* ≥99%), methylene blue (MB, *s,* ≥82%), methyl orange (MO, *s,* 85%) and rhodamine 6G (R6G, *s,* ≥82%) from Sigma Aldrich; HF (*aq,* 48.0-51.0%) from J.T. Baker; NH4OH (*aq,* 25-28%), ethanol (*l,* ≥99.8%) from Daejung Chemicals. Water (>15 MΩ cm^{-1}) purified from an Elga PURELAB Option-S system was used in all the experiments.

3.3.2. Synthesis of pore-expanded mesoporous silica (mSiO₂) NPs

NPs of $mSiO_2$ were fabricated by following the Stober method.[25] 120 mL of a 6 mM aqueous CTAB solution was prepared in a beaker and maintained at 40 ℃ with stirring for 30 min. The beaker was kept under aluminium foil to avoid dust contamination. When 50 mL of ethanol was poured into the CTAB solution, the solution turned cloudy and then became transparent. 1.5 mL of NH4OH was added and then 1.5 mL of TEOS was added dropwise under vigorous stirring. The solution was heated to 60 ℃ and maintained at this temperature for 2 days under gentle stirring. Produced $mSiO_2$ NPs were washed with ethanol by centrifugation (10 min, 7000 rpm, twice) and stored in 20 mL of ethanol. To expand pore sizes, 20 mL of as-prepared $mSiO_2$ NPs, 10 mL of water, and 10 mL of TMB were mixed and stirred vigorously for 10 min.[28,29] The mixture solution was then loaded into a Teflon-lined stainless-steel autoclave with a capacity of 50 mL. The sealed autoclave was put into an oven at 120 ℃ for 2 days and cooled to room temperature. The product was washed with ethanol by centrifugation (10 min, 7000 rpm, twice) and stored in 20 mL of ethanol. To extract CTAB templates, 20 mL of as-prepared pore-expanded $mSiO_2$ NPs and 3 mL of HCl were mixed and stirred gently for 4 h at 70 ℃. Then, the product was washed with ethanol by centrifugation (10 min, 7000 rpm, twice) and stored in 20 mL of ethanol.

3.3.3. Synthesis of Au seeds-decorated mSiO₂ (Au-mSiO₂) NPs

The surfaces of $mSiO_2$ NPs were modified with functional amine groups using APTES.[17] 5.0 mL of as-prepared $mSiO_2$ NPs, 30 mL of ethanol, and 6.0 mL of APTES

were mixed, heated to 60 ℃, and stirred for 4 h. Produced amine-modified $mSiO_2$ NPs were washed twice with ethanol by centrifugation (10 min, 7000 rpm) and redispersed in 10 mL of ethanol. Then, 10 mL of the as-prepared amine-modified $mSiO_2$ colloid, 30 mL of ethanol, and 1.5 mL of 0.02 M $HAuCl_4(aq)$ were mixed, heated to 50 ℃, and stirred for 4 h. Au ions-adsorbed $mSiO_2$ NPs were washed twice with ethanol by centrifugation (10 min, 7000 rpm) and re-dispersed in 30 mL of ethanol. To grow small Au seeds onto $mSiO_2$ NPs, 0.3 mL of 10 mM $NaBH_4(aq)$ was added in 30 mL of the Au ions-adsorbed $mSiO_2$ colloid with vigorous stirring. As the mixture turned brownish red, it was kept for overnight to produce Au-$mSiO_2$ NPs.

3.3.4. Synthesis of Au NSs

To prepare a K-gold solution (Au-plating solution), 3.0 mL of 20 mM $HAuCl_4(aq)$ was added to 80 mL of water containing 20 mg of K_2CO_3 under vigorous stirring.[19] The resulting solution was stored in the dark for overnight. To grow Au NSs, 0.40 mL of the Au-$mSiO_2$ colloid was stirred in a 100 mL vial and then 2.0 mL of the prepared K-gold solution was added and sonicated for 30 s. After 3 min, 0.20 mL of 10 mM ascorbic acid(aq) was added. After 10 min, 2.0 mL of the K-gold solution added again and sonicated for 30 s. After 3 min, 0.20 mL of 10 mM ascorbic acid(aq) was added again. Sonication was employed to aid the growth of Au NSs without using surfactants or capping agents by preventing irreversible aggregation. We will regard the 2.0 mL addition of the K-gold solution followed by the 0.20 mL addition of 10 mM ascorbic acid(aq) as a step. After

seven steps, Au NSs were washed twice with ethanol by centrifugation (10 min, 7000 rpm) and re-dispersed in 10 mL of ethanol.

3.3.5. *Synthesis of hollow and bumpy Au NSs (HBA NSs)*

To etch silica cores, 1.0 mL of a 0.5% ethanoic HF solution was slowly added into 2.0 mL of the as-prepared Au colloid under gentle stirring (~100 rpm). 1.0 mL of the HF solution was added additionally three times with an interval of 10 min. HBA NSs were washed twice with ethanol by centrifugation (10 min, 7000 rpm) and re-dispersed in 5.0 mL of ethanol.

3.3.6. *Measurement of surface-enhanced Raman scattering (SERS)*

R6G, MB, and MO were used as probes for Raman scattering measurement. Representatively, 10 μL of a Au colloid and 10 μL of a 10 μM R6G ethanol solution were consecutively drop-casted onto a p-type Si substrate, which had been already cleaned sequentially with water, acetone, and ethanol. Raman signals of pristine R6G were measured using 10 μL of 0.10 M R6G(ethanol). To test the pH-dependent SERS efficiency of HBA NSs, 0.10 mL of HBA NSs and 0.10 mL of a 10 μM R6G ethanol solution were mixed in a 1 mL vial. Then, the different pH values of the mixture were adjusted by adding a 0.1 M HCl or NaOH solution. Raman spectroscopic analysis was carried out using an OLYMPUS BX41 confocal microscope Raman system equipped with a SLOC Laser

GL532RA-100DPSS laser; a 5.0 mW laser beam of 532 nm was focused to a sample with a spot diameter of 2.0 μm.

3.3.7. Characterization

UV-visible absorption spectra were measured using a Scinco S-3100 spectrophotometer. Transmission electron microscopy (TEM) images were acquired using a Hitachi H-7600 microscope at an accelerating voltage of 100 kV while field emission scanning electron microscopy (FESEM) images were taken with a ZEISS MERLIN Compact microscope operated at an accelerating voltage of 3 kV. Nitrogen adsorption/desorption isotherms were measured with a MicrotracBEL BELSORP MINI-II apparatus. Surface-area calculation was carried out using the BET method and the pore size distribution was calculated according to the BJH method.[32] X-ray diffraction (XRD) patterns were collected with a Bruker New D8 advanced diffractometer using Cu-K$_a$ radiation. A focused ion beam (FIB) was applied using a Carl Zeiss AURIGA apparatus to mill the assembly of as-prepared nanoparticles at ambient temperature. Substrates were fixed with Ag paste after coating samples with Pt for 30 s via ion sputtering (HITACHI, E-1010). A JEOL JEM-2100F microscope at an accelerating voltage of 200 kV was employed to acquire high angle annular dark field-scanning transmission electron microscopy (HAADF-STEM) images and energy dispersive X-ray (EDX) elemental profiles.
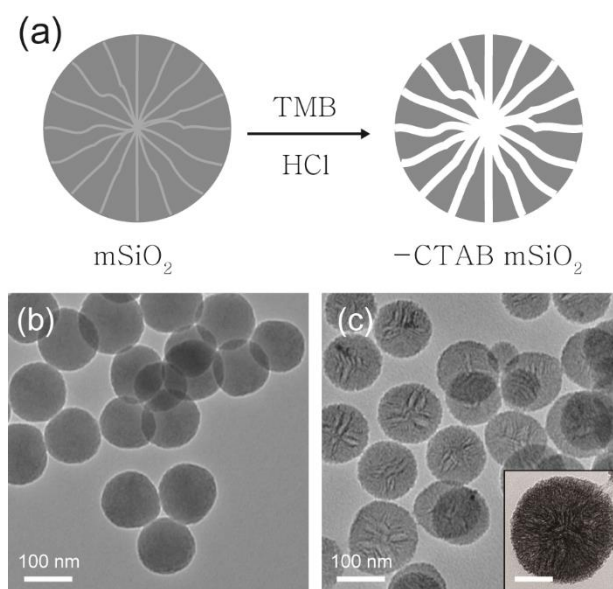
3.4.   Results and discussion

Figure 3-1. (a) Schematic illustration for the fabrication of pore-expanded mSiO$_2$ NPs. (b,c) TEM images of (b) mSiO$_2$ NPs and (c) pore-expanded mSiO$_2$ NPs. The scale bar in the inset of Figure 3-1c indicates 50 nm.
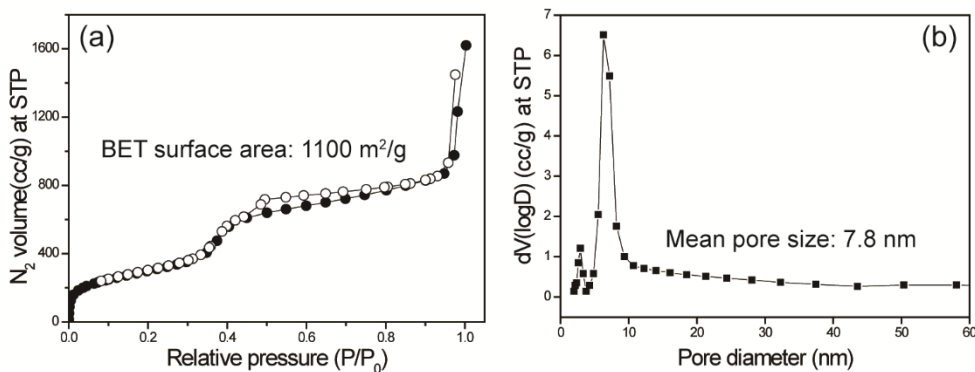
Figure 3-2. (a) N_2 adsorption/desorption isotherms of pore-expanded $mSiO_2$ NPs, where closed and open circles correspond to adsorption and desorption points, respectively. (b) Pore-size distribution plot corresponding to the N_2 adsorption/desorption isotherm of pore-expanded $mSiO_2$ NPs.

The first step for the conventional synthesis of Au NSs requires the decoration of Au seeds onto SiO_2 cores.[20] Thus, prior to the fabrication of Au NSs, we have been concerned about the synthesis of Au-$mSiO_2$ NPs having Au seeds in mesopores. $mSiO_2$ NPs are usually obtained through surfactant-templated synthesis via the Stober method, where CTAB is widely used as a surfactant.[31] It is generally known that pores with sizes of 2-3 nm can be obtained using CTAB templates. We have considered that it is difficult to adsorb functional APTES to the surfaces of typical-size mesopores because the length of APTES is as long as 5-8 nm. To prepare pore-expanded $mSiO_2$ NPs, we have employed an expansion strategy using trimethylbenzene (TMB) as a swelling agent (Figure 3-1).[28,29] The TEM image of pore-expanded $mSiO_2$ NPs shows rather rough surfaces with numerous radial mesopores, compared with that of pristine $mSiO_2$ NPs.[25] The Brunauer-Emmett-Teller (BET) average pore size and the average surface area for pore-expanded $mSiO_2$ NPs

60

were 7.8 nm and 1100 m^2/g, respectively (Figure 3-2). Hereafter, we will call pore-expanded $mSiO_2$ simply as $mSiO_2$.
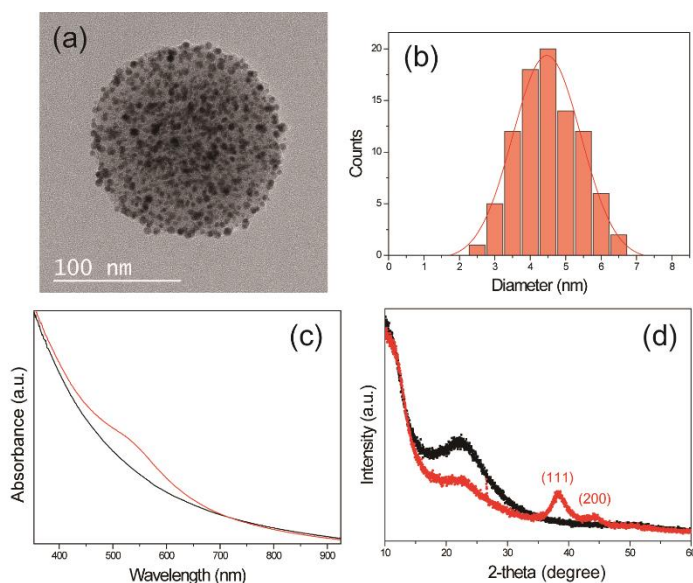

Figure 3-3. (a) HRTEM image of Au-$mSiO_2$ NPs. (b) Size-histogram of Au seed in Au-$mSiO_2$ NPs. (c) UV-vis absorption and (d) XRD data of (black) $mSiO_2$ NPs and (red) Au-$mSiO_2$ NPs.

Although there are two methods to decorate $mSiO_2$ NPs with Au seeds, we have adopted the deposition-precipitation (DP) method because tetrakis(hydroxymethyl)phosphonium chloride-mediated Au seeds cannot enter into mesopores easily.[21] We have fabricated Au seeds-decorated $mSiO_2$ (Au-$mSiO_2$) NPs by the $NaBH_4$ chemical reduction of Au ions via a modified DP method. Our chemical reduction method is advantageous in creating small Au seeds during a relatively short reaction time. The HRTEM image of Au-$mSiO_2$ NPs in

Figure 3-3a reveals that numerous Au seeds with an average diameter of 4.5 nm are adsorbed on the surfaces of mSiO$_2$ NPs, suggesting that APTES molecules have enabled us to fabricate evenly distributed Au seeds with uniform sizes (Figure 3-3b). The UV-vis absorption spectra of Figure 3-3c indicate that Au-mSiO$_2$ NPs have a shoulder peak at 550 nm, suggesting that Au seeds have plasmonic properties as well. Wide-angle X-ray diffraction analysis was used to confirm the adsorption of Au seeds (Figure 3-3d). While a 22º broad peak confirms the amorphous nature of mSiO$_2$ NPs,[32] the characteristic XRD peaks of Au seeds were clearly observed at 39º ((111) planes) and 42º ((200) planes) for Au-mSiO$_2$ NPs (JCPDS No. 65-2870). The full width at the half maximum (FWHM) of an XRD peak is affected by particle sizes according to the Scherrer equation: D = K λ / (β cosθ), where D is the average particle size, K is a constant equal to 0.94, λ is the Cu-K$_\alpha$ radiation wavelength (0.154 nm), β is the FWHM of a diffraction peak, and θ is the diffraction angle. The calculated average size of Au seeds is 2.9 nm, determined from (111) planes using the Scherrer equation.
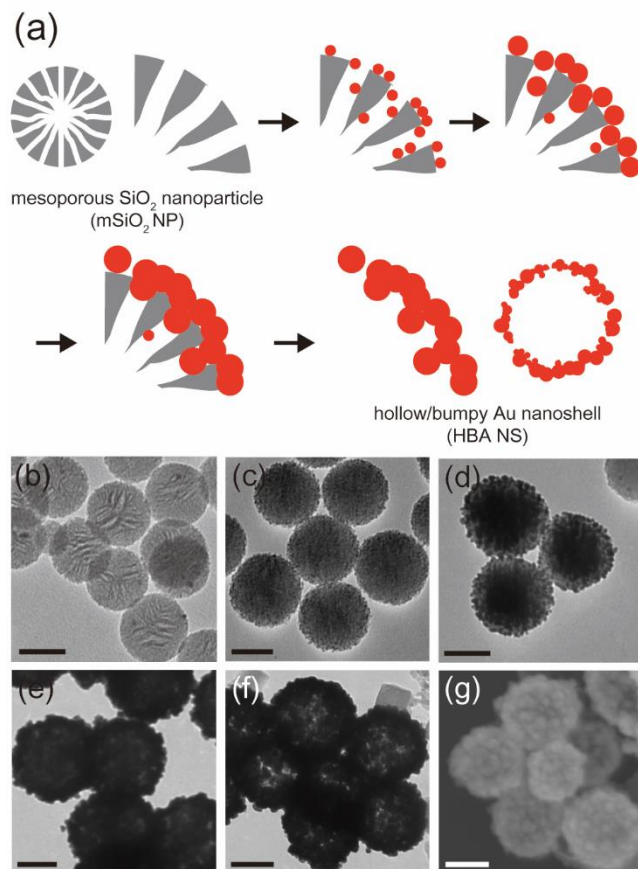
Figure 3-4. (a) Schematic illustration for the fabrication of HBA NS. (b-f) TEM images of progressively growing (b) mSiO$_2$ NPs, (c) Au-mSiO$_2$ NPs, (d) growth intermediates, (e) Au NSs, and (f) HBA NSs. (g) SEM image of HBA NSs. Each scale bar indicates 100 nm.

Figure 3-4a illustrates the synthesis of HBA NSs. Through the direct growth of Au seeds on mSiO$_2$ surfaces, Au-mSiO$_2$ NPs have been firstly synthesized (Figure 3-4b and 4c). The followed sequential reduction of gold ions has grown the Au seeds of Au-mSiO$_2$ NPs

63

progressively until Au seeds coalesce and fuse together (Figure 3-4d and 4e). Because the Au seeds are located partly at the inner surfaces of mesopores, produced Au NSs have inherent nanobumps (Figure 3-4e). Finally, as silica cores were etched using a HF solution, Au NSs were transformed into hollow and bumpy Au nanoshells (HBA NSs, Figure 3-4f). The SEM image of Figure 3-4g reveals that the outside surfaces of HBA NSs have inherent nanobumps indeed, although it is difficult to observe the inner morphologies of HBA NSs by measuring ordinary TEM or SEM images.
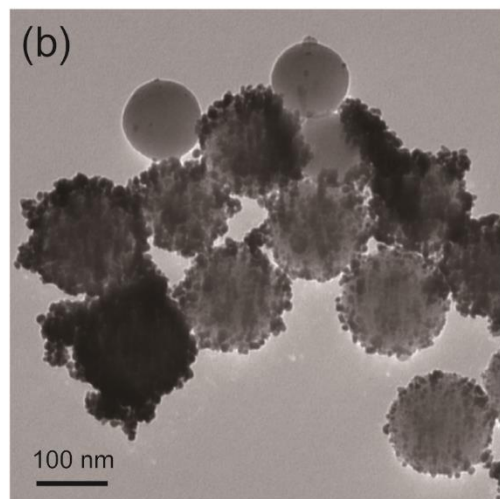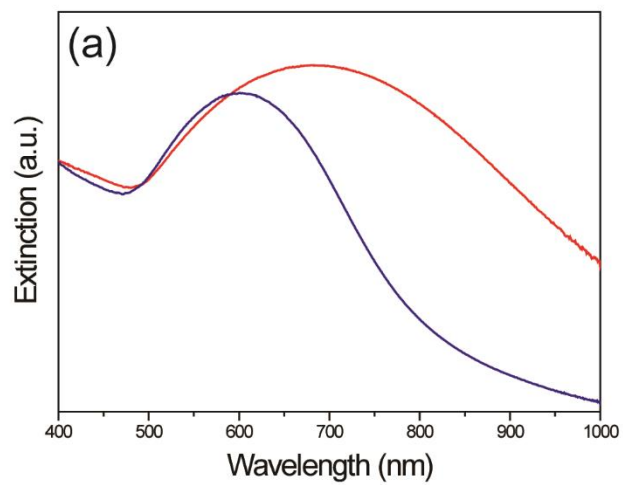
Figure 3-5. (a) UV-vis extinction spectra of Au NPs synthesized by (blue) the conventional method and (red) our sequential reduction method. (b) TEM image of irregular Au NPs synthesized by the conventional method.
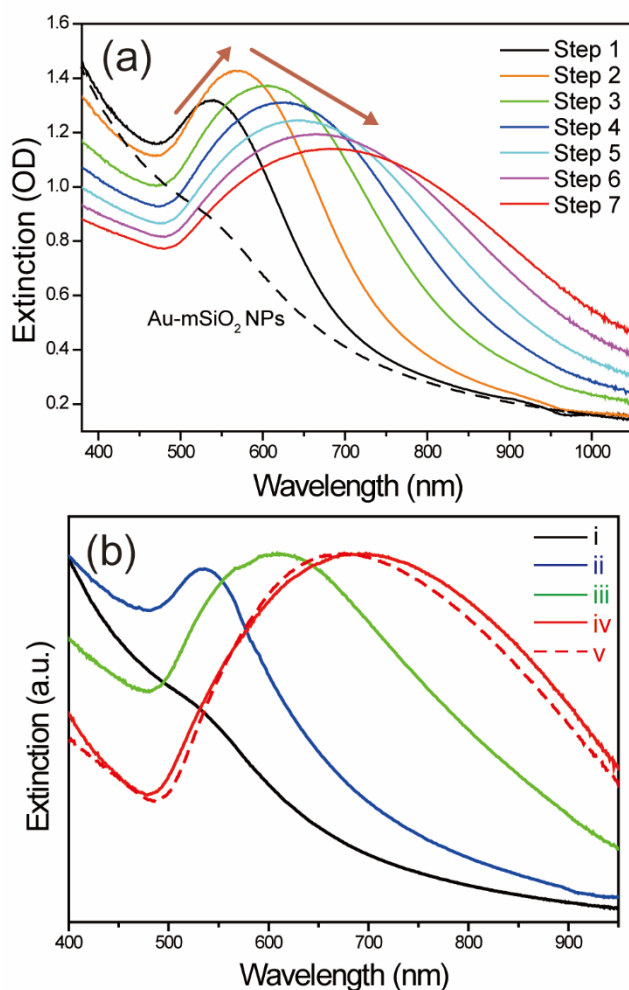
Figure 3-6. (a) Extinction spectra measured at successive steps during the growth reaction of Au NSs. (b) UV-vis extinction spectra of (i) Au-mSiO$_2$ NPs, (ii) step-1 NPs, (iii) step-4 NPs, (iv) Au NSs, and (v) HBA NSs.

Although it was generally reported[19,20,33,34] that Au NSs could be fabricated by reducing gold ions at one go, we could not use the conventional reduction method to produce Au

NSs. However, we fabricated Au nanostructures as well via the conventional mehtod as a comparative experiment; 0.40 mL of the Au-mSiO$_2$ NPs colloid was added to 14 mL of the K-gold solution, which was then added with 1.4 mL of 10 mM ascorbic acid(*aq*). Figure 3-5a shows that the LSPR characters of Au NSs are more prominent in the UV-vis extintion spectrum of Au NSs fabricated by our sequential reduction method than in the spectrum of Au nanostructures synthesized by the conventional method. Figure 3-5b shows that Au nanostructres fabricated by the conventional method have irregular shapes. However, Au NSs prepared by the sequential reduction method, where the conventional method was divided into 7 steps, have well-defined shapes. Figure 3-6a shows that LSPR shifted to the red and its bandwidth became broader progessively with the increase of growth steps. The LSPR peak of step-1 NPs is remarkable at 550 nm, supporting that Au seeds have grown in sizes. This trend was observed until the sequential reduction of the step 2 took place. The reasons why we should use the sequential reduction method are as follows. A periodically sequential sonication process is essential to introduce Au ions well in the mesopores. Also, the sequential reduction method without using surfactants or capping agents prevents Au NPs from irreversible aggregation.
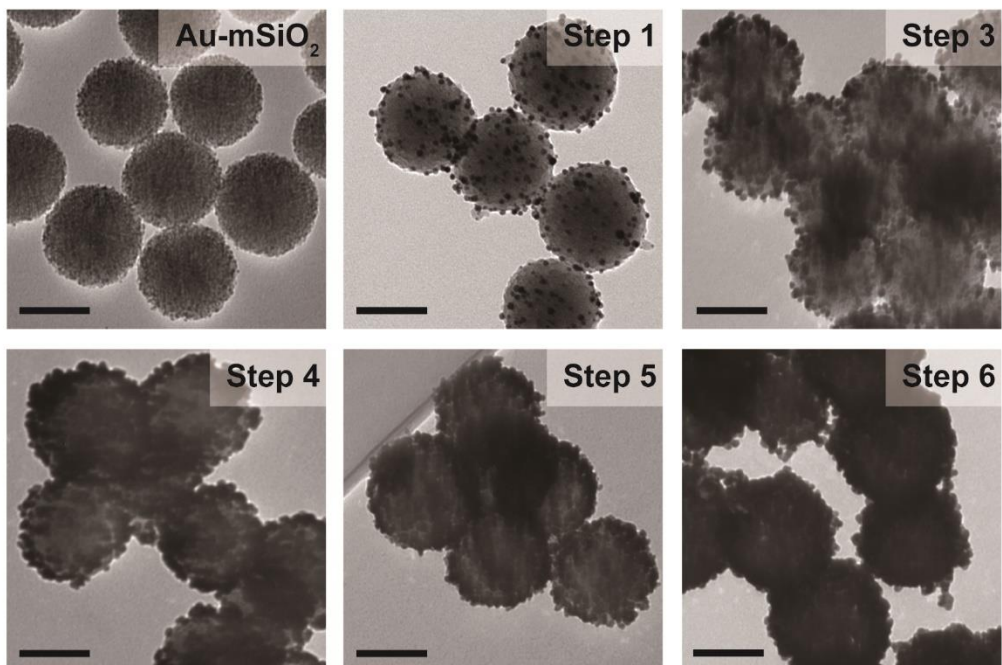
Figure 3-7. TEM images of progressively growing Au NSs. Each scale bar indicates 100 nm.

During seven successive steps, the LSPR peak of Au nanostructures shifted progressively toward a longer wavelength as the sizes of Au seeds increased further. The small Au seeds were likely to collide and coalesce with neighbouring Au seeds to form nanoshells (Figure 3-7). The morphologies of Au NSs formed on $mSiO_2$ templates reveal that nanoshell structures are well-defined and uniform. Au NSs prepared at the step 7 show the LSPR peak at 697 nm, suggesting that their nanoshell structures are not completely closed. It has been generally reported that Au NSs having a fully closed shell structures with an average diameter of less than 200 nm have the LSPR peak at $\geq$800 nm.[19,20] However, as-synthesized Au NSs have shown the LSPR band at 697 nm, so the morphologies of Au NSs were inferred to be not completely closed, as shown in Figure 3-

4f. We did not control the thickness of Au NSs. If we conduct further reduction steps, an increase in shell thickness can be achieved and completely closed-nanoshell morphologies can be obtained as well. There are some attractive reasons for the synthesis of incompletely closed-nanoshell morphologies. Not only Raman probe molecules are easily accessible to inherent pore structures[17] but also high near-field enhancement is induced well at incomplete nanoshell morphologies.[19] Finally, as silica cores were etched using a HF solution, Au NSs were transformed into HBA NSs. The extinction spectrum of HBA NSs (Figure 3-6b) is slightly blue-shifted compared to that of Au NSs, suggesting that the etching of silica cores has reduced the sizes of Au NSs. We have investigated the particle-size distribution histograms of Au nanostructures shown in Figure 3-6b. While the average diameter of as-prepared $mSiO_2$ NPs is 130 nm, the average particle diameters of synthesized Au nanostructures range from 138 to 161 nm, suggesting that the average shell thickness of Au NSs is about 15 nm (Figure 3-8). The average diameter of HBA NSs is 150 nm, which is slightly shorter than that of Au NSs (161 nm), as predicted with the extinction spectra of Figure 3-6b.
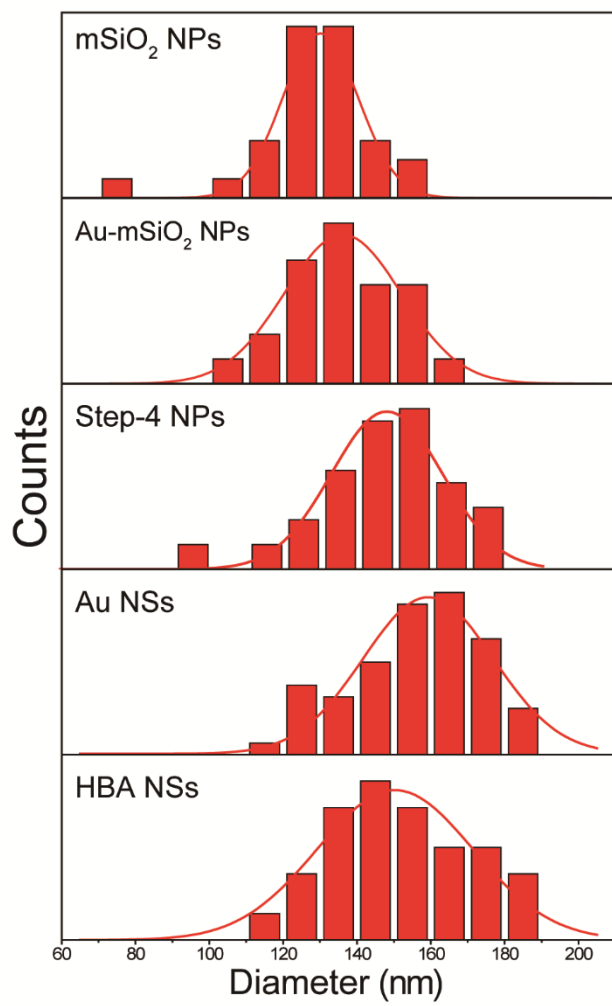
Figure 3-8. Particle size-distribution histograms of respectively indicated samples.
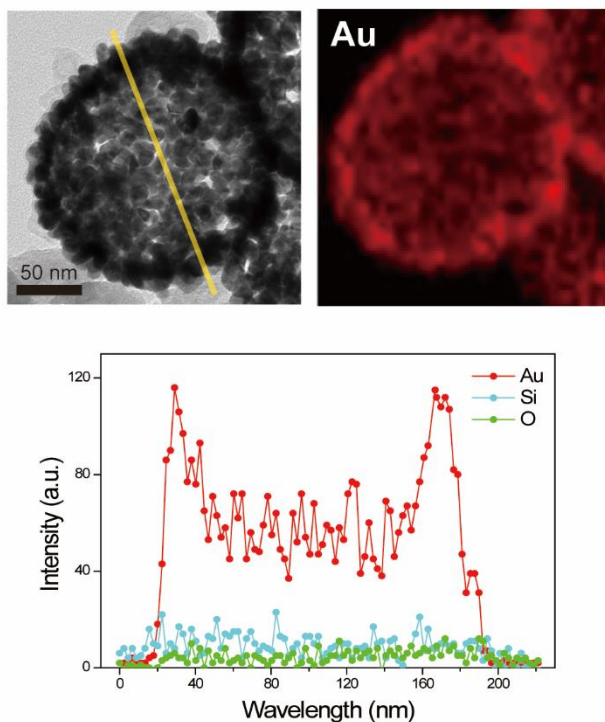
Figure 3-9. (top) HADDF-STEM image and EDX elemental map of a HBA NS. (bottom) Line-scanned elemental profiles of HBA NS.

For the further characterization of HBA NSs, elemental compositions and distributions have been determined by measuring an EDX elemental map and line-scanned elemental profiles, as well as a HAADF-STEM image. The HAADF-STEM image and the elemental map of Figure 3-9 reveal that a HBA NS has a hollow, porous, and bumpy nanoshell structure. Because Au seeds were located partly at the inner surfaces of mesopores, produced Au NSs have inherent inward nanobumps. In particular, two characteristic sharp peaks of the line-scanned gold elemental profile in Figure 3-9 indicate that the HBA NS is

hollow indeed. Furthermore, the fluctuating ripple peaks of the gold elemental profile suggest that the HBA NS has a porous structure. The relatively very small elemental intensities of Si and O in Figure 3-9 indicate that the residual amount of $mSiO_2$ in the HBA NSs is negligible. However, it is difficult to observe the inner morphologies of HBA NSs by measuring HAADF-STEM images. Furthermore, TEM-based tomographic analysis is not suitable for inner shapes of Au nanostructures because noble-metal nanostructures hardly transmit an electron beam.[35]
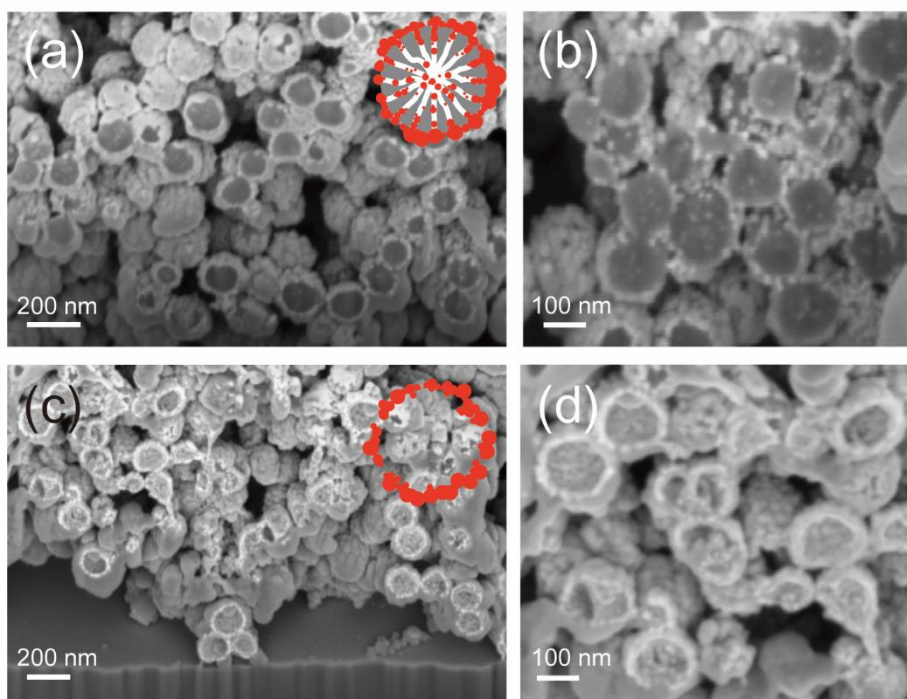

Figure 3-10. Cross-section SEM images of (a,b) Au NSs and (c,d) HBA NSs obtained by the focused-ion-beam milling method.

For the precise analysis of the inner morphologies of HBA NSs, we have inves
tigated the cross-sections of NSs milled by a focused ion beam. To mill numerou
s Au nanostructures via one process, we drop-casted the Au NSs colloid several t
imes to heap Au NSs up at the same spot. In addition, to prevent substrates fro
m slipping down, we fixed them with a Ag-paste adhesive. The beam-milled cros
s-sections of Au NSs in Figure 3-10a and 10b display bright Au NSs as well as
relatively dark silica cores. It is noteworthy that Au seeds were embedded in mSi
O_2 NPs. The embedded morphologies arose from Au seeds formed at the deeply i
nside surfaces of mesopores during the fabrication process of Au-mSiO$_2$ NPs. Dee
ply located Au seeds grew hardly because gold ions near deeply located Au seed
s could not react well with reducing agents. Figure 3-10c and 10d show hollow and
inward-bumpy nanoshell structures, which could not be observed in the SEM images of
Au NSs because inner shapes were screened by silica cores. We consider that hollow and
bumpy structures arose from the pore structures of mSiO$_2$ templates. HBA NSs are
expected to confine Raman-probe molecules well due to their hollow structures. Also,
because their inner surfaces are ragged, the nanoshells would exhibit high plasmonic
properties. The cross sections of HPA NSs look slightly elliptical because a strong Ga-ion
beam has thermally distorted Au nanostructures.[36] We are reporting the inward-bumpy
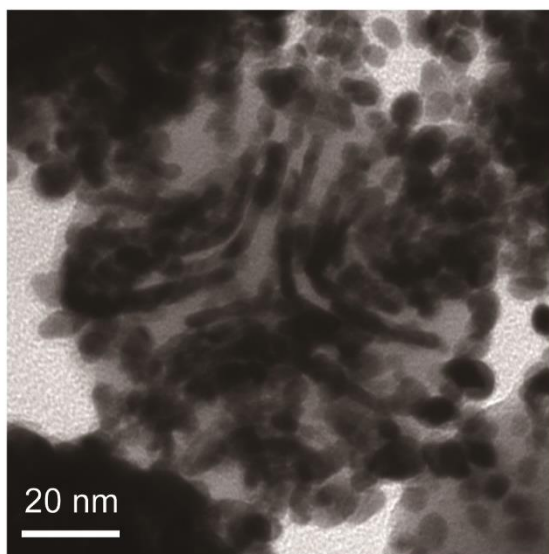surfaces of Au NSs for the first time to our knowledge.

73

Figure 3-11. TEM image of inward grown Au nanotips in mesoporous silica NPs.

A few interesting aspects have been observed during our TEM study. We have identified inward-grown gold nanotips located in mesopores (Figure 3-11). We have already described with Figure 3-10 that Au seeds were embedded in the mesopores of $mSiO_2$ NPs. The Au seeds grew to form nanorods in the mesopores of $mSiO_2$ NPs. The fabrication of nanoparticles-embedded SiO_2 NPs using mesopore channels as templates has already been reported.[25,37,38] If both of gold ions and reducing agents could move freely in the mesopores of $mSiO_2$ NPs, it would be possible to fabricate more functional Au NSs having inward-grown (convergent) nanotips.
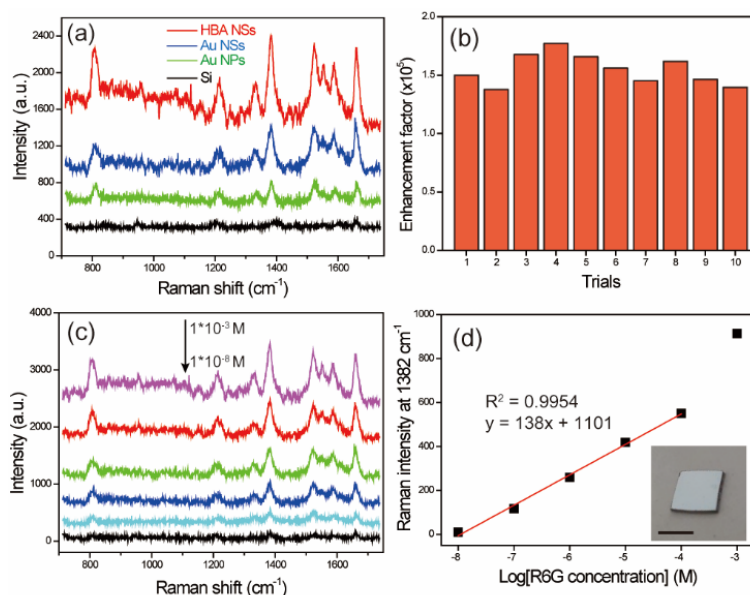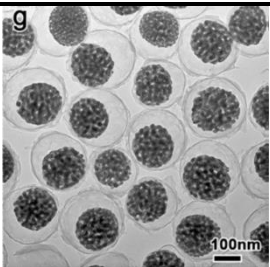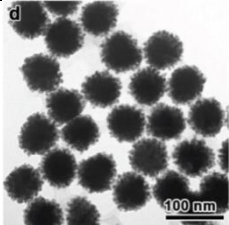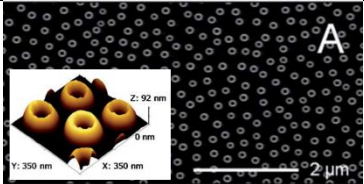
Figure 3-12. (a) SERS spectra of 10 μM R6G(*ethanol*) adsorbed on HBA NSs, Au NSs, Au NPs, and Si. Note that 0.10 M R6G(*ethanol*) was used to record the Raman signal of the Si substrate. (b) The SERS enhancement factors of HBA NSs acquired via measuring relatvie Raman intensities at 1382 cm^{-1}. (c) SERS sepctra of R6G at concentrations ranging from 10^{-8} M to 10^{-3} M   (d) SERS intensity of R6G at 1382 cm^{-1} as a function of the logarithm of the R6G concentration. The inset shows a representative optical image of a HBA NSs-R6G SERS substrate on a Si piece (scale bar: 1 cm)

The SERS capabilities of HBA NSs, Au NSs, and Au NPs (having an average diameter of 150 nm) have been investigated using R6G as a Raman probe with excitation at 532 nm (Figure 3-12); the Au NPs were prepared using the seed-mediated growth method.[39] The peaks in the region between 800 and 1700 cm^{-1} arose from the bending modes of C-H and the stretching modes of the carbon skeleton. The SERS enhancement factors (EF) of Au

nanostructures acquired by measuring relative Raman intensities were 4.9×10^4 for Au NPs, 8.0×10^4 for Au NSs, and 1.8×10^5 for HBA NSs. Note that the SERS efficiency of HBA NSs was 2.3 times greater than that of Au NSs and 3.7 times larger than that of Au NPs. The EF value of HBA NSs has also been compared with the reported EF values of various plasmonic nanoparticles in Table 3-1.

Table 3-1. SERS EFs of various plasmonic nanoparticles.

Entry	EF	Excitation wavelength, Raman probe	Reference
Porous Au-Ag nanospheres	1.3×10^7	633 nm, crystal violet	ref. 24
Island-on-Au NSs	5.0×10^6	633 nm, crystal violet	ref. 11
Au nanorings array	5.0×10^5	532 nm, 4-aminothiophenol	ref. 41

 HBA NSs	1.8×10^5	532 nm, R6G	this work
 Ag nanoplates	1.7×10^5	633 nm, R6G	ref 42
 Au nanorods	1.7×10^5	785 nm, rose bengal	ref. 40
 Hollow and porous Au NSs	1.0×10^5	532 nm, methylene blue	ref. 17
 Au-mSiO$_2$ hybrid microspheres	3.2×10^3	633 nm, crystal violet	ref. 22

The largest SERS enhancement of HBA NSs has been attributed to hollow structures confining probe molecules as well as to inward-bumpy structures exhibiting high plasmonic properties. Meanwhile, we also tried to understand SERS enhancement from the perspective of the LSPR-mediated charge transfer mechanism. The charge transfer mechanism involves the bonding of the Raman probes to the surfaces of substrates. The mechanism is also called as the 'first layer effect'; Raman probes and metal surfaces need to be in close contact with each other.[44] Because Au NSs with rough surfaces have higher surface area than Au NPs with smooth surfaces, Au NSs have superb first-layer effect. However, as silica cores were etched using a HF solution, HBA NSs show the largest SERS enhancement owing to the hollow and inward-bumpy structures, which were not seen in Au NSs having silica cores. Furthermore, high SERS reproducibility has been explored by comparing Raman signals measured at ten different spots (Figure 3-12b). The relative standard deviation of the ten measured Raman intensities has been calculated as 13%, indicating that HBA NSs have outstanding SERS reproducibility. The SERS spectra of R6G at concentrations ranging from 10^{-8} to 10^{-3} M using HBA NSs as substrates are shown in Figure 3-12c. It can be observed from the SERS spectra that the intensities of characteristic peaks decrease with the decrease of R6G concentrations. The peak at 1382 cm^{-1} could be observed when the R6G concentration was as low as 1×10^{-8} M. Hence, the detection limit of HBA NS substrates has been estimated as 10^{-8} M of R6G. The logarithm of the Raman intensity of R6G at different concentrations ranging from 10^{-3} M to 10^{-8} M was plotted in Figure 3-12d to obtain a standard calibration curve with a correlation coefficient of 0.9954, suggesting that a good linear response was found to R6G

78

concentrations ranging from 10^{-8} to 10^{-4} M. We have also tested the pH-dependent SERS

stability of HBA NSs (Figure 3-13).
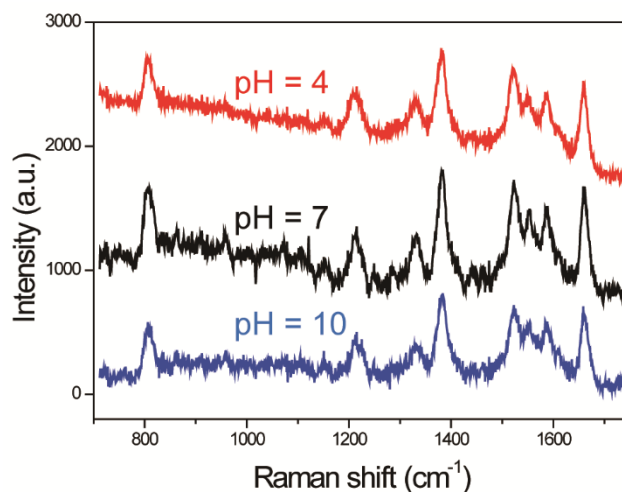
Figure 3-13. SERS spectra of 10 μM R6G(ethanol) adosrbed on HBA NSs at different pH values.
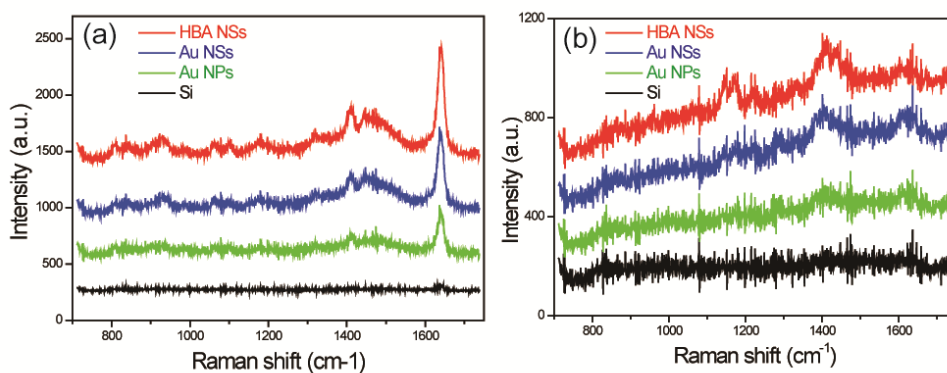
Figure 3-14. SERS spectra of (a) 10 μM MB(ethanol) and (b) 10 μM MO(*aq*) adsorbed on HBA

NSs, Au NSs, Au NPs, and Si. Note that 0.10 M MB(ethanol) and 0.10 M MO(*aq*) were used to

record the Raman signals of the Si substrate.

The SERS intensities and frequencies of R6G were almost invariant regardless of pH variation, indicating that the molecular structures of R6G[46] and the morphologies of HBA NSs were stable at all the investigated pH values. To demonstrate the universality of HBA NSs as SERS substrates, we have investigated the SERS efficiency using MB and MO as Raman probes with excitation at 532 nm. Figure 3-14a shows that the SERS efficiency of HBA NSs is 1.4 and 1.9 times greater than the respective ones of Au NSs and Au NPs for the MB Raman probe while Figure 3-14b indicates that the SERS efficiency of HBA NSs is 1.3 and 1.6 times larger than the respective ones of Au NSs and Au NPs for the MO Raman probe. Thus, Figures 3-12 and 3-14 indicate that although the SERS enhancement factor of HBA NSs depends on Raman probes, HBA NSs can be used universally as Raman substrates owing to their hollow and inward-bumpy morphologies.

3.5. Conclusions

We have fabricated hollow and inward-bumpy Au (HBA) nanoshells (NSs) of 150 nm diameters with an average thickness of 15 nm using expanded silica mesopores as templates. Because some Au seeds were located at the inner surfaces of silica mesopores, produced Au NSs have inherent inward-grown nanobumps. While these nanostructures could not be obtained by the conventional shell-growth method, they have been synthesized by a sequential-reduction growth method. During seven successive reduction steps, the LSPR peak of Au nanostructures shifted progressively toward a longer wavelength as the sizes of Au seeds increased gradually. Measuring the cross sections of HBA NSs milled by a focused ion beam, we have   found that hollow and bumpy structures arose from the pore structures of $mSiO_2$ templates. HBA NSs confine Raman-probe molecules well owing to their hollow structures and have ragged surfaces due to their inward-bumpy morphologies, thus exhibiting highly efficient SERS activity.

3.6. Acknowledgements

3.7. References

1   J. Olson, S. Dominguez-Medina, A. Hoggard, L.-Y. Wang, W.-S. Chang and S. Link. Chem. Soc. Rev., 2015, 44, 40.

2   S. T. Kochuveedu and D. H. Kim, Nanoscale, 2014, 6, 4966.

3   G. Jean-Michel and C. Antonino. Nat. Comm. 2017, 8, 16095.

4   S.-Y. Ding, J. Yi, J.-F. Li, R. Panneerselvam, B. Ren, D.-Y. Wu and Z.-Q. Tian. Nat. Rev. Mater., 2016, 1, 1.

5   L. Zhen, Y. Zhongbo, P. Bo, C. Cuong, Z. Chao, Y. Hongjun, X. Qihua, L. Zhiyuan and F. Jixiang. Adv. Mater., 2014, 26, 2431.

6   Makarov, S. V.; Milichko, V. A.; Mukhin, I. S.; Shishkin, I. I.; Zuev, D. A.; Mozharov, A. M.; Krasnok, A. E.; Belov, P. A. Laser Photonics Rev., 2016, 10, 91.

7   Kim, J. K.; Jang, D.-J. J. Mater. Chem. C, 2017, 5, 6037.

8   Ming, L,; Scott, K. C.; Nianqing, W. Analyst 2015, 140, 386.

9   Nam, J. M.; Oh, J. W.; Lee, H.; Suh, Y. D. Acc. Chem. Res., 2016, 49, 2746.

10   Zhuo, W.; Dong, Z.; Gu, Y.; Chang, Y.-H.; Zhang, L.; Li, L.-J.; Zhao, W.; Eda, G.; Zhang, W.; Gustavo, G.; Stefan, A. M.; Joel, K. W. Y.; Cheng-Wei, Q.; Andew, T. S. W. Nat. Comm., 2016, 7, 11283.

11   Fan, Q.; Liu, K.; Feng, J.; Wang, F.; Liu, Z.; Liu, M.; Yin, Y.; Gao, C. Adv. Func. Mater., 2018, 28, 41.

12   Sánchez-Iglesias, A.; Barroso, J.; Solís, D. M.; Taboada, J. M.; Obelleiro, F.; Pavlov, V.; Chuvilin, A.; Grzelczak, M. J. Mater. Chem. A, 2016, 4, 7045.

13   Novikov, S. M.; Sánchez-Iglesias, A.; Schmidt, M. K.; Chuvilin, A.; Aizpurua, J.; Grzelczak, M.; Liz-Marzán, L. M. Part. Part. Sys. Character., 2014, 31, 77.

14   Yuan, H.; Khoury, C. G.; Hwang, H.; Wilson, C. M.; Grant, G. A.; Vo-Dinh, T. Nanotechnology 2012, 23, 075102.

15   Sanchez-Gaytan, B. L.; Swanglap, P.; Lamkin, T. J.; Hickey, R. J.; Fakhraai, Z.; Link, S.; Park, S.-J. J. Phys. Chem. C, 2012, 116, 10318.

16   Kang, H.; Yang, J.-K.; Noh, M. S.; Jo, A.; Jeong, S.; Lee, M.; Lee, S.; Chang, H.; Lee, H.; Jeon, S.-J.; Kim, H.-I.; Cho, M.-H.; Lee, H.-Y.; Kim, J.-H.; Jeong, D. H.; Lee, Y.-S. J.

Mater. Chem. B, 2014, 2, 4415.

17 Park, T. H.; Jang, D. J. Nanoscale 2018, 10, 20108.

18 Zhao, J.; Long, L.; Weng, G.; Li, J.; Zhu, J.; Zhao, J.-W. J. Mater. Chem. C, 2017, 5, 12678.

19 Sauerbeck, C.; Haderlein, M.; Schurer, B.; Braunschweig, B.; Peukert, W.; Taylor, R. M. K. ACS Nano, 2014, 8, 3088.

20 James, C. Y.; Kah, N. P.; Rachel C. Y.; Wan, J. S.; Timothy, W.; Subodh, M.; Iman, A.; Colin, S.; Malini, O.; Gold Bullet., 2008, 41, 23.

21 Wang, Y. C.; Rheaume, E.; Lesage, F.; Kakkar, A. Molecules, 2018, 23.

22 Son, H. Y.; Kim, K. R.; Lee, J. B.; Kim, T. H. L.; Jang, J.; Kim, S. J.; Yoon, M. S.; Kim, J. W.; Nam, Y. S. Sci. Rep., 2017, 7, 14728.

23 Mann, D.; Nascimento-Duplat, D.; Keul, H.; Moller, M.; Verheijen, M.; Xu, M.; Urbach, H. P.; Adam, A. J. L.; Buskens, P. Plasmonics, 2017, 12, 929.

24 Liu, K.; Bai, Y.; Zhang, L.; Yang, Z.; Fan, Q.; Zheng, H.; Yin, Y.; Gao, C. Nano Letters 2016, 16, 3675.

25 Sanz-Ortiz, M. N.; Sentosun, K.; Bals, S.; Liz-Marzan, L. M. ACS Nano, 2015, 9, 10489.

26 Tew, L. S.; Cai, M. T.; Lo, L. W.; Khung, Y. L.; Chen, N. T. Materials, 2018, 11, 7.

27 Elbialy, N.; Mohamed, N.; Monem, A. S. Micro. Meso. Mater., 2014, 190, 197.

28 Na, H. K.; Kim, M. H.; Park, K.; Ryoo, S. R.; Lee, K. E.; Jeon, H.; Ryoo, R.; Hyeon, C.; Min, D. H. Small, 2012, 8, 1752.

29 Kim, S.; Na, H.-K.; Won, C.; Min, D.-H. RSC Adv, 2016, 6, 27143.

30 Kim, J. K.; Lee, K. S.; Park, T.-H.; Jeong, D.-W.; Kim, Z. H.; Jang, D.-J. Opt. Laser Technol., 2019, 112, 151.

31 Davidson, M.; Ji, Y.; Leong, G. J.; Kovach, N. C.; Trewyn, B. G.; Richards, R. M. ACS Appl. Nano Mater., 2018, 1, 4386.

32 Kayal, U.; Mohanty, B.; Bhanja, P.; Chatterjee, S.; Chandra, D.; Hara, M.; Kumar Jena, B.; Bhaumik, A. Dalton Trans., 2019, 48, 2220.

33 Wang, H.; Liu, X.; Li, X.; Lu, W.; Jiang, L. Chem. Select, 2016, 1, 659.

34 Tharion, J.; Satija, J.; Mukherji, S. RSC Adv., 2014, 4, 3984.

35 Song, H.; Yang, Y.; Geng, J.; Gu, Z.; Zou, J.; Yu, C. Adv. Mater., 2018, 1801564

36 Park, M.-Y.; Lim, S.; Lee, S.-W.; Park, S.-E. Macro. Res., 2009, 17, 307.

37 Li, Z.; Kübel, C.; Parvulescu, V. I.; Richards, R. ACS Nano, 2008, 2, 1205.

38 Chen, P. J.; Hu, S. H.; Fan, C. T.; Li, M. L.; Chen, Y. Y.; Chen, S. Y.; Liu, D. M. Chem. Comm., 2013, 49 (9), 892.

39 Tian, F.; Bonnier, F.; Casey, A.; Shanahan, A. E.; Byrne, H. J. Anal. Methods, 2014, 6, 9116.

40 Gabudean, A. M.; Focsan, M.; Astilean, S. J. Phys. Chem. C, 2012, 116, 12240.

41 Ye, J,; Hutchison, J. A,; Uji-i, H.; Hofkens, J.; Lagae, L.; Maes, G.; Borghs, G.; Dorpe, P. V. Nanoscale 2012, 4, 1606.

42 Tan, T.; Tian, C.; Ren, Z.; Yang, J.; Chen, Y,; Sun, L.; Li, Z.; Wu, A.; Yin, J.; Fu, H. Phys. Chem. Chem. Phys., 2013, 15, 21034.

43 Goul, R.; Das, S.; Liu, Q.; Xin, M.; Lu, R.; Hui, R.; Wu, J. Z. Carbon, 2017, 111, 386.

44 Kavitha, C.; Bramhaiah, K.; John, N. S.; Ramachandran, B. E. Chem. Phys. Lett., 2015, 629, 81.

45 Hou, M.; Huang, Y.; Ma, L.; Zhang, Z. Nano. Res. Lett., 2015, 10, 437

46 Li, P.; Zhou, X.; Liu, H.; Yang, L.; J. Raman spec., 2013, 44, 999.

47 Li, C.-H.; Jamison, A. C.; Rittikulsittichai, S.; Lee, T.-C.; Lee, T. R. ACS Appl. Mater. Inter., 2014, 6, 19943.

Chapter 4. Surface-enhanced Raman scattering and photothermal effect of hollow Au nanourchins with well-defined cavities

† This was submitted to *New J. Chem.* by Joon Ki Kim, Tae-Hyeon Park, and Du-Jeon Jang.

4.1. Abstract

We have prepared genuinely hollow Au nanourchins (HANUs) using SiO_2 nanoparticles (NPs) as hard templates. Ag-SiO_2 NPs were fabricated via amine-assisted reduction. Then, Au nanourchins (ANUs) were synthesized by the galvanic replacement reaction of Ag-SiO_2 NPs using L-3,4-dihydroxyphenylalanine (DOPA) as a reductant and a capping agent. The silica cores of ANUs were etched using HF*(aq)* to produce HANUs. Measuring cross sections, we have found that HANUs have well-defined hollow morphologies. Compared with nanourchins made via DOPA-mediated reduction, HANUs hardly contain residual silver because very tiny silver seeds were used as the initiation sites of galvanic replacement. HANUs have revealed large surface-enhanced Raman scattering enhancement and a significant photothermal effect under a weak illumination.

4.2. Introduction

Hollow nanoparticles (NPs), a class of nanostructures having cavities inside nanoshells (NSs), have attracted growing attention due to their unique structural properties.[1,2] Some intrinsic features of hollow nanostructures, such as large surface areas, low densities, and immense inner void spaces, have been harnessed in a variety of applications. For instance, hollow Pt nanospheres are twice as active as solid Pt NPs for methanol oxidation. Hollow NPs can be employed as nanoscale containers to load small organic molecules such as pharmaceutical compounds, proteins, and DNA. Also, plasmon resonances of noble metal NSs can be effectively tuned to a wavelength ranging from the visible to the infrared region by varying the ratio of cavity diameter to metallic shell thickness.[3-6] Diverse fabrication strategies of hollow nanostructures have been based on two classifications: self-organization and sacrificial templating.[1] The galvanic replacement reaction, a class of sacrificial template methods, is a redox process between two metals with distinct reduction potentials. The reaction provides a simple and versatile route to fabricate a range of advanced multifunctional NPs with plasmonic cavities and porous walls.[7-9]

Controlling surface morphologies of nanostuructures is a key issue in enhancing their structural and optical properties. Roughnesses, spikes, and tips in nanoscale are interesting structures owing to the anisotropic enhancement of the electromagnetic field, an effect similar to the lightning rod effect.[10-16] Their local plasmonic features allow the modulation of localized surface plasmon resonance (LSPR) modes by tuning their lengths, densities, and aspect ratios.[17-21] They have shown a great promise in surface-enhanced Raman

scattering (SERS), optoelectronic applications, and catalysis.[10,11,22-26] Several years ago, Liu *et al.* reported a highly sensitive SERS performance arising from aggregated hollow Au-Ag alloy nanourchin (HAAA-NU) substrates.[27] The nanourchins (NUs) were synthesized *via* a seed-mediated growth method using L-3,4-dihydroxyphenylalanine (DOPA) as a reductant as well as a capping agent.[28] The NUs have attracted growing attention due to their hieracrchical and functional structures. You *et al.*[25] have reported that controlling the morphologies of Pt–Au NUs can provide a great opportunity to increase their catalytic activity and to improve their durability at the same time. The Pt–Au NUs have been demonstrated to have an ultrahigh density of sharp tips and a uniform coating of 2 nm Pt NPs. In addition, Ong *et al.*[10] have reported a seed-mediated synthesis of multibranched Au NPs using L- or D-DOPA for active cancer targeting. Here, a few things for the synthesis of the reported NUs should be improved for further applications. Firstly, it is not sure that the reported NUs have hollow morphologies actually; the real sizes of cavities have not been reported yet. Secondly, as-synthesized HAAA-NUs have some residual amounts of silver because large Ag NPs of tens nm in diameters were used as sacrificial templates. Silver can dissolve rather easily in aquous solutions so that HAAA-NUs are not bio-comparative.
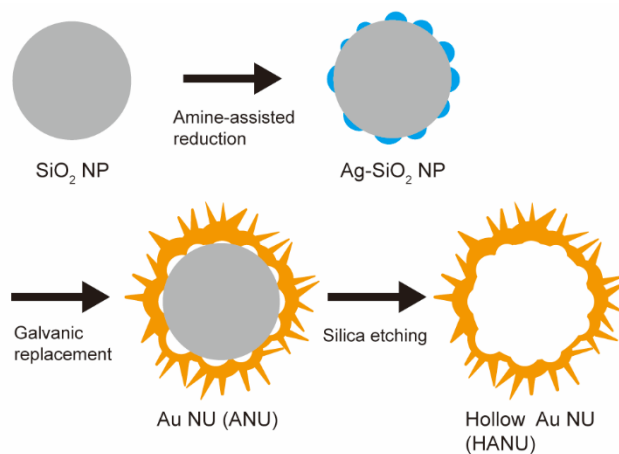
Figure 4-1. Schematic illustration for the fabrication of HANU.

Herein, we have prepared genuinely hollow Au nanourchins (HANUs) using SiO_2 NPs as hard templates. These templates are advantageous because of diverse reasons including their narrow size distribution, availability in large amounts with wide ranges of sizes, and simplicity of their synthesis using the well-known formulation.[19,23,29] Figure 4-1 illustrates the synthetic procedure of HANUs. We fabricated Ag-SiO_2 NPs via oleylamine-assisted reduction.[23,24] Next, the Au nanourchins (ANUs) were synthesized via a seed-mediated growth route using DOPA as not only a reductant but also a capping agent.[27,30] As silica cores were etched with HF*(aq)*,[31] ANUs were transformed into HANUs. Measuring the cross-sections of HANUs, we have found that HANUs have well-defined hollow morphologies arising from hard-template SiO_2 NPs. Compared with previously reported NUs prepared via DOPA-mediated reduction, HANUs contain a very small amount of

silver because we used very tiny silver seeds as initiation sites for galvanic replacement. HANUs reveal high SERS enhancement for the determination of rhodamine 6G (R6G) and a substantial photothermal effect under weak illumination of a Xe lamp.

4.3. Experimental section

4.3.1. Materials

Chemicals were used as purchased without further purification: $HAuCl_4 \cdot 3H_2O$ (*s*, ≥99.9%), $AgNO_3$ (*s*, ≥99.0%), oleylamine (technical grade, 70%), polyvinylpyrrolidone (PVP, *s*, K 30), L-3,4-dihydroxy phenylalanine (DOPA, *s*, ≥98%), HCl (*aq*, 35%), tetraethylorthosilicate (TEOS, *l*, ≥99.0%), (3-mercaptopropyl)triethoxysilane (MPTES, *l*, 80%), R6G (*s*, ≥82%) from Sigma Aldrich; NH_4OH (*aq*, 25-28%), ethylene glycol, and ethanol (*l*, ≥99.8%) from Daejung Chemicals; HF (*aq*, 48.0-51.0%) from J. T. Baker. Purified water (>15 $M\Omega$ cm^{-1}) via an Elga PURELAB Option-S system has been employed in all the experiments.

4.3.2. Preparation of SiO_2 NPs

SiO_2 NPs were produced by following the Stober method.[5] 6.0 mL water was poured into 120 mL ethanol. 6.0 mL NH_4OH(*aq*) was added and then 400 μL of TEOS was added dropwise with vigorous stirring at room temperature. The produced precipitate was

centrifuged (7000 rpm, 10 min), washed twice with ethanol, and then dispersed in 20 mL ethanol.

4.3.3. Preparation of Ag seeds-adsorbed SiO₂ (Ag-SiO₂) NPs

The surfaces of SiO$_2$ NPs were modified with functional sulfur groups using MPTES. 10 mL as-prepared SiO$_2$ colloid, 30 mL ethanol, 1.0 mL NH$_4$OH(aq), and 6.0 mL MPTES were mixed together, heated to 60 ºC, and stirred for 4 h. Generated sulfur-modified SiO$_2$ NPs were washed twice with ethanol by centrifugation (7000 rpm, 10 min) and redispersed in 10 mL ethanol. 6.0 mL of the sulfur-modified SiO$_2$ colloid was mixed with 45 mL of EG, followed by the addition of 12 mg of PVP. Then, 5.0 mg of AgNO$_3$ was mixed with the EG solution. A variously specific amount of oleylamine was quickly added to the reaction mixture, and the mixture was stirred for 1 h at room temperature. Finally, synthesized Ag-SiO$_2$ NPs were centrifuged (7000 rpm, 10 min), washed several times with ethanol, and then dispersed in 10 mL ethanol.

4.3.4. Preparation of hollow Au nanourchins (HANUs)

For the preparation of Au nanourchins (ANUs), 0.30 mL of 10 mM HAuCl$_4$(aq) was mixed with 2.0 mL of cold water. Then, 0.50 mL the as-synthesized Ag-SiO$_2$ colloid was added. After adding 0.30 mL of 10 mM DOPA(aq) to the solution, the mixture was gently shaken for several seconds. The color of the mixture changed from light yellow to bluish brown. After 20 min, brown suspension containing ANUs was produced. The product was

collected by centrifugation at 5000 rpm for 5 min, then washed sequentially with 0.2 M HCl(aq), 0.2 M ammonia(aq), and water. The product was then dispersed in 5.0 mL of water. To remove SiO_2 cores, 1.0 mL of 0.5% HF(aq) was added gently into 2.0 mL as-synthesized ANU colloid under stirring (~100 rpm). HANUs were washed three times with water by centrifugation (5000 rpm, 10 min) and redispersed in 4.0 mL of water.

4.3.5. Measurement of SERS and photothermal effect

The measurement procedure of SERS is similar to that of our reported paper.[31] For the measurement of a photothermal effect, 2.0 mL of the colloid of HANUs was placed in a plastic cuvette and illuminated using a Xe lamp with irradiance of 340 mW/cm^2 for 15 min. The temperature of the colloid was measured via immersing a digital thermometer. Photothermal effects of HANUs, reference NUs, and purified water were performed at the same conditions.

4.3.6. Characterization

The measurements of UV-visible absorption spectra, transmission electron microscopy (TEM) images, scanning electron microscopy (SEM) images, and Raman spectroscopic analysis were already described in detail.[31] X-ray diffraction (XRD) patterns were collected using a Bruker New D8 advanced diffractometer with Cu-K$_\alpha$ radiation. A focused ion beam (FIB) was applied with a Carl Zeiss AURIGA apparatus to mill the assembly of NPs. A JEOL JEM-2100F microscope operating at 200 kV was employed to acquire high

angle annular dark field-scanning transmission electron microscopy (HAADF-STEM) images and energy dispersive X-ray (EDX) elemental profiles. X-ray photoelectron spectroscopy (XPS) spectra were obtained with a KRATOS AXIS-HSi spectrometer using Al-K$_\alpha$ radiation and the measured binding energies were calibrated with the C 1s peak at 284.5 eV of contaminated carbon.

4.4.   Results and discussion

Ag-SiO$_2$ NPs, starting materials to fabricate HANUs, were synthesized via oleylamine-assisted reduction. Yang *et al.*[24] reported a facile synthesis of Ag nanoshells via alkylamine-assisted reduction. The rapid growth was attributed to a decrease in the reduction potential of Ag$^+$ in ethylene glycol (EG) through the formation of a Ag/EG complex; it was easy for Ag$^+$ to be reduced by an alkylamine even at room temperature. However, it was difficult to scoop up a precisely desired amount of a reductant because some alkylamines are sticky and solid at room temperature. Thus, instead of an alkylamine, we have used oleylamine, which is liquid at room temperature. This has simplified the washing procedure after the chemical synthesis of NPs, supporting that oleylamine is a well-known capping agent for synthesises of nanomaterials.[32] The TEM images of Figure 4-2 and the UV-visible absorption spectra of Figure 4-3 reveal that Ag nanoshells could be synthesized as the concentration of oleylamine increased from 1.1 to 3.2 µM.

However, completely closed Ag nanoshells were not synthesized because of the steric hindrance of oleylamine (Figure 4-4).[22]
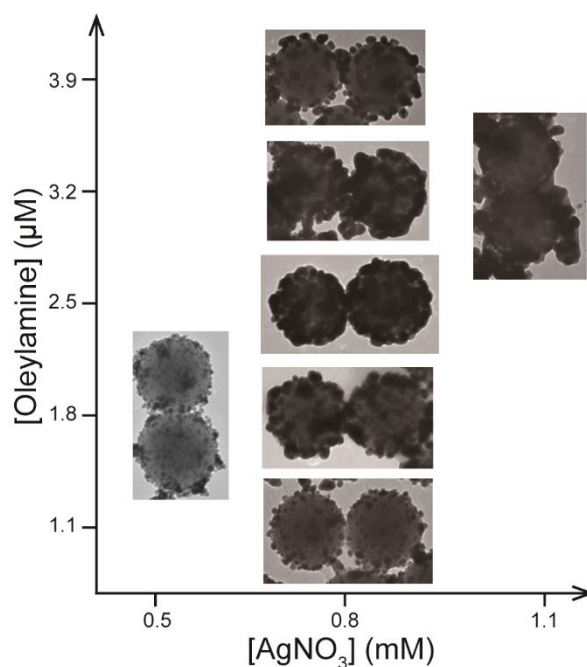
Figure 4-2. Effects of $AgNO_3$ and oleylamine concentrations on the formation of Ag-SiO_2 NPs. TEM images show the structures of Ag seeds adsorbed on SiO_2 NPs at various concentrations of $AgNO_3$ and oleylamine.
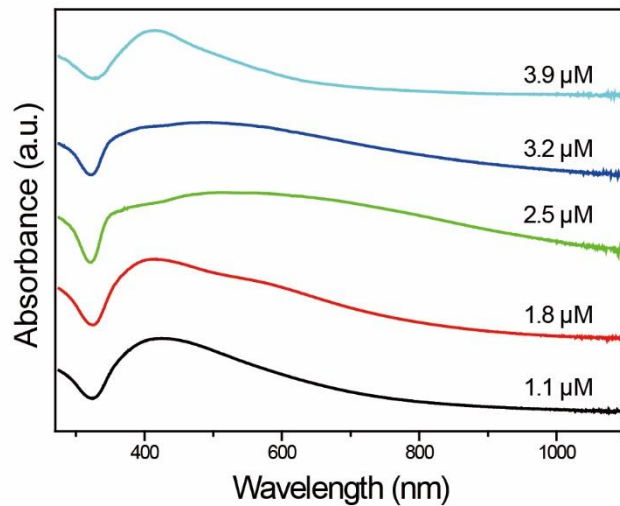
Figure 4-3. UV-vis absorbance spectra of Ag-SiO$_2$ NPs prepared at various oleylamine concentrations in ethanol.
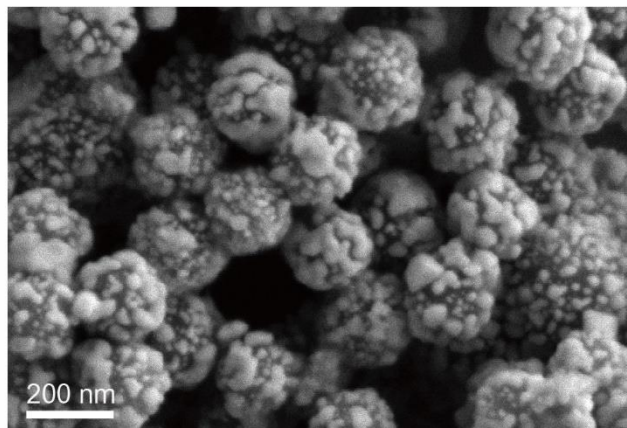

Figure 4-4. SEM image of Ag-SiO$_2$ NPs obtained with 0.8 mM AgNO$_3$ and 2.5 μM oleyamine.
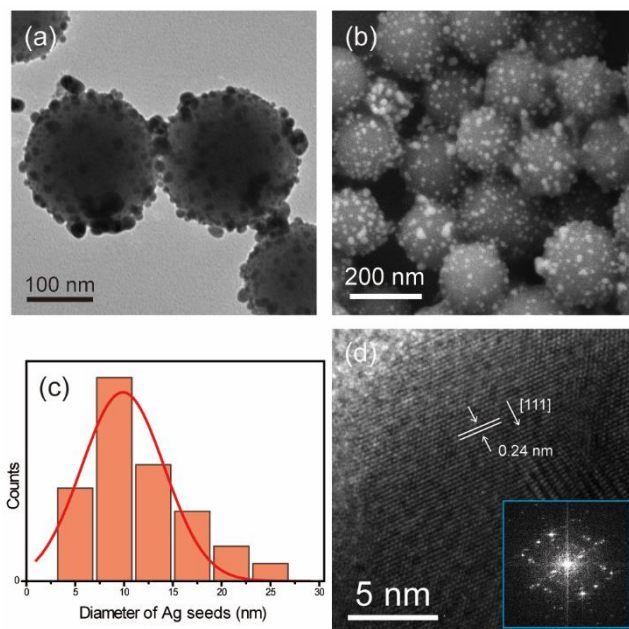
Figure 4-5. (a) TEM and (b) SEM images of Ag-SiO$_2$ NPs. (c) Ag seed-size histogram of Ag-SiO$_2$ NPs. (d) HRTEM image of Ag-SiO$_2$ NP.

We used Ag-SiO$_2$ NPs, which had been synthesized at the concentrations of 0.8 mM AgNO$_3$ and 1.1 μM oleylamine, as starting materials for the production of ANUs. Through the direct decoration of Ag seeds on the surfaces of SiO$_2$ NPs via oleylamine-assisted reduction, uniform Ag-SiO$_2$ NPs have been prepared. The TEM (Figure 4-5a) and SEM (Figure 4-5b) images of Ag-SiO$_2$ NPs reveal that countless Ag seeds with a typical diameter of 9 nm are uniformly decorated to the surfaces of SiO$_2$ NPs, implying that MPTES has enabled us to synthesize uniformly size-distributed Ag seeds on SiO$_2$ NPs

96

(Figure 4-5c). The average d-spacing value of 0.24 nm presented in the HRTEM image of Figure 4-5d corresponds well to the standard spacing between the (111) planes of the fcc silver (JCPDS-04-0783). The fast Fourier transformation pattern (inset in Figure 4-5d) indicates that the Ag seed has single crystallinity.
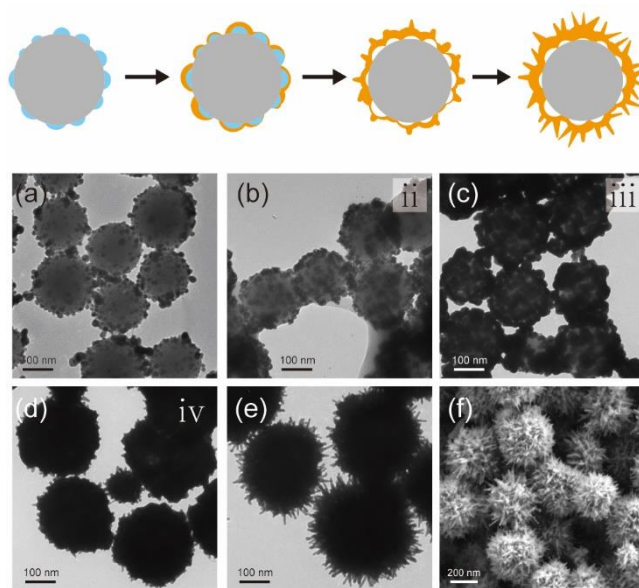
Figure 4-6. (top) Schematic illustration for the fabrication of ANU. (a-e) TEM images of (a) Ag-SiO$_2$ NPs, (b-d) progressively growing intermediates ii-iv, and (e) ANUs. (f) SEM image of ANUs.

Figure 4-6 illustrates the synthetic procedure of ANUs. It was difficult to obtain TEM images of intermediate NPs produced as a function of the reaction time because the reaction took place rapidly; the color of the reaction solution changed immediately as Au ions and DOPA were added. Therefore, the synthetic mechanism could be investigated by

measuring the TEM image of NPs synthesized with decreased amounts of the gold precursor and the reducing agent. The galvanic replacement reaction could be considered to take place at five different steps; the intermediates i, ii, iii, iv, and v can be considered as the products generated after adding 0, 1/8, 1/4, 1/2, and 1, respectively, of the stoichiometric amounts of the gold precursor and the reducing agent. The DOPA-mediated reduction of gold ions took place progressively to produce gold shell morphologies (Figure 4-6). Produced Ag/Au alloy nanostructures have nanobump morphologies because the galvanic replacement took place at individual Ag seeds on SiO_2 NP surfaces.[7,33] As the reaction proceeded further, Ag seeds were depleted off and subsequently produced a Au NS to surround a SiO_2 nanosphere template. After numerous Au nanotips were overgrown on Au NSs, ANUs were finally generated. The TEM image of Figure 4-6e and the SEM image of Figure 4-6f show that there are lots of Au nanotips on the surfaces of ANUs. DOPA has a glue function;[34] the amine group of DOPA adsorbs to the noble-metal surface while the hydrogen boding of hydroxyl groups and the Π - Π interaction of benzene rings tend to aggregate DOPA molecules with each other. The aggregation can provide exposed spaces to allow Au ions to be deposited so that gold nanotips can be produced.[11]
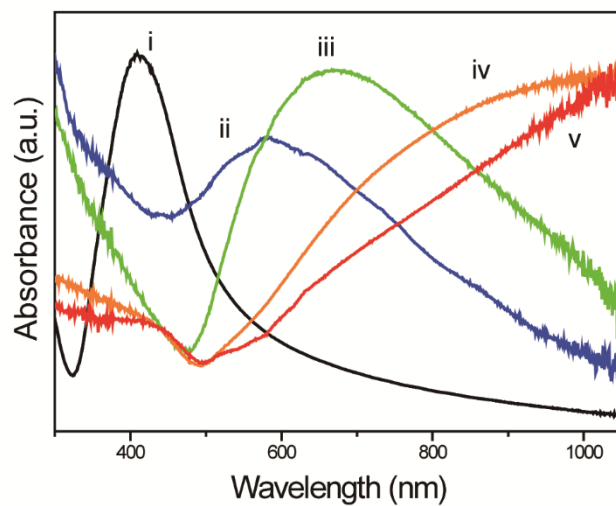
Figure 4-7. Absorbance spectra of (i) Ag-SiO$_2$ NPs, (ii-iv) progressively growing intermediates, and (v) ANUs.
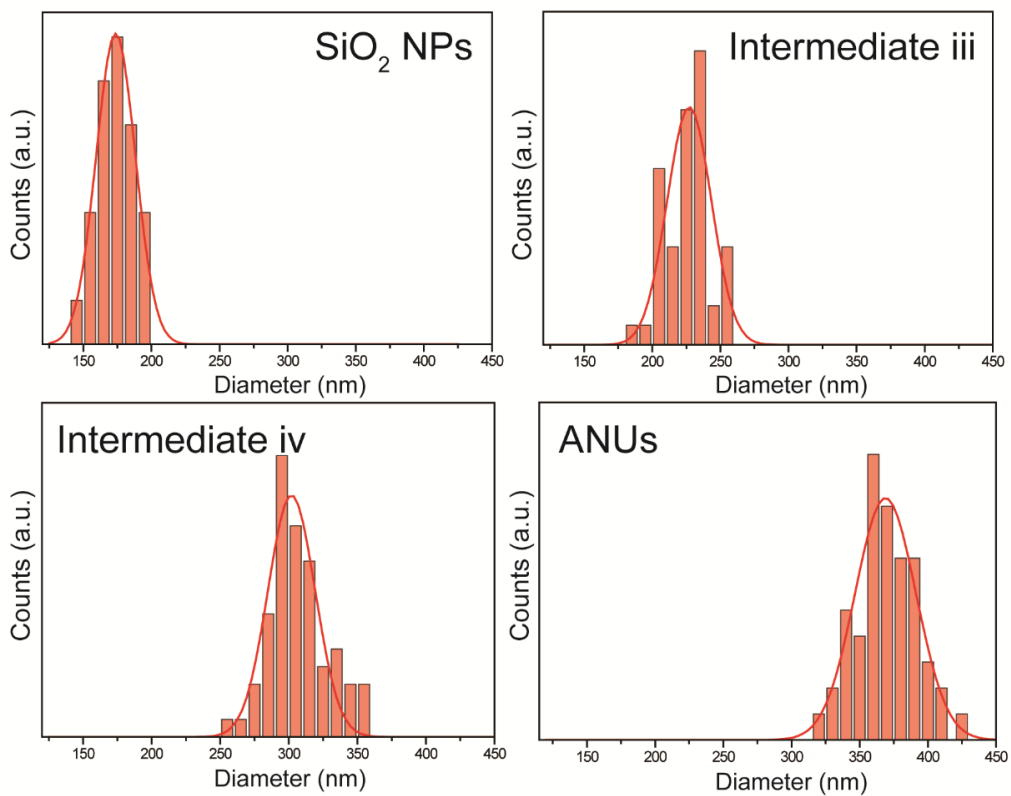
Figure 4-8. Particle-size distribution histograms of resepctively indicated samples.
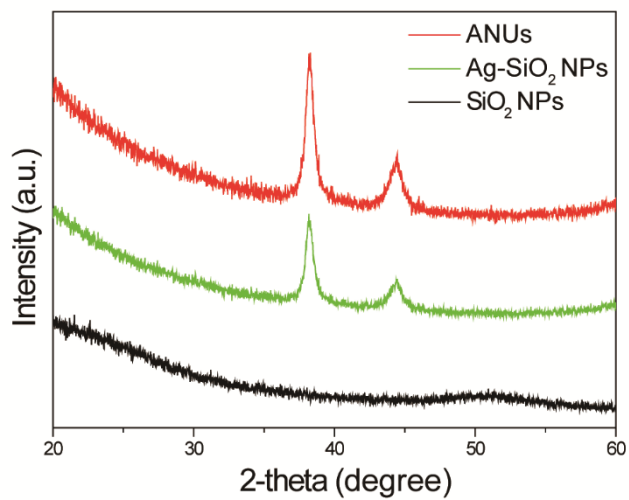
Figure 4-9. XRD data of (black) SiO_2 NPs, (green) Ag-SiO_2 NPs, and (red) ANUs.
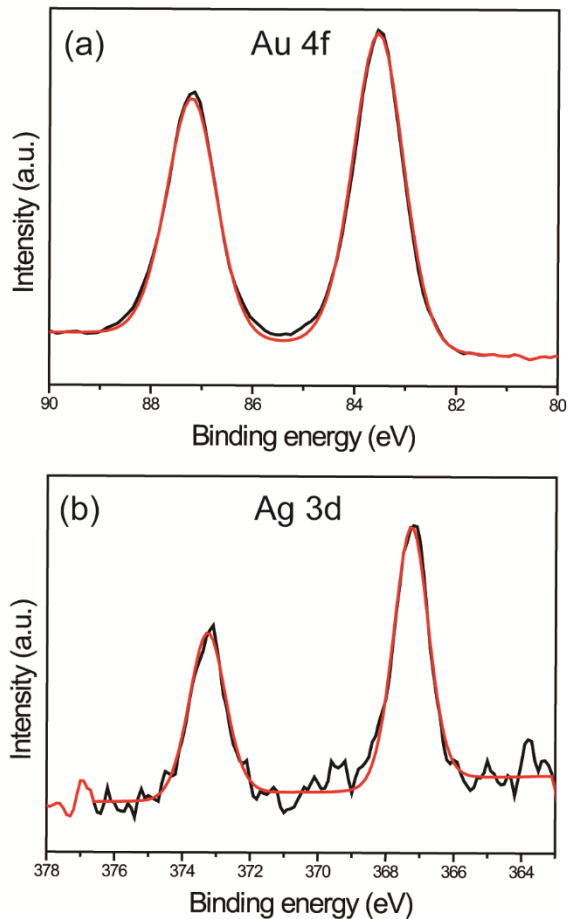
Figure 4-10. XPS spectra of ANUs in the regions of (a) Au 4f and (b) Ag 3d.

Figure 4-7 indicates that the maximum of LSPR shifted to a longer wavelength and the bandwidth of LSPR became broader as the galvanic replacement reaction proceeded progressively. The wavelength of the LSPR maximum of ANUs is longer than 1000 nm, suggesting that spiky and shell morphologies have been produced.[35] Figure 4-8 reveals that whereas the typical diameter of as-synthesized SiO_2 NPs is 173 nm, the average particle

diameter of the prepared intermediate iv is 297 nm, implying that the typical thickness of the intermediate gold nanoshells is about 60 nm. Finally, the average diameter of produced ANUs is 375 nm. Figure 4-9 shows that the XRD patterns of Ag-SiO$_2$ NPs and ANUs are very close to each other since Au and Ag metals have similar lattice constants.[30] The XRD peaks of ANUs are more intense than those of Ag-SiO$_2$ NPs because NUs are much larger than silver seeds in Ag-SiO$_2$ NPs. Any significant XRD peaks were not observed at all in amorphous SiO$_2$ NPs. The chemical states of ANUs were analyzed by measuring XPS profiles (Figure 4-10). The significant Au 4f signals at 87.2 and 83.5 eV confirm that ANUs consist of metallic Au indeed.[25,36] The Ag 3d scan of the ANUs reveals doublet peaks at 373 and 367 eV, indicating that metallic Ag also exists in ANUs. However, the low signal-to-noise ratios of Ag signals suggest that the fractional amount of Ag is much smaller than that of Au.
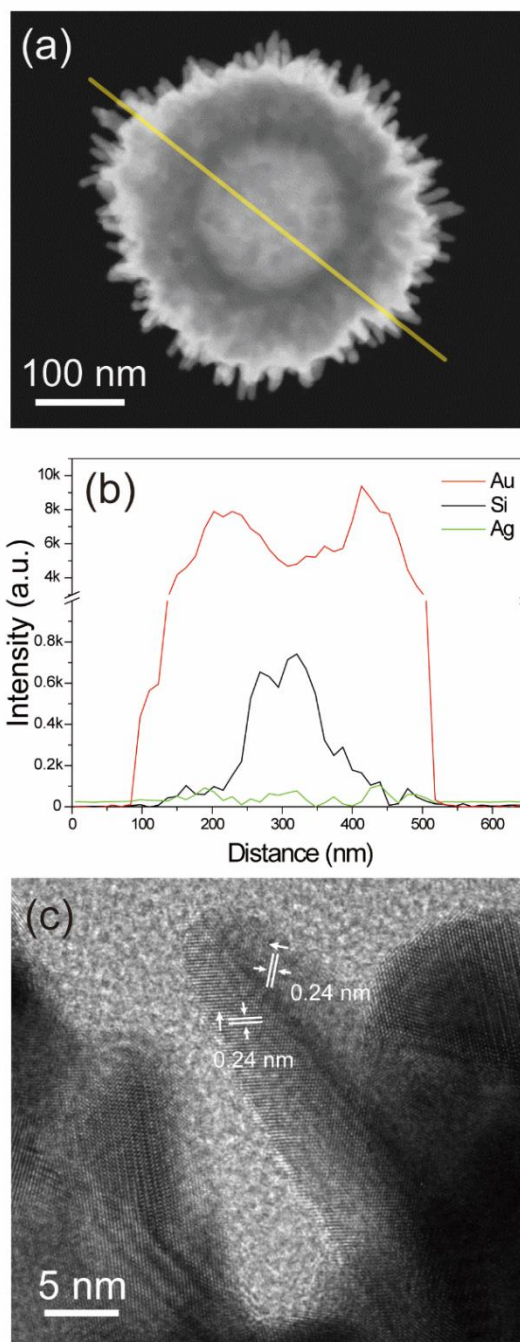
Figure 4-11. (a) HAADF-STEM image of ANU. (b) Line-scanned elemental profiles of ANUs. (c) HRTEM image of a few nanotips in ANU.

For the structural characterization of ANUs, elemental distributions have been determined by measuring a HAADF-STEM image as well as line-scanned elemental profiles. Figure 4-11a reveals that ANU has a SiO_2 core and its surface is surrounded by numerous gold nanotips. The lengths of the nanotips range from 5 to 30 nm. In particular, two sharp characteristic peaks of the Au elemental profile displayed in Figure 4-11b indicate that a Au NS encircles a SiO_2 template. Also, the Si element arising from the SiO_2 core can be seen on the central region. The very small intensity of Ag indicates that the fractional amount of Ag in ANU is negligible. The weight percentages of Au and Ag in ANU are 98% and 0.2%, respectively, indicating that the weight fraction of Ag is about 500 times smaller than that of Au because we have employed very tiny silver seeds for the initiation sites of galvanic replacement. The d-spacing value of 0.24 nm presented in the nanotip image of Figure 4-11c corresponds well to the standard spacing between the (111) planes of the fcc gold (JCPDS-04-0784). Twin planes are located in the center of a nanotip, demonstrating that our observation matches well with previous reports.[11] It has been suggested that the spiky nanotips have originated from twin planes-induced anisotropic growth.
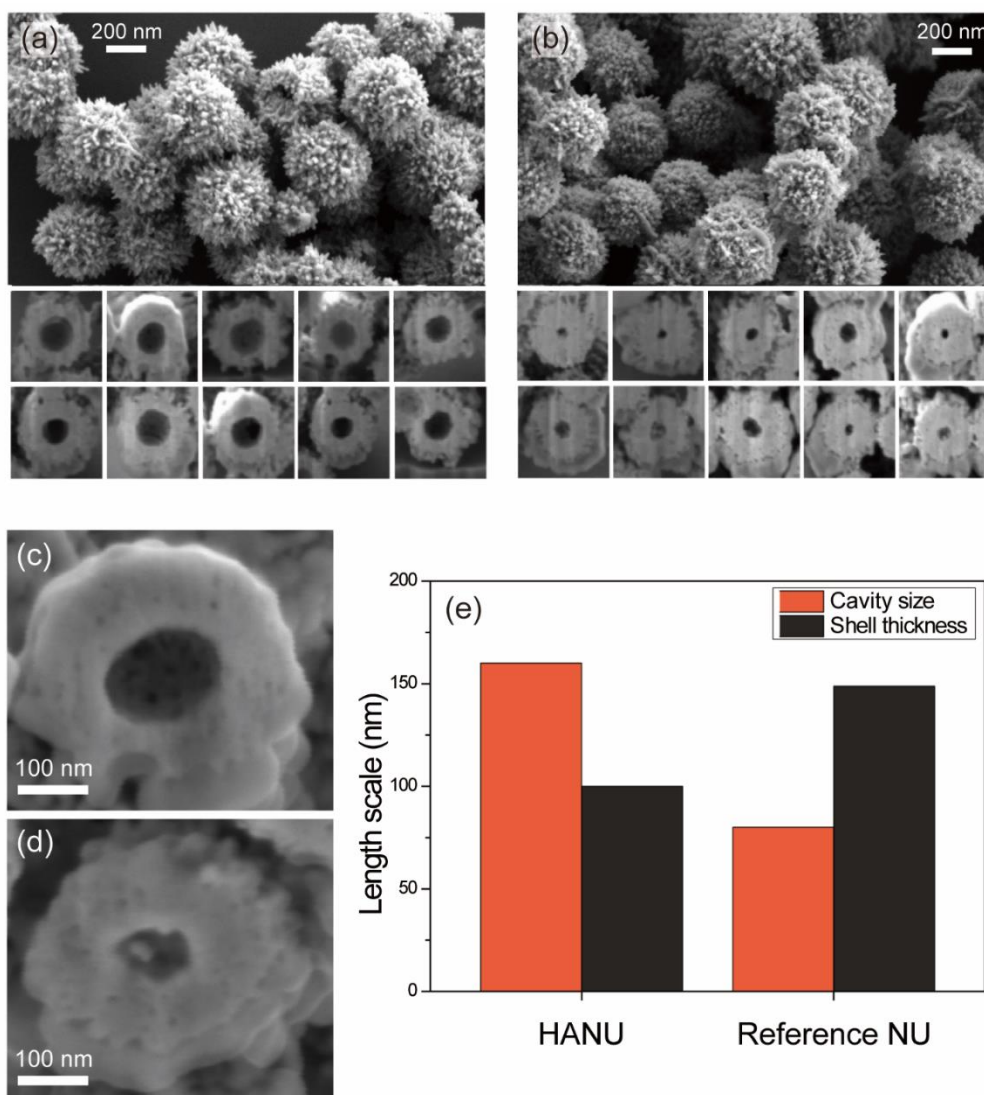
Figure 4-12. SEM images of (a,c) HANUs and (b,d) reference NUs. NP's cross sections have been observed by a FIB process. (e) Cavity diameter and shell thickness of each indicated NP obtained by a FIB process.

Silica cores were removed using HF*(aq)* to convert ANUs into hollow Au nanourchins (HANUs). The aim of this research is to fabricate functional NUs having distinctly more hollow morphologies than any published NUs. To compare the hollowness of HANUs with that of reported NUs, we have fabricated reference NUs (HAAA-NUs) having an average diameter of 370 nm.[27] For the synthesis of reference NUs, 0.30 mL of 10 mM HAuCl$_4$(*aq*) was mixed with 2.0 mL of cold water. Then, 0.20 ml of 100 nm silver seed colloid (purchased from Sigma-Aldrich) was added. After adding 0.30 mL of 10 mM DOPA(*aq*) to the solution, the mixture was gently shaken for several seconds. Then, brown suspension containing reference NUs was produced. The product was collected by centrifugation and then washed sequentially with 0.2 M HCl(*aq*), 0.2 M ammonia(*aq*), and water. Figure 4-12a and 12b shows that both HANUs and reference NUs have similar surface morphologies with numerous nanotips. For the accurate analysis of the cavities of NUs, we have monitored the cross sections of NUs milled with a focused ion beam (FIB). Only the largest cavity is meaningful because the regions where the NUs are milled are varied depending on the positions of milled NUs. HANUs have been found to have cavities of $\leq$160 nm diameters owing to the etching of SiO$_2$ templates. Considering that the average diameter of SiO$_2$ NPs is 173 nm, we suggest that the cavities are slightly smaller than the SiO$_2$ templates due to the melting and contraction of the Au nanoshells during the FIB process. Inside the cavity of Figure 4-12c, a porous nanostructure having traces of Ag seeds depleted via the galvanic replacement can be seen. The cross sections of HANUs look slightly elliptical and smooth as a strong Ga-ion beam has distorted thermally and melted original gold nanostructures having spiky nanotips. Nevertheless, the cavities of HANUs

are definitely more distinct and larger than those of reference NUs. The average cavity diameter and shell thickness of HANUs are 160 and 100 nm, respectively, while those of reference NUs are 80 and 150 nm, respectively (Figure 4-12c~12e). The volume percentages of cavities to NUs have been calculated 9% for HANUs and 1% for reference NUs. Thus, we have fabricated genuinely hollow Au nanourchins (HANUs) using SiO_2 nanospheres as hard templates. We consider that HANU can be widely used in plasmonic applications because the inner large cavity and the outer countless nanotips can induce strong near-field enhancement.
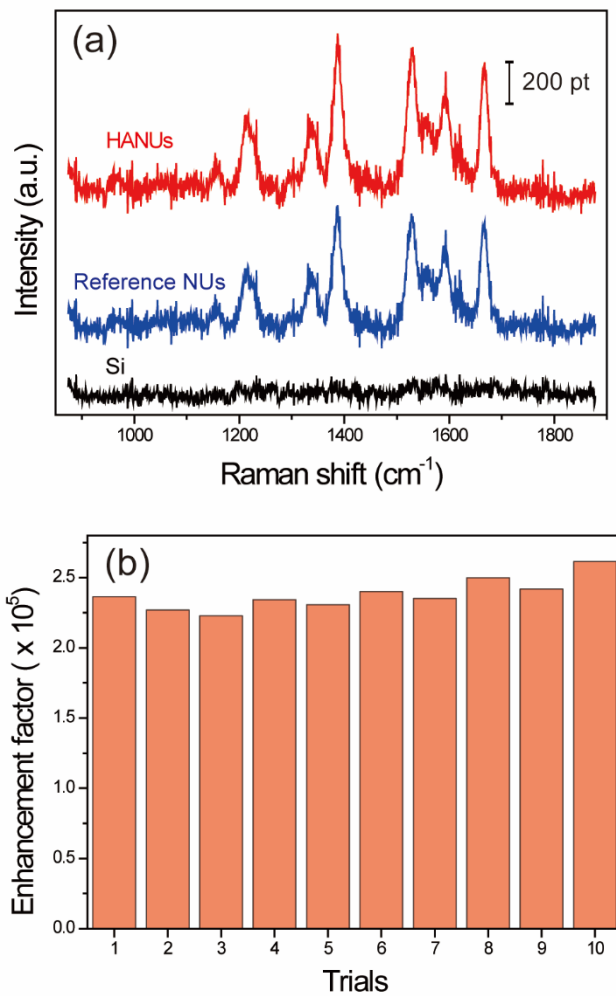
Figure 4-13. (a) SERS spectra of 10 mM R6G (in ethanol) adsorbed on HANUs, reference NUs, and Si. Note that 0.1 M R6G (in ethanol) was employed to monitor the Raman intensity of the Si substrate. (b) SERS enhancement factors of HANUs obtained by monitoring Raman intensities at 1382 cm^{-1}.

The SERS capabilities of HANUs and reference NUs were studied with R6G after excitation at 532 nm (Figure 4-13a). High-frequency bands at 1172, 1356, 1504, 1571, and 1647 cm^{-1} with large scattering cross sections have been attributed to stretching modes of aromatic benzene rings. The observed SERS frequencies and relative intensities demonstrate that the plasmonic nanotips of HANUs perturb the vibrational transitions of R6G. Additional hot spots could be created via interparticle assemblies, which were greatly beneficial to improve the uniformity and reproducibility of SERS signals.[27] SERS enhancement factors obtained by measuring relative Raman signals were 2.4 x 10^5 for HANUs and 1.7 x 10^5 for reference NUs. The SERS efficiency of HANUs was 30% greater than that of reference NUs. The significant SERS enhancement of HANUs has been attributed to high plasmonic properties originating from well-defined hollow morphologies confining R6G molecules as well as spiky nanotips. In addition, we have observed high SERS reproducibility by comparing Raman intensities measured at ten different spots (Figure 4-13b). The relative standard percent deviation of the measured Raman intensities has been calculated as 11%, designating that the SERS reproducibility of HANUs is outstanding.
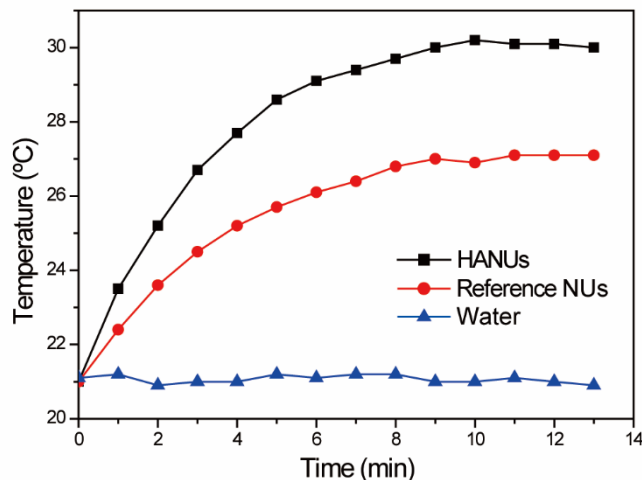
Figure 4-14. Photothermal effects of HANUs, reference NUs, and pure water.

These complex gold nanostructures can exhibit a vigorous enhancement of the electromagnetic field at nanotips and cavities, thus efficiently transducing photon energy into heat. To measure photothermal conversion properties induced by Xe-lamp light, HANUs and reference NUs were tested. As displayed in Figure 4-14, purified water did not reveal any noticeable response to the irradiation of 340 mW/cm². However, the temperature of the HANU colloid became high with the increase of irradiation time to reach 30 °C in 8 min, whereas irradiation to the reference NU colloid led to a relatively low temperature of 27 °C at 8 min. Thus, it is suggested that due to numerous sharp nanotips and hollow morphologies, HANUs can be promising nanostructures for photothermal transducers in various theragnostic applications.

111

4.5. Conclusions

We have fabricated genuinely hollow Au nanourchins (HANUs) by etching the SiO_2 cores of Au nanourchins (ANUs), which were synthesized by the galvanic replacement reaction of Ag-SiO_2 NPs using DOPA as not only a reductant but also a capping agent. The weight percentages of Au and Ag in ANU are 98% and 0.2%, respectively, because we have employed very tiny silver seeds for the initiation sites of the galvanic replacement reaction. Measuring the cross-sections of HANUs, we have found that well-defined hollow morphologies have been produced indeed. The volume percentages of cavities have been calculated as 9% for HANUs and 1% for reference NUs. HANU can be widely used in plasmonic applications because the inner large cavity and the outer countless nanotips can induce strong near-field enhancement; HANUs reveal high SERS enhancement for the detection of R6G and a substantial photothermal effect under weak illumination of a Xe lamp.

112

4.6. Acknowledgements

4.7. References

1   J. Feng and Y. Yin, Adv. Mater., 2019, 31, e1802349.

2   J. Park, T. Kwon, J. Kim, H. Jin, H. Y. Kim, B. Kim, S. H. Joo and K. Lee, Chem. Soc. Rev., 2018, 47, 8173-8202.

3   C. R. E. Prodan, N. J. Halas, P. Nordlander, Science, 2003, 302, 419.

4   A. Genç, J. Patarroyo, J. Sancho-Parramon, R. Arenal, M. Duchamp, E. E. Gonzalez, L. Henrard, N. G. Bastús, R. E. Dunin-Borkowski, V. F. Puntes and J. Arbiol, ACS Photonics, 2016, 3, 770-779.

5   T. H. Park and D. J. Jang, Nanoscale, 2018, 10, 20108-20112.

6   W. Xiong, D. Sikdar, L. W. Yap, P. Guo, M. Premaratne, X. Li and W. Cheng, Nano Research, 2016, 9, 415-423.

7   A.-A. El Mel, M. Chettab, E. Gautron, A. Chauvin, B. Humbert, J.-Y. Mevellec, C. Delacote, D. Thiry, N. Stephant, J. Ding, K. Du, C.-H. Choi and P.-Y. Tessier, J. Phys. Chem. C, 2016, 120, 17652-17659.

8   S. W. Chee, S. F. Tan, Z. Baraissov, M. Bosman and U. Mirsaidov, Nat. Comm., 2017, 8, 1224.

9   M. Rycenga, Z. Wang, E. Gordon, C. M. Cobley, A. G. Schwartz, C. S. Lo and Y. Xia, Angew. Chem., 2009, 48, 9924-9927.

10   Z. Y. Ong, S. Chen, E. Nabavi, A. Regoutz, D. J. Payne, D. S. Elson, D. T. Dexter, I. E. Dunlop and A. E. Porter, ACS Appl. Mater. Interfaces, 2017, 9, 39259-39270.

11   L. Yu, L. Zhang, X. Zhang, G. Dai, J. Zhang, X. Wang and H. You, ACS Appl. Energy

Mater., 2019, 3, 723-732.

12   Q. Fan, K. Liu, J. Feng, F. Wang, Z. Liu, M. Liu, Y. Yin and C. Gao, Adv. Func. Mater., 2018, 28, e1803199.

13   W. Wang, Y. Pang, J. Yan, G. Wang, H. Suo, C. Zhao and S. Xing, Gold Bullet., 2012, 45, 91-98.

14   Y. Xia, Z. Gao, X. Liao, C. Pan, Y. Zhang and X. Feng, CrystEngComm, 2017, 19, 6547-6555.

15   A. J. Blanch, M. Doblinger and J. Rodriguez-Fernandez, Small, 2015, 11, 4550-4559.

16   M. N. Sanz-Ortiz, K. Sentosun, S. Bals and L. M. Liz-Marzan, ACS Nano, 2015, 9, 10489-10497.

17   X. Shi, N. Coca-Lopez, J. Janik and A. Hartschuh, Chem. Rev., 2017, 117, 4945-4960.

18   R. Alvarez-Puebla, L. M. Liz-Marzán and F. J. García de Abajo, J. Phys. Chem. Lett., 2010, 1, 2428-2434.

19   B. L. Sanchez-Gaytan, P. Swanglap, T. J. Lamkin, R. J. Hickey, Z. Fakhraai, S. Link and S.-J. Park, J. Phys. Chem. C, 2012, 116, 10318-10324.

20   J. Morla-Folch, L. Guerrini, N. Pazos-Perez, R. Arenal and R. A. Alvarez-Puebla, ACS Photonics, 2014, 1, 1237-1244.

21   D. Joseph, R. Baskaran, S. G. Yang, Y. S. Huh and Y. K. Han, J. Col. Inter. Sci., 2019, 542, 308-316.

22   M. G. Cha, H. Kang, Y. S. Choi, Y. Cho, M. Lee, H. Y. Lee, Y. S. Lee and D. H. Jeong, ACS Appl. Mater. Interfaces, 2019, 11, 8374-8381.

23   H. Chang, H. Kang, J. K. Yang, A. Jo, H. Y. Lee, Y. S. Lee and D. H. Jeong, ACS Appl. Mater. Interfaces, 2014, 6, 11859-11863.

24   J. K. Yang, H. Kang, H. Lee, A. Jo, S. Jeong, S. J. Jeon, H. I. Kim, H. Y. Lee, D. H. Jeong, J. H. Kim and Y. S. Lee, ACS Appl. Mater. Interfaces, 2014, 6, 12541-12549.

25   H. You, F. Zhang, Z. Liu and J. Fang, ACS Catal., 2014, 4, 2829-2835.

26   S.-Y. Ding, J. Yi, J.-F. Li, R. Panneerselvam, B. Ren, D.-Y. Wu and Z.-Q. Tian, Nat. Rev. Mater., 2016, 1, 1-16.

27   Z. Y. Zhen Liu, Bo Peng, Cuong Cao, Chao Zhang, Hongjun You, Qihua Xiong, Zhiyuan Li, and Jixiang Fang, Adv. Mater., 2014, 26, 2431-2439.

28   Z. Liu, L. Cheng, L. Zhang, Z. Yang, Z. Liu and J. Fang, Biomaterials, 2014, 35, 4099-4107.

29   A. B. Serrano-Montes, J. Langer, M. Henriksen-Lacey, D. Jimenez de Aberasturi, D. M. Solís, J. M. Taboada, F. Obelleiro, K. Sentosun, S. Bals, A. Bekdemir, F. Stellacci and L. M. Liz-Marzán, J. Phys. Chem. C, 2016, 120, 20860-20868.

30   F. Xu, K. Cui, Y. Sun, C. Guo, Z. Liu, Y. Zhang, Y. Shi and Z. Li, Talanta, 2010, 82, 1845-1852.

31   J. K. Kim and D.-J. Jang, New J. Chem., 2019, 43, 9732-9739.

32   M. Vara, M. Chi and Y. Xia, ChemNanoMat, 2016, 2, 873-878.

33   H. L. Tae-Hyeon Park, Jaewon Lee and Du-Jeon Jang, RSC Adv., 2017, 7, 7718-7724.

34   Z. Liu, F. Zhang, Z. Yang, H. You, C. Tian, Z. Li and J. Fang, J. Mater. Chem. C, 2013, 1, 5567-5576.

35   H. N. Xie, I. A. Larmour, Y. C. Chen, A. W. Wark, V. Tileli, D. W. McComb, K. Faulds and D. Graham, Nanoscale, 2013, 5, 765-771.

36   S. Pedireddy, A. Li, M. Bosman, I. Y. Phang, S. Li and X. Y. Ling, J. Phys. Chem. C, 2013, 117, 16640-16649.

Chapter 5. Fabrication of plasmonic silver nanoparticle arrays by laser-induced dewetting of commercial silver paste

5.1. Abstract

Highly dense plasmonic silver nanoparticle (NP) arrays have been fabricated by laser-induced dewetting of commercially available silver paste as a starting bulk material. Laser-irradiation criteria for the laser melting, dewetting, and ablation of silver paste films have been determined in order to understand the optimal conditions of laser fabrication. The first laser-scan mode has produced unprecedented intermediate structures, so called laser-induced fine silver nanostructures (LIFSNs) while the second laser-scan mode has transformed LIFSNs into plasmonic silver NP arrays via the dewetting of the priorly formed nanostructures. The laser-induced fabrication of silver NP arrays has been found to be very sensitive to distance from secondly irradiated laser pulses, suggesting that the fine control of laser intensity is very important. Silver NP arrays of sub-100 nm diameters with narrow size distribution have been fabricated well at a laser scanning rate of ≥ 50 μm/s. As-prepared silver NP arrays have generated numerous hot spots to show highly strong surface-enhanced Raman scattering signals; the Raman enhancement factor of silver NP arrays for rhodamine 6G has been found as 1.2×10^6. Overall, our fabrication method of plasmonic silver NP arrays via laser-induced dewetting is facile, scalable, and reproducible.

5.2. Introduction

Plasmonic noble-metal nanoparticles (NPs) exhibit unique optical properties when their surface plasmon resonance (SPR) is excited, concentrating and enhancing an incident electromagnetic (EM) field.[1] This 'hot-spot' theory extensively contributes to the highly sensitive spectroscopic techniques of biochemical molecules such as metal-enhanced fluorescence (MEF) or surface-enhanced Raman scattering (SERS).[2-5] SERS is a powerful tool that provides a fingerprint on the composition of analytes through Raman scattering that is highly enhanced by the EM field for molecules adsorbed to hot spots on plasmonic substrates. Some research groups produced hot spots by dropping a noble-metal NP colloid on a substrate although the locations of the hot spots were relatively sparse.[1,6,7] Thus, it is still ambiguous to fabricate a SERS-active substrate with high sensitivity and good signal reproducibility in a large area using a metal colloid.

Some research groups have reported facile and reliable attempts to fabricate certain noble-metal nanostructures on a substrate with high hot-spot density.[8-12,50] Noble metals are considered to be hard materials having melting points around 1000 ºC. Therefore, the common method used to build noble-metal nanostructures is e-beam lithography, which etches metals with an electron beam, making it possible to produce uniform and functional plasmonic nanostructures.[13] However, this technique has various disadvantages: high cost, harsh conditions (high temperature and high vacuum), time consumption, and complex fabrication processes. One of the alternative methods for producing plasmonic

nanostructures is laser-induced melting and dewetting via laser-direct-writing (LDW) processing.[14-17] Dewetting is a spontaneous physical phenomenon that describes the rupture of a thin film on a substrate as well as the formation of discrete NPs or other nanostructures.[18] The overall driving force for dewetting is the minimization of the surface free energy of the metal film at the metal-substrate interface.[19] So far, researches of laser-induced dewetting have usually been performed using ultrashort laser sources such a femtosecond laser and relatively thin (<0.5 μm) noble-metal films. While Tsai et al.[16] have reported the fast fabrication of silver aggregates by irradiating femtosecond laser pulses to a AgO$_x$ thin film, Ionin et al.[15] have also studied the femtosecond-laser fabrication of self-organized plasmonic nanotextures on thin silver films. The reason for using an ultrashort laser source is that the heat-affected zone (HAZ) has a limited area because the surface treatment is neat and because the generation of byproducts such as metal debris is diminutive due to nonthermal melting via electron excitation.[20,21] During a femtosecond pulse width, only the surface lattice is heated so the shape and size of a metal microstructure are kept nearly unchanged. Meanwhile, for a nanosecond pulse, laser thermal effect is dominant compared to nonthermal melting. Because HAZ is broad, nanosecond-laser melting and dewetting can lead to an enormous structural change in a starting metal material. From an economic point of view, the fabrication of metallic microstructures using a cost-effective nanosecond-laser process is increasingly important because the price of a femtosecond laser is higher by an order of magnitude than that of a nanosecond laser. Therefore, nanosecond-laser processing is practical for the production of plasmonic NP arrays because drastic structural changes take place in a bulk noble metal.

There is a lack of researches on the fabrication of plasmonic NP arrays on a relatively thick (>1 μm) or rough bulk noble metal via laser irradiation. Diverse researches have been reported on sputtered or thermally evaporated metal thin films as starting materials.[22-26] It is facile to fabricate plasmonic NP arrays and to observe a phenomenon on the surface of a thin film because the film is moderately uniform.[50] For practical applications, however, it is important to use the bulk state of a noble metal as a starting material because a bulk metal is ubiquitous and easy to handle. Also, it is simple to fabricate a large-size functional substrate using a LDW method with controlling laser repetition rates and moving translation stages finely.[15-16] Researches on the unique morphologies of noble metal nanostructures using a laser-scanning method have attracted a great deal of attention.[27-29] Two factors, the repetition rate and the overlap degree, can control the overall heat input into the material via a heat-accumulation effect, enabling the efficient fabrication of desired noble-metal nanostructures. Thus, the laser-scanning method has led us to fabricate noble-metal NP arrays having extremely SERS-active hot spots.
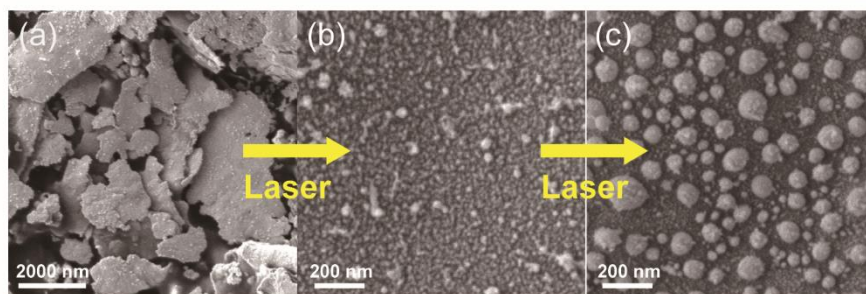
Figure 5-1. Transformation of (a) silver paste into (c) plasmonic silver NP arrays via forming (b) LIFSNs under nanosecond-laser irradiation.

In this paper, we report that highly dense silver NP arrays have been fabricated facilely by the nanosecond laser-induced dewetting of commercially available silver paste as a starting bulk material (Figure 5-1). The plasmonic arrays have been generated via forming unprecedented intermediate structures, so called laser-induced fine silver nanostructures (LIFSNs). We have also determined the detailed formation mechanism of silver NP arrays during the laser scanning. Due to the facile laser-processing method, we have achieved highly sensitive and reproducible SERS signals of rhodamine 6G (R6G) on a centimeter-scale plasmonic substrate. Confirming the presence of hot spots arising from silver NP arrays, we will propose a facile and convenient fabrication method of sensitive SERS substrates.

5.3. Experimental section

5.3.1. Nanosecond-laser direct writing

Commercially available P-100 silver paste purchased from El-coat was used without further purification. Soda lime glass, polyethylene terephthalate (PET), and printing paper were used as substrates. The glass was cleaned sequentially with Alconox dissolved in purified water (>15 MΩ/cm), acetone, and isopropyl alcohol. A 30 μm-thick silver paste film was made by dropping and blading silver paste on the center of a glass substrate which had been already attached with 30 μm-thick Scotch tapes. The silver paste film was then placed on a PC-controlled motorized X-, Y-axis stage (SHOT-202, Sigma-Koki, 1 μm resolution). A Nd:YAG nanosecond laser (Brilliant B, Quantel, λ = 532 nm, pulse duration = 6 ns, repetition rate = 10 Hz) was used as a light source. The laser beam was focused using an f/4 spherical lens, and the spot diameter of the laser beam at the sample was 0.12 mm. All the experiments were carried out in ambient conditions.

5.3.2. Characterization

Scanning electron microscopy (SEM) images were recorded with a MERLIN compact microscope operating at 5 kV. UV/vis extinction spectra were measured with a Scinco S3100 spectrophotometer. SERS spectra were measured by using an OLYMPUS BX41 confocal microscope Raman system equipped with a 532 nm SLOC-Laser GL532RA-100 DPSS laser. Each SERS spectrum was averaged over five measurements, and the baseline was subtracted from each spectrum to eliminate background noises. The recorded spectra

were imported into an Originlab OriginPro8.5 program to facilitate data analysis. Hyperspectral SERS was measured with an epi-confocal Raman spectrometer equipped with a diode laser (λex = 671 nm, Shanghai Dream Lasers Technology), a high-NA objective lens (1.49 NA, oil-immersion type, Apo N, OLYMPUS), a nanopositioning scanner (P-545.2R7, Physik Instrumente, GmbH & Co. KG.), and a spectrometer (Shamrock 193i and iXon Ultra 888, Andor Technology).

5.3.3. SERS analysis

R6G was purchased from Sigma-Aldrich and dissolved in ethanol at various concentrations (10 nM, 0.1 μM, 1 μM, 10 μM, and 0.1 mM). 7 μL of an R6G ethanol solution was dropped on a SERS substrate and the ethanol solvent was subsequently evaporated. The SERS enhancement factor (EF) was calculated following the conventional method. [30] In the SERS measurement, 7 μL of a 0.1 mM R6G aqueous solution was dropped to form a circular spot of 12.6 mm2 on a laser processed area. In the normal Raman measurement, 7 μL of a 1 M R6G aqueous solution was dropped to form a circular spot of 28.3 mm2 on a glass substrate.

5.3.4. Finite-difference time-domain calculation

The morphologies of dewetted Ag structures were extracted from SEM images to the input file using the Image J software. To simplify the computation, the structures were assumed to be cylindrical objects with flat-top topographies. The objects were placed onto a thin Ag substrate with 100 nm thickness, and lateral positions were located so that the

spatial arrangement closely mimicked the experimental patterns. To calculate electric field distributions of each pattern, a plane wave with a wavelength of 532 nm was irradiated (normal incidence) to the sample surface. All electric field distributions were sampled from the boundary between Ag cylindrical patterns and a Ag substrate with 1 nm mesh size, and were modeled with a finite-difference time-domain method (Lumerical FDTD Solutions 8.15.736). The detail of geometrical FDTD simulation is illustrated in Figure 5-2.
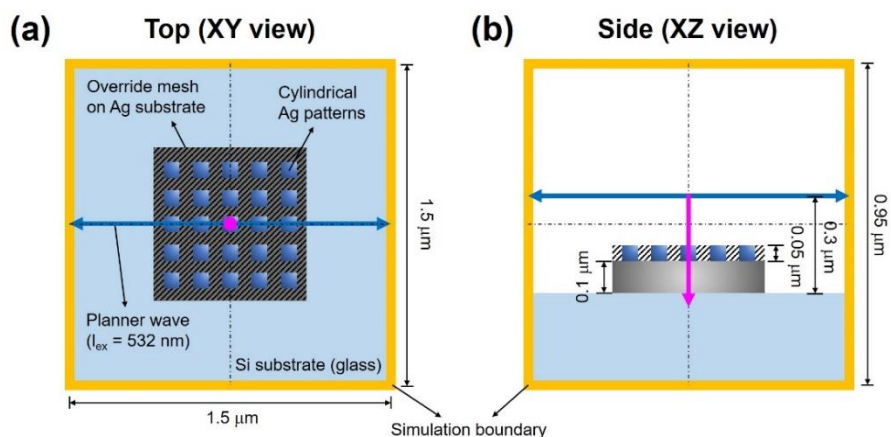

Figure 5-2. Schematic illustrations of the boundary conditions of (a) top (xy-plane) and (b) side (xz-plane) view for FDTD simulation.
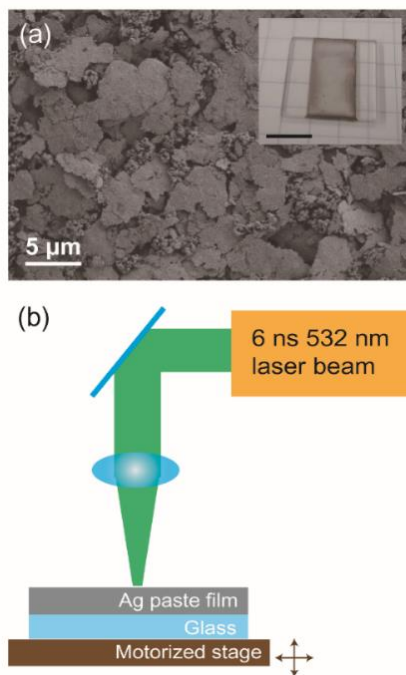
5.4. Results and discussion

Figure 5-3. (a) SEM image of silver flakes in commercial silver paste. The inset represents an optical image of a silver paste film on a glass plate (scale bar: 1 cm). (b) Schematic of laser-direct-writing (LDW) processing with a PC-driven X-, Y-axis motorized stage.

The employed starting material was silver paste, which was made by blending micro-sized silver flakes in organic solvents. The paste has been widely used in the metallization process of electrode formation in the solar cell industry,[31] and it has also been used as a silver-metal source in chemical laboratories.[32] The SEM image of Figure 5-3a shows that

125

an as-prepared silver paste film consists of plate-like silver flakes having typical sizes of a few micrometers.   Although the paste film is rough and not well-defined compared to sputtered or thermally evaporated metal thin films, it will be shown in this paper that plasmonic silver NP arrays can be produced directly from the bulk paste film via LDW processing. The experimental setup of the LDW process is illustrated in Figure 5-3b; a silver paste film is placed on a micrometer-precision motorized stage, and a 532 nm pulse beam from a 6 ns Nd:YAG laser is employed as the light source.
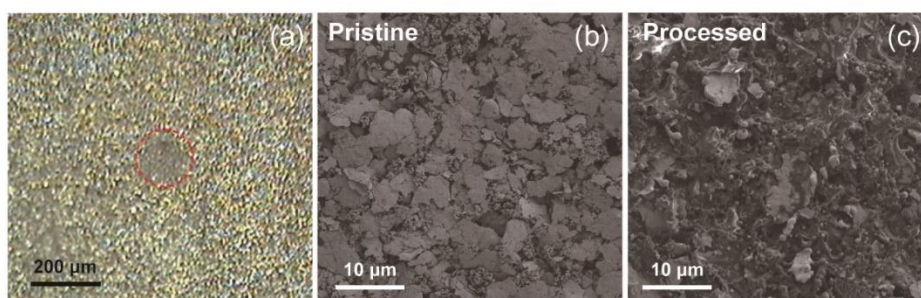

Figure 5-4. (a) Optical image of a laser-irradiated silver paste film. The red-circled region indicates the laser-processed area. SEM images of (b) a pristine region and (c) a laser-processed area in a silver paste film.

First of all, we have determined the threshold of the laser fluence necessary to melt silver flakes. The optical image of Figure 5-4a reveals a melted region that has been formed under the irradiation of a single laser pulse of 0.25 J/cm^2 (the red-circled region). While

126

Figure 5-4b indicates pristine silver flakes, Figure 5-4c shows the melted shapes of silver flakes in the laser-processed area. Micro-protruded spherical tips are created sparsely due to the high surface tension of the liquid-phase silver structures, demonstrating good agreement with the previous observations.[15,27,33] Silver flakes in the paste have micrometer sizes so their melting point is about 960 ºC, which is the melting point of bulk silver. Because the focused laser pulse could heat the irradiated area to reach the melting point, silver flakes melted to produce spherical silver particles. The organic matters in the paste film, such as toluene and resin, were evaporated during laser processing.
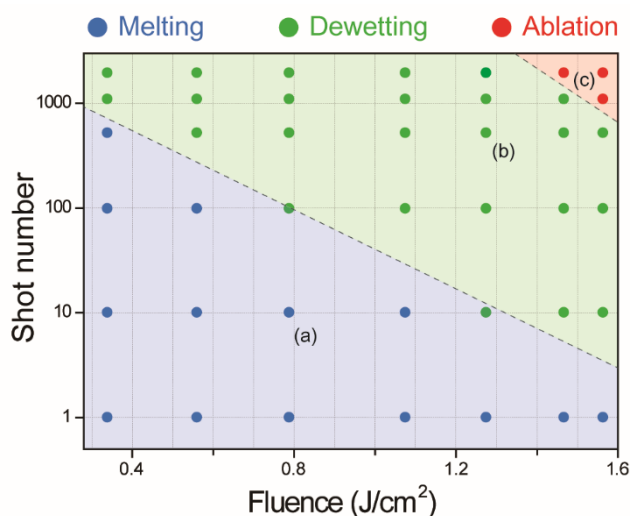

Figure 5-5. Nanosecond laser irradiation criteria for the melting, dewetting, and ablation of a silver paste film.

In order to show the optimal conditions of laser fabrication, we have presented nanosecond-laser irradiation criteria for the laser melting, dewetting, and ablation of silver

paste films in Figure 5-5. The morphologies of irradiated surfaces have been studied with variation of the laser fluence from 0.32 to 1.56 J/cm^2 and the shot number of applied pulses from 1 to 3000. The surface structural changes of the silver paste film irradiated by nanosecond-laser pulses are illustrated with a series of representative SEM images in Figure 5-6.
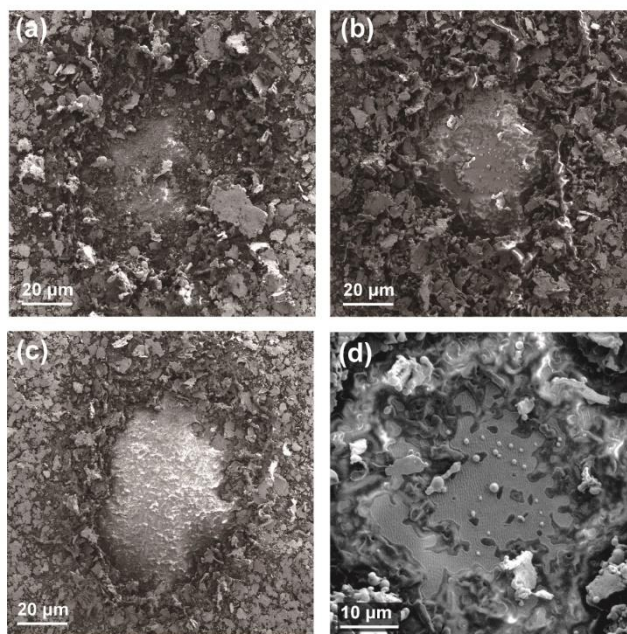

Figure 5-6. SEM images elucidating (a) laser melting, (b) laser dewetting, and (c) laser ablation, induced by nanosecond-laser irradiation. (d) Magnified SEM image of silver particles created from laser dewetting.

A dominantly occurring phenomenon via a small number of laser shots at a low fluence is the laser melting (Figure 5-6a). Compared to the laser melting, the laser dewetting is observed at a higher laser fluence and a larger number of laser shots (Figure 5-6b). The laser dewetting refers to the phenomenon that spherical silver particles are produced from a silver paste film in order to minimize the surface energy of unstable silver structures induced by the laser irradiation.[34,35] Figure 5-6d shows that spherical silver particles are formed along with the traces of melted and resolidified silver flakes. In the laser ablation region of Figure 5-6, silver particles produced via the laser melting and dewetting were evaporated by extremely high laser energy (Figure 5-6c).[25] The threshold energy of the laser dewetting is higher than that of the laser melting and lower than that of the laser ablation. Thus, it has been deduced from Figure 5-5 that the laser dewetting at the laser fluence of 1.3 J/cm^2 occurs when the shot number of applied pulses ranges from 10 to 3000. However, plasmonic silver NP arrays were not created by laser irradiation when the silver paste film was located at a fixed position. Particles in a laser-melted or laser-dewetted region show plasmonic properties but do not exhibit hot spots densely because they are located sparsely. Therefore, in order to fabricate plasmonic silver NP arrays, we have adopted a laser scanning method, where a laser is scanned at a moderate fluence of 1.3 J/cm^2 to avoid the ablation of silver particles from a silver paste film.
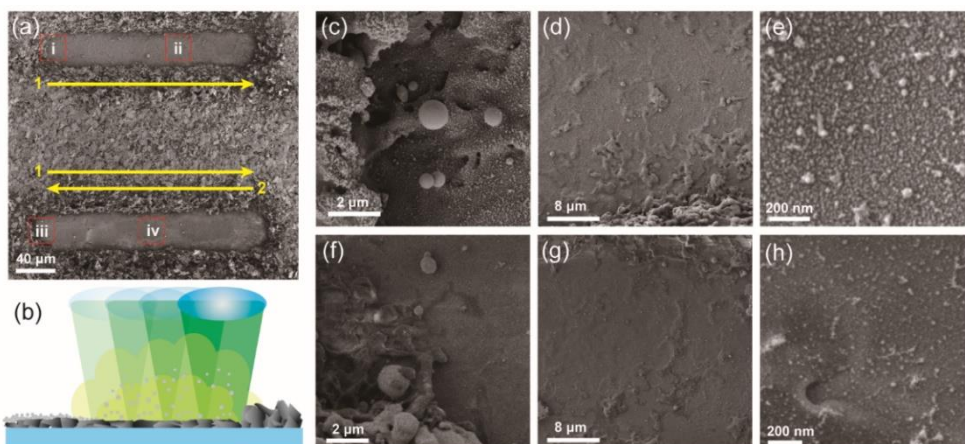
Figure 5-7. (a) SEM image of a laser-scanned silver paste film, where yellow arrows indicate scanned directions. (b) Schematic showing the laser-sanning process, where a laser beam with 6 ns pulses of 1.3 J/cm^2 was scanned on the film at a rate of 50 μm/s. SEM images of (c) the spot **i**, (d,e) the spot **ii**, (f) the spot **iii**, and (g,h) the spot **iv**.

Compared with other techniques,[36] LDW is an easy method to fabricate a large-scale functional substrate because we can 'scan' a laser beam. The nanosecond-laser scanning can reshape an as-irradiated metal structures; reshaping can be realized by the multiple irradiation of the already irradiated region.[15] We have scanned a silver paste film by moving the motorized stage horizontally in a straight line as the first laser-scan mode. Figure 5-7a indicates the SEM image of a laser-scanned silver paste film, which was scanned by a laser beam of 1.3 J/cm^2 at a rate of 50 μm/s (the upper line, scanned forward; the lower line, scanned forward and backward). Since the beam diameter is about 120 μm and the beam movement between two laser pulses is 5 μm (Figure 5-7b), the overlapping portion between two sequential laser shots is about 96%. When the laser beam was scanned

130

once in the forward direction, the melting of silver flakes took place so that a smooth silver film, rather than a rough silver flake surface, was observed. However, a close look of the smooth silver film reveals that the laser scanning led to the formation of sub-micrometer bumps, cavities, and protrusions due to the fast freezing of laser-melted silver (Figure 5-7c and 7d).[15,28,37,38] Figure 5-7e shows that the smooth silver film is covered with fine silver nanostructures, which have been formed by the melting, ablation, and resolidification of silver flakes in a silver paste film. Once a laser beam was scanned at a high fluence, silver paste went through the laser melting to produce a smooth silver film. Meanwhile, some silver materials also underwent ablation. The subsequent cooling, nucleation, and coalescence of the ablated silver led to the deposition of fine silver structures on the smooth silver film. The entire processes of ablation, cooling, and resolidification was completed within 0.1 ms and the repetition rate of the employed nanosecond laser was 10 Hz, indicating that the entire processes induced by a single laser shot were completed before the arrival of another laser shot.[21] Barcikowski et al.[26,39] have reported that the laser ablation of a metal film in water induces two different particle species: (i) primary particles of 8–10 nm in diameter, which show a smooth concentration gradient starting from the target and (ii) secondary particles of 45 nm in diameter. Also, Zhigilei et al.[40] have theoretically reported that laser pulses generate silver vapor, which falls down to form silver NPs through cooling and resolidification. Hereafter, laser-induced fine silver nanostructures, as shown in Figure 5-7e, will be designated as LIFSNs. We consider that our laser scanning method has the following three remarkable aspects. (1) Bulk and rough silver flakes were used as starting metal materials; each silver flake can act as an active

site where ablation and resolidification can take place. (2) Fabricated silver nanostructures remain unablated because the laser beam scans different regions continuously. (3) Nanosecond-laser melting and dewetting can lead to enormous structural changes in a starting metal material because HAZ is broad. LIFSNs are key intermediates in the fabrication of plasmonic NP arrays. Figure 5-7f and 7g suggests that the backward second laser scan has erased microbumps and cavities generated by the forward first laser scan to produce a smooth silver film. It is also observed that the backward laser scanning has ablated the LIFSNs of Figure 5-7e formed by the forward laser scanning (Figure 5-7h).
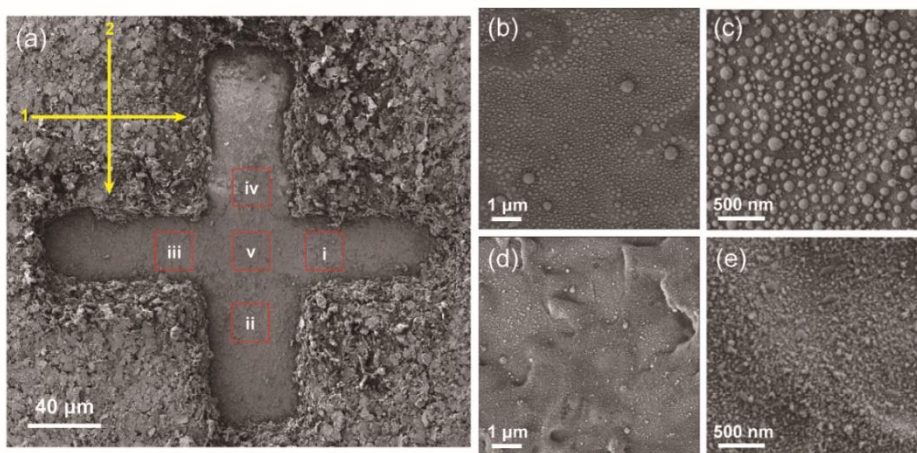
Figure 5-8. (a) SEM image of a crossly line-scanned silver paste film (yellow arrows: scan directions). (b,c) SEM image of the spot **i**. (d.e) SEM image of the spot **ii**.

We have scanned a silver paste film by moving the motorized stage perpendicularly to the already scanned line as the second laser-scan mode. Figure 5-8a indicates the SEM image of a silver paste film crossly laser-scanned with 6 ns pulses of 1.3 J/cm² at a rate of 50 μm/s. While Figure 5-8b and 8c displays the SEM image of the spot **i**, Figure 3-8d and 8e shows the SEM image of the spot **ii**. Interestingly, plasmonic silver NP arrays were generated at the spots **i** and **iii** of the laser-scanned cruciform structure whereas silver NP arrays were not produced at the spots **ii**, **iv**, and **v** (Figure 5-9).
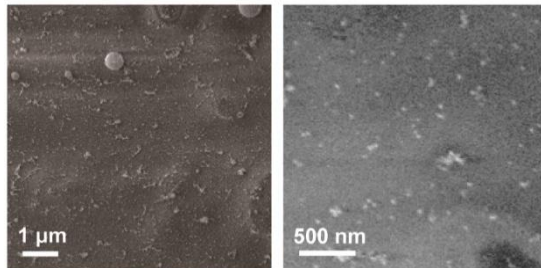
Figure 5-9. SEM images of silver nanostructures formed at the spot **v** of Figure 5-8.

In the spot **i**, typical droplet-like silver NPs were formed on the smooth silver film.[30,34,41] As a laser beam was vertically scanned over LIFSNs like the arrow 2 of Figure 5-8a, a vertical line bearing LIFSNs is newly generated (Figure 5-8d and 8e). However, the already produced LIFSNs in the spots **i** and **iii** has been transformed into plasmonic NP arrays by the second laser-induced dewetting of the priorly formed nanostructures. The cause of this phenomenon is due to the inhomogeneous energy distribution of the nanosecond laser pulse. A detailed description of the formation mechanism will be given later. The spatial distribution of the silver NP arrays is not uniform due to the inhomogeneous appearance of the microbumps and cavities generated by the first horizontal laser scan. Meanwhile, in the crossly scanned central region of the spot **v** (Figure 5-9), LIFSNs have been ablated by the second vertical laser scan.
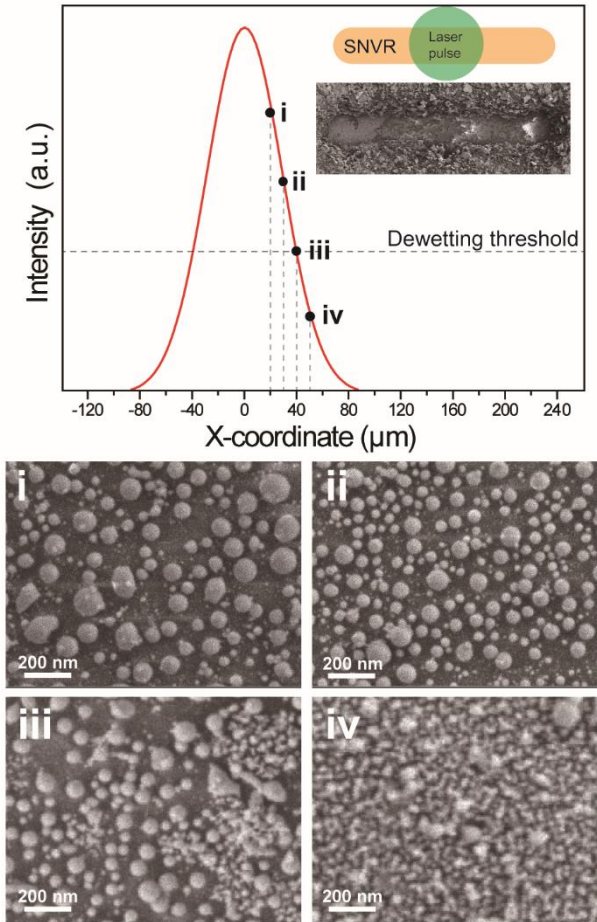
Figure 5-10. (top) Spatial energy distribution of a nanosecond laser pulse and SEM image of a silver paste film bearing LIFSNs, which was irradiated again with a single laser pulse in the middle. (bottom) SEM images measured at the respectively indicated positions.

In order to understand the formation mechanism of silver NP arrays by the second laser-scan mode, we irradiated a single laser pulse to the middle of a horizontally laser-scanned line bearing LIFSNs. Figure 5-10 indicates that silver NP arrays have been generated clearly at both spots **i** and **ii** via the laser-induced dewetting of the priorly formed LIFSNs, although silver NPs are more uniform at the spot **ii** than at the spot **i**. However, in the spot **iii** which is 40 μm apart from the center of the laser pulse, original LIFSNs, as well as newly formed silver NPs, can be observed; the boundary between original LIFSNs and silver NP arrays can be seen clearly in Figure 5-11.
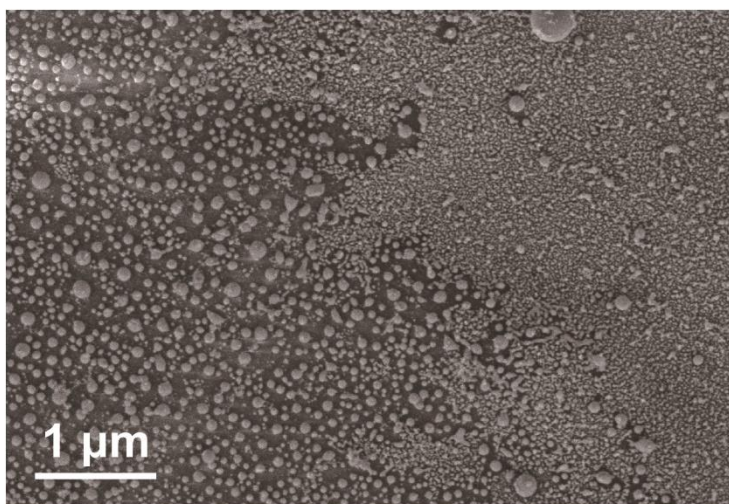

Figure 5-11. Low-magnified SEM image of silver nanostructures formed at the spot **iii** of Figure 5-10.

The clear boundary observation indicates that there exists a threshold energy of laser-induced dewetting. In the spot **iv**, silver NP arrays can hardly be observed, indicating that LIFSNs consisting of fine silver nanostructures remain intact because of insufficient laser-induced heat in this area. Thus, Figure 5-10 has indicated that the laser-induced fabrication of silver NP arrays is very sensitive to distance from the secondly irradiated laser pulse, suggesting that the fine control of laser intensity is very important for the laser fabrication. Nonetheless, we have shown that plasmonic silver NP arrays can be produced via the nanosecond-laser-induced dewetting of commercial silver paste.
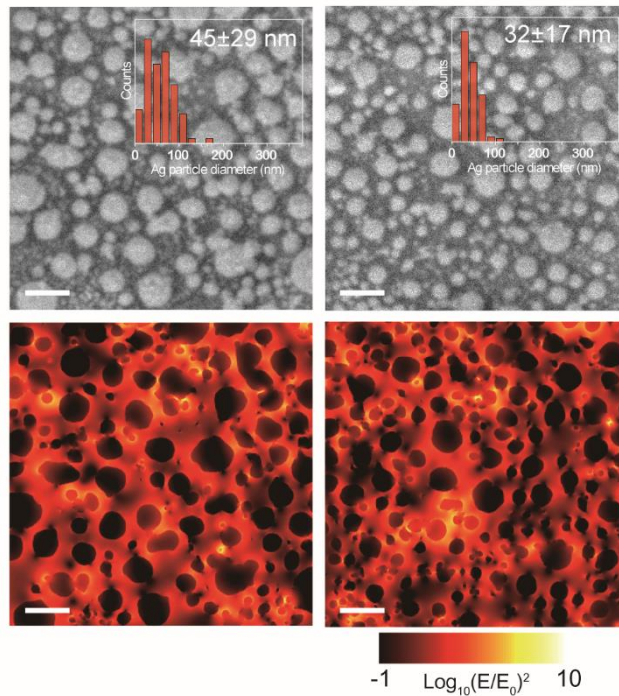
Figure 5-12. (top) SEM images with particle size-distribution histograms and (bottom) electric-field intensity distributions, calculated numerically by using the finite-difference time-domain method, of Ag NP arrays obtained by cross line scanning at rates of (left) 50 and (right) 200 μm/s. Each scale bar indicates 100 nm.
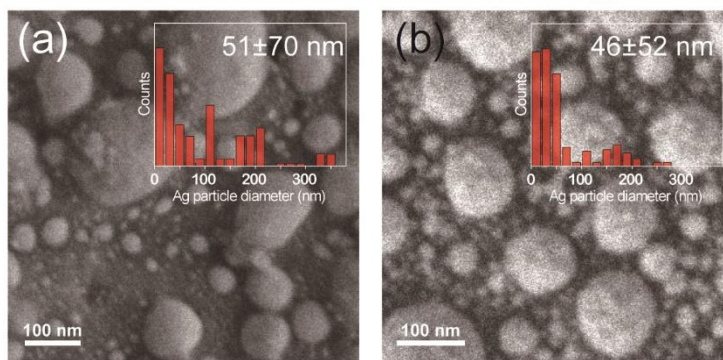
Figure 5-13. SEM images of Ag NP arrays formed by cross line scanning at rates of (a) 5 and (b) 20 μm/s. Insets: Particle size-distribution histograms of Ag NP arrays.

We have investigated the particle-size distribution of silver NP arrays formed by cross line laser scanning at various rates (Figure 5-12 and 13). Because the laser-induced dewetting is a thermodynamically spontaneous reaction, it is difficult to precisely control the diameters and gap sizes of silver NP arrays. However, Figure 5-12 and 13 display that silver NP arrays of sub-100 nm diameters with narrow size distribution can be fabricated well at a laser scanning rate of ≥50 μm/s. The average particle-diameters of silver NP arrays have been found to range from 32 to 45 nm. This is comparable to previously reported laser-processing results.[30,41] When the scanning rates were below 50 μm/s, produced silver NPs were not uniform in sizes so that the standard diameter deviation was as large as 70 nm at a scanning rate of 5 μm/s. When the scan rate was too slow, the overlapping degree between two sequential laser shots was too high to produce uniform

silver NP arrays from LIFSNs. When LIFSNs absorbed too much laser-induced heat, the mobility of silver atoms became so large that the Ostwald ripening occurred severely, producing very large particles with wide size distribution. We have also carried out the electric-field intensity simulation based on the finite-difference time-domain (FDTD) method to explore whether these silver arrays produce sufficiently enhanced and localized EM fields at hot spots.[41] The simulated results of Figure 5-12 show that the hot spots are localized in the narrow gaps of neighboring silver NPs, suggesting that strong plasmonic effects are generated between silver NPs. It is well observed that very high EM fields are concentrated on the edges of silver NPs. The simulations have confirmed that the laser-fabricated arrays can generate hot spots and produce highly enhanced SERS signals for molecules located in the nanogaps of silver NPs.
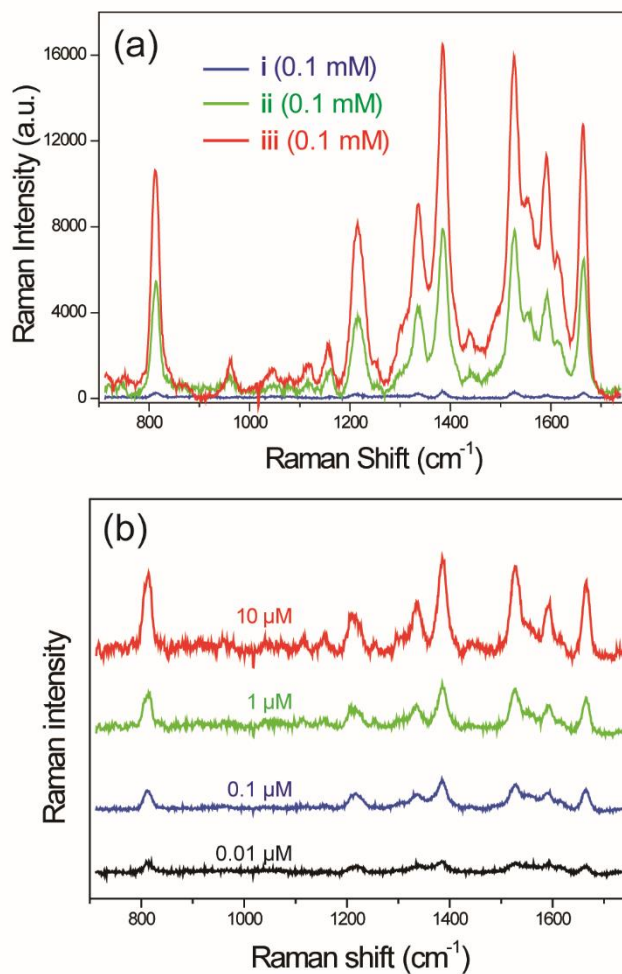
Figure 5-14. (a) Raman signals of R6G adsorbed on the spots **i**, **ii**, and **iii** of Figure 5-15. (b) Raman signals of R6G adsorbed to Ag NP arrays on the spot **iii**. The samples were excited at 532 nm, and the concentration of R6G is indicated near each spectrum.
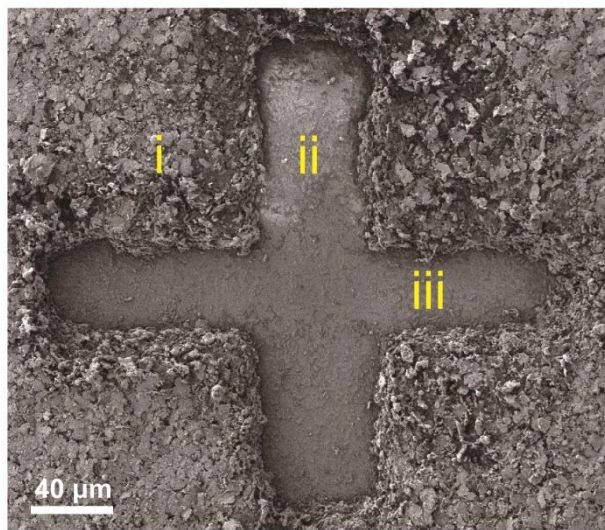
Figure 5-15. SEM image of a crossly line-scanned silver paste film.

The strong plasmonic effect of silver NP arrays is potentially useful for sensors, solar energy devices, bio-imaging, and so on.[42-44] The plasmonic performances of as-fabricated silver NP arrays have been evaluated by recording SERS spectra. Figure 5-14a shows the Raman spectra of 0.1 mM R6G on pristine silver paste, LIFSNs, and silver NP arrays. Among the examined three substrates, silver NP arrays exhibited the strongest Raman enhancement. The EF of R6G at the peak of 1381 cm^{-1} has been found as 1.2×10^6 for silver NP arrays and 5.8×10^5 for LIFSNs. The EM field enhancement is widely accepted for the mechanism of SERS;[45,46] the larger EF of SERS is due to the enhanced EM field, where the optical excitations of localized surface plasmon resonance (LSPR) in metallic nanostructures enhance the Raman signal intensity. Such an outstanding enhancement

effect is attributed to the plasmonic property of hot spots localized in the narrow gaps of neighboring silver NPs, which may effectively couple with laser light used in Raman analysis. Even if plasmonic silver NP arrays do not have uniform arrangement, they have been found to show an efficient SERS effect.[12,29] Figure 5-14b exhibits that it is possible to detect the Raman signal of R6G at a very low concentration of 10 nM when R6G molecules are adsorbed on the surfaces of silver NP arrays.
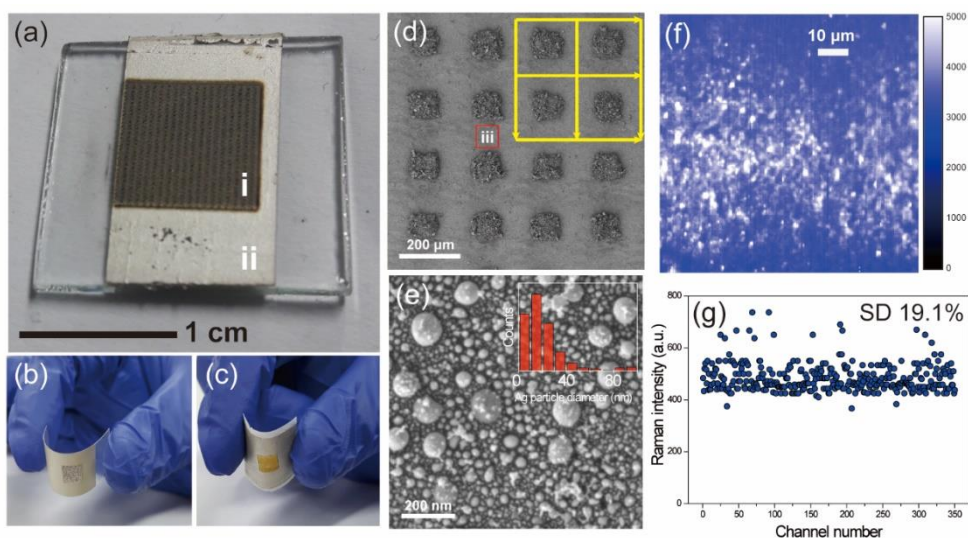
Figure 5-16. Real images of fishnet-likely scanned silver paste films on (a) a glass plate, (b) a PET sheet, and (c) a paper slip. The areas **i** and **ii** of the panel **a** indicate laser-scanned and pristine silver paste films, respectively. (d) SEM image of the laser-scanned area. (e) Magnified SEM image of the spot **iii** in the panel **d** with a size-distribution histogram. (f) Hyperspectral Raman mapping of the spot **iii**. (g) Raman intensity distribution with standard deviations of 19.1% on the spot **iii**.

The laser scanning method has the advantage of producing a large-size functional substrate at a high processing speed, compared to reported plasmonic substrate fabrication methods including conventional lithography.[42] We have scanned a silver paste film by moving the motorized stage of Figure 5-2b in a fishnet-like format. Figure 5-16a~16c shows the real optical images of fishnet-likely scanned silver paste films on a glass substrate, a PET sheet, and a paper slip. Because laser heating and subsequent cooling are completed within 0.1 ms at the surface of silver paste, the substrates such as a PET sheet and a paper slip remain intact during the laser processing. For the fast fabrication of large-size plasmonic silver NP arrays, a laser beam of 3.0 J/cm^2 was scanned on a silver paste substrate at a rate of 1.0 mm/s with +30 mm defocusing of the z-axis from the focal point. It took 10 s to scan a line of 1.0 cm, 17 min to scan 100 lines, and 34 min to scan 1.0 cm^2 (100 x 100 lines). Figure 5-16d reveals that the laser scan has melted the silver flakes to form fishnet-like smooth silver films. The average particle diameter of silver NP arrays has been found to be 32±21 nm (Figure 5-16e), which is similar to the value observed in Figure 5-8c. These silver arrays may produce sufficiently enhanced and localized EM fields at hot spots. Figure 5-16f, observed on the spot **iii** of Figure 5-16d, shows the hyperspectral Raman mapping image of R6G at 1381 cm^{-1}. The Raman mapping was scanned over an area of 0.1 x 0.1 mm^2 to display 700 x 350 data points. Frequently appearing strong Raman signals thoughout the scanned area confirm that the efficient SERS effect of the laser-scanned silver paste film is reliable and applicable. The standard deviation of Raman intensities over 350 channels is 19.1% and the entire Raman intensities change within a factor of 2, also assuring that the SERS effect is reliable and steady.

Overall, our fabrication method of plasmonic SERS substrates via laser-induced dewetting is easily scalable and reproducible.
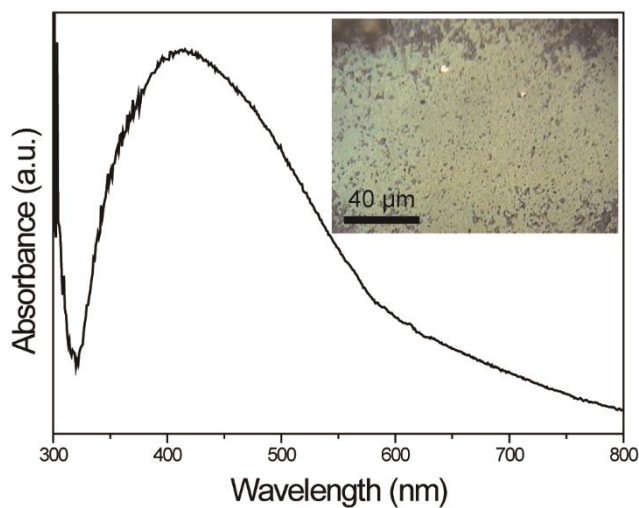
Figure 5-17. Absorption spectrum of a fishnet-likely scanned silver paste film on a glass plate (the area **i** of Figure 5-16a). Inset: optical microscope image of the paste film.

The simplest method to identify the LSPR of plasmonic substrates is a measurement of absorption spectra using a UV/vis spectrophotometer. The UV/vis absorption spectrum of a fishnet-likely scanned silver paste film in Figure 5-17 indicates that the maximum of its SPR band is located at 410 nm, suggesting that the laser-scanned silver paste film consists of plasmonic silver NPs.[2,50] Compared with the SPR bands of typical silver colloids, the observed band width is relatively broad because the size distribution of laser-induced silver NPs is wide. Thermal annealing using a furnace is usually employed for the dewetting of

noble-metal thin films.[41] However, the thermal sintering method has diverse drawbacks such as slow and nonlocal heating. We heated pristine silver paste films under a furnace at 300, 500, and 700 ºC for 1 h (Figure 5-18). Silver NP arrays have not been generated via annealing at ≤700 ºC although our nanosecond-laser-induced dewetting method has produced plasmonic silver NP arrays readily at room temperature via fast, efficient, and local heating of silver paste films.

We have compared our data with three published papers[47-49], which differ from our paper in the point that they used nm-scale thin films as a starting material. In refs. 47 and 48, a conventional thermal annealing is used to fabricate Au NP arrays or Ag nanoislands. The furnace annealing method has diverse drawbacks such as slow and nonlocal heating. The laser direct writing (LDW) technique is a promising process for the alternative low-cost annealing method. Meanwhile, in ref. 49, they developed a novel method of direct laser writing via cutting amorphous silicon square patches by femtosecond laser irradiation. They produced very uniform and large-sized crystalline Si nanoparticle arrays. However, the separation distance between particles is relatively long ($\approx$ 1 μm), and there is a limit for SERS application in the aspect that plasmonic noble metals have not been studied.
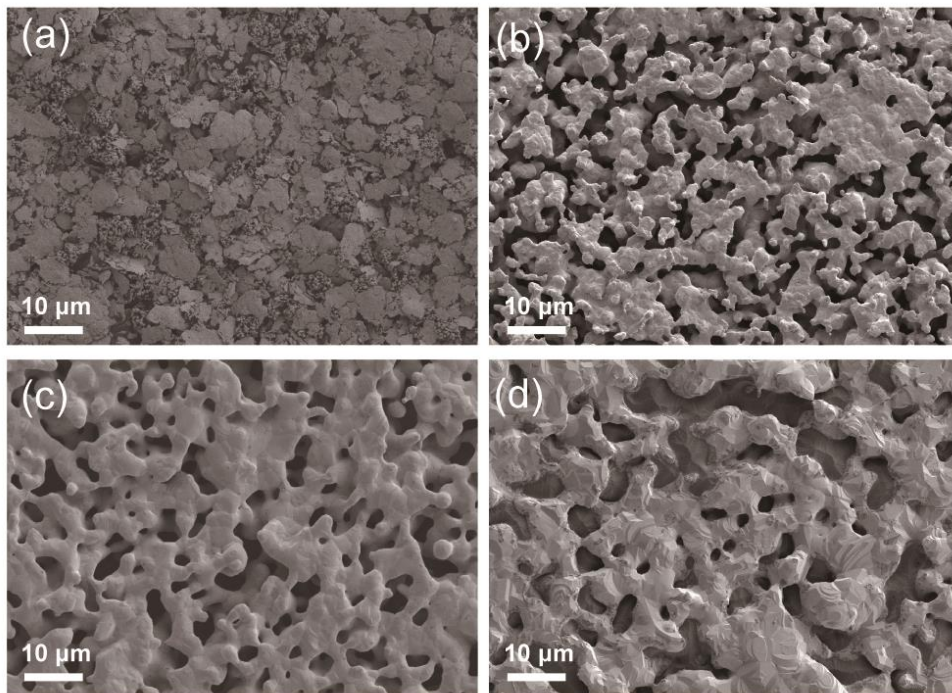
Figure 5-18. SEM images of (a) pristine and silver paste films conventionally sintered at (b) 300, (c) 500, and (d) 700 ºC.

5.5. Conclusions

Highly dense plasmonic silver NP arrays have been fabricated by laser-induced dewetting of commercially available silver paste as a starting bulk material. Laser-irradiation criteria for the laser melting, dewetting, and ablation of silver paste films have been determined in order to understand the optimal conditions of laser fabrication. The first laser-scan mode has produced LIFSNs as key intermediates in the fabrication of plasmonic arrays. Meanwhile, the second laser-scan mode has transformed LIFSNs into plasmonic silver NP arrays by the laser-induced dewetting of priorly formed fine silver nanostructures. The laser-induced fabrication of silver NP arrays has been found to be very sensitive to distance from secondly irradiated laser pulses, suggesting that the fine control of laser intensity is very important. Silver NP arrays of sub-100 nm diameters with narrow size distribution have been fabricated well at a laser scanning rate of ≥ 50 μm/s. Carrying out electric-field intensity simulation, we have confirmed that our laser-scanned substrates have generated numerous hot spots to show highly enhanced SERS signals; the EF of silver NP arrays for R6G has been found as 1.2×10^6. Overall, our fabrication method of plasmonic SERS substrates via laser-induced dewetting is facile, scalable, and reproducible.

5.6. Acknowledgements

5.7. References

1   J. Olson, S. Dominguez-Medina, A. Hoggard, L.-Y. Wang, W.-S. Chang, S. Link, Chem. Soc. Rev., 2015, 44, 40-57.

2   J.K. Kim, D.-J. Jang, J. Mate. Chem. C, 2017, 5, 6037-6046.

3   H. Jung, M. Park, M. Kang, K.-H. Jeong, Light Sci. Appl., 2016, 5, e16009.

4   P.P. Pompa, L. Martiradonna, A.D. Torre, F.D. Sala, L. Manna, M.D. Vittorio, F. Calabi, R. Cingolani, R. Rinaldi, Nat. Nanotechnol., 2006, 1, 126-130.

5   A. Kinkhabwala, Z. Yu, S. Fan, Y. Avlasevich, K. Mullen, W.E. Moerner, Nat. Photonics, 2009, 3, 654-657.

6   M.N. Sanz-Ortiz, K. Sentosun, S. Bals, L.M. Liz-Marzan, ACS Nano, 2015, 9, 10489-10497.

7   H.Y. Son, K.R. Kim, J.B. Lee, T.H.L. Kim, J. Jang, S.J. Kim, M.S. Yoon, J.W. Kim, Y.S. Nam, Sci. Rep., 2017. 7, 14728.

8   A.N. Severyukhina, B.V. Parakhonskiy, E.S. Prikhozhdenko, D.A. Gorin, G.B. Sukhorukov, H. Mohwald, A.M. Yashchenok, ACS Appl. Mater. Inter., 2015, 7, 15466-15473.

9   D. Lin, Z. Wu, S. Li, W. Zhao, C. Ma, J. Wang, Z. Jiang, Z. Zhong, Y. Zheng, X. Yang, ACS Nano, 2017, 11, 1478-1487.

10   W.J. Cho, Y. Kim, J.K. Kim, ACS Nano, 2012, 6, 249-255.

11   Y.J. Oh, K.H. Jeong, Adv. Mater., 2012, 24, 2234-2237.

12   Y. Liu, C. Deng, D. Yi, X. Wang, Y. Tang, Y. Wang, Nanoscale, 2017, 9, 15901-15910.

13   Z. Wang, Z. Dong, Y. Gu, Y.-H. Chang, L. Zhang, L.-J. Li, W. Zhao, G. Eda, W. Zhang, G. Grinblat, S.A. Maier, J.K.W. Yang, C.-W. Qiu, A.T.S. Wee, Nat. Comm., 2016, 7, 11283.

14   N. Kalfagiannis, A. Siozios, D.V. Bellas, D. Toliopoulos, L. Bowen, N. Pliatsikas, W.M. Cranton, C. Kosmidis, D.C. Koutsogeorgis, E. Lidorikis, P. Patsalas, Nanoscale, 2016, 8, 8236-8244.

15   A. Kuchmizhak, E. Pustovalov, S. Syubaev, O. Vitrik, Y. Kulchin, A. Porfirev, S. Khonina, S. Kudryashov, P. Danilov, A. Ionin, ACS Appl. Mater. Inter., 2016, 8, 24946-24955.

16   M.L. Tseng, Y.-W. Huang, M.-K. Hsiao, H. Huang, H.M. Chen, Y.L. Chen, C.H. Chu, N.-N. Chu, Y.J. He, C.M. Chang, W.C. Lin, D.-W. Huang, H.-P. Chiang, R.-S. Liu, G. Sun, D.P. Tsai, ACS Nano, 2012, 6, 5190-5197.

17   Y. Oh, M. Lee, Appl. Surf. Sci., 2017, 399, 555-564.

18   S.J. Henley, J.D. Carey, S.R.P. Silva, Phys. Rev. B, 2015, 72, 195408.

19   M. Altomare, N.T. Nguyen, P. Schmuki, Chem. Sci., 2016, 7, 6865-6886.

20   A. Hu, Y. Zhou, W.W. Duley, Open Surf. Sci. J., 2011, 3, 42-49.

21   B. Rethfeld, K. Sokolowski-tinten, D.V.D. Linde, S.I. Anisimov, Applied Physics A, 79 (2004) 767-769.

22   R. Hong, W. Shao, W. Sun, C. Deng, C. Tao, D. Zhang, Opt. Mater., 2018, 77, 198-203.

23   Y. Kojima, T. Kato, Nanotechnology, 2008, 19, 255605.

24   F. Wang, H.Y. Yu, X. Wang, J. Li, X. Sun, M. Yang, S.M. Wong, H. Zheng, J. Appl. Phys., 2010, 108, 024301.

25   A. Hu, P. Peng, H. Alarifi, X.Y. Zhang, J.Y. Guo, Y. Zhou, W.W. Duley, J. Laser Appl., 2012, 24, 042001.

26   S. Ibrahimkutty, P. Wagener, A. Menzel, A. Plech, S. Barcikowski, Appl. Phys. Lett., 2012, 101, 2019.

27   P. Fan, M. Zhong, P.S. Lin Li, C. Lin, J. Long, H. Zhang, J. Appl. Phys., 2014, 115, 124302.

28   H. He, N. Qu, Y. Zeng, Surf. Coat. Technol., 2016, 307, 898-907.

29   S.V. Makarov, V.A. Milichko, I.S. Mukhin, I.I. Shishkin, D.A. Zuev, A.M. Mozharov,

A.E. Krasnok, P.A. Belov, Laser Photonics Rev., 2016, 10, 91-99.

30   H. Zhang, L. Xu, Y. Xu, G. Huang, X. Zhao, Y. Lai, T. Shi, Sci. Rep., 2016, 6, 38337.

31   Y. Chen, D. Munoz-Martin, M. Morales, C. Molpecere, E. Sanchez-Cortezon, J. Murillo-Gutierrez, Phys. Pro., 2016, 83, 204-210.

32   D. Munoz-Martina, C.F. Braszb, Y. Chena, M. Moralesa, C.B. Arnoldb, C. Molpeceresa, Appl. Surf. Sci., 2016, 366, 389-396.

33   S.V. Starinskiy, Y.G. Shukhov, A.V. Bulgakov, Appl. Surf. Sci., 2017, 396, 1765-1774.

34   D. Qi, D. Paeng, J. Yeo, E. Kim, LetianWang, S. Chen, C.P. Grigoropoulos, Appl. Phys. Lett., 2016, 108, 211602.

35   P.Peng, A. Hu, Y. Zhou, Appl. Phys. A, 2012, 108, 685-691.

36   H. Palneedi, J.H. Park, D. Maurya, M. Peddigari, G.T. Hwang, V. Annapureddy, J.W. Kim, J.J. Choi, B.D. Hahn, S. Priya, K.J. Lee, J. Ryu, Adv. Mater., 2018, 30, e1705148.

37   S.M. Arakelyan, V.P. Veiko, S.V. Kutrovskaya, A.O. Kucherik, A.V. Osipov, T.A. Vartanyan, T.E. Itina, J. Nanopart. Res., 2016, 18, 155.

38   A.Y. Vorobyev, C. Guo, Opt. Exp., 2006, 14, 2164-2169.

39   B. Gocke, D. Zhang, S. Barcikowski, Chem. Rev., 2017, 117, 3920-4103.

40   C.Y. Shih, C. Wu, M.V. Shugaev, L.V. Zhigilei, J. Col. Inter. Sci., 2017, 489, 3-17.

41   M. Kang, S.-G. Park, K.-H. Jeong, Sci. Rep., 2015, 5, 14790.

42   K.N. Kanipe, P.P. Chidester, G.D. Stucky, M. Moskovits, ACS Nano, 2016, 10, 7566-7571.

43   S.-H. Jeong, H. Choi, J.Y. Kim, T.-W. Lee, Part. Part. Syst. Char., 2015, 32, 164-175.

44   H.A. Atwater, A. Polman, Nat. Mater., 2010, 9, 205-213.

45   S.-Y. Ding, J. Yi, J.-F. Li, R. Panneerselvam, B. Ren, D.-Y. Wu, Z.-Q. Tian, Nat. Rev. Mater., 2016, 1, 1-16.

46   S.L. Kleinman, R.R. Frontiera, A.I. Henry, J.A. Dieringer, R.P. Van Duyne, Phys. Chem. Chem. Phys., 2013, 15, 21-36.

47   T.-W. Chang, M. R. Gartia, S. Seo, A. Hsiao, G. L. Liu, Nanotechnology, 2014, 25, 145304.

48   S. Ayas, A. E. Topal, A. Cupallari, H. Guner, G. Bakan, A. Dana, ACS Photonics, 2014,

1, 1313-1321.

49   P. A. Dmitriev, S. V. Makarov, V. A. Milichko, I. S. Mukhin, A. S. Gudovskikh, A. A. Sitnikova, A. K. Samusev, A. E. Krasnok, P. A. Belov, Nanoscale, 2016, 8, 5043-5048.

50   J. Gwamuri, R. Venkatesan, M. Sadatgol, J. Mayandi, D. O. Guney, J. M. Pearce, J. Photonics Ener., 2017, 7, 037002.

Appendices

A.1. List of publications

[1] Lee, D.; **Kim, J. K.;** Jang, D.-J., Excited-state dynamics of an amphiphilic diblock copolymer self-assembled from mixed solvents. *Polymer,* **2016.**

[2] Jeong, S.; Lee, D.; **Kim, J. K.;** Jang, D.-J., A colloidal system of polythiophene-grafted edge-gold-coated silver nanoprisms with enhanced optical properties and stability. *New Journal of Chemistry,* **2017.**

[3] Lee, J.; Kim, Y.; **Kim, J. K.;** Kim, S.; Min, D.-H.; Jang, D.-J., Highly efficient photocatalytic performances of SnO_2-deposited ZnS nanorods based on interfacial charge transfer. *Applied Catalysis B: Environmental,* **2017.**

[4] **Kim, J. K.;** Jang, D.-J., Metal-enhanced fluorescence of gold nanoclusters adsorbed onto Ag@SiO_2 core-shell nanoparticle. *Journal of Materials Chemistry C,* **2017**

[5] Park, S.; Kwon, J. E.; Park, S.-Y.; Kwon, O.-H.; **Kim, J. K.;** Yoon, S.-J.; Chung, J. W.; Whang, D. R.; Park, S. K.; Lee, D. K.; Jang, D.-J.; Gierschner, J.; Park, S. Y., Crystallization-induced emission enhancement and amplified spontaneous emission from a CF_3-containing excited-state intra molecular proton transfer molecule. *Advanced Optical Materials,* **2017.**

[6] Jeong, S.; Lee, Y.; **Kim, J. K.;** Jang, D.-J.; Hong, J.-I., Non-doped thermally

activated delayed fluorescent organic light-emitting diodes using an intra-and intermolecular exciplex system with a meta-linked acridine-triazine conjugate. *Journal of Materials Chemistry C,* **2018.**

[7] **Kim, J. K.;** Jang, D.-J., Hollow and inward-bumpy gold nanoshells fabricated using expanded silica mesopores as templates. *New Journal of Chemistry,* **2019.**

[8] **Kim, J. K.;** Lee, K. S.; Park, T.-H.; Jeong, D.-W.; Kim, Z. H.; Jang, D.-J., Fabrication of plasmonic silver nanoparticle clusters using laser-induced dewetting by commercial silver paste. *Optics & Laser Technology,* **2019.**

[9] **Kim, J. K.;** Park, T.-H.; Jang, D.-J., Surface-enhanced Raman scattering and photothermal effect of hollow Au nanourchins with well-defined cavities. *(submitted to New J. Chem.)*

A.2. List of presentations

A.2.1. International presentations

[1] **Kim, J. K.;** Lee, D.; Jang, D.-J. "Amphiphilic Diblock Copolymer Self-Assembled from Mixed Solvent" International Conference of Composites Structure, Finland, 2016.

[2] **Kim, J. K.;** Lee, J.; Jang, D.-J. "Laser Fabrication of Ag@SiO$_2$@Ag Nano-

structures with Enhanced Catalytic Activity" Surface Plasmon Polarition 8, Taiwan, 2017.

[3] **Kim, J. K.;** Jang, D.-J. "Metal-enhanced Fluorescence of Gold Nanoclusters Adsorbed to Ag@SiO$_2$ Core-Shell Nanocomposites" Nanosmat: Asia, Hongkong, 2017.

A.2.2. Domestic presentations

[1] **Kim, J. K.;** Lee, D.; Jang, D.-J. "Fabrication and Characterization of Hybrid J-Aggregate Nanofibers Consisting of Poly(3-hexylthiophene)-Coated Gold Nanoparticles" The 115th National Meeting of the Korean Chemical Society, Goyang, Korea (2015).

[2] **Kim, J. K.;** Jang, D.-J. "Excited-state dynamics amphiphilic deblock copolymer nanostructures consisting of poly(3-hexylthiophene) and poly(4-vinylpyridine)" The 116th National Meeting of the Korean Chemical Society, Daegu, Korea (2015).

[3] **Kim, J. K.;** Jang, D.-J. "Fabrication and Photocatalytic Activity of ZnS Nanobelts with Graphene Quantum Dots" The 117th National Meeting of the Korean Chemical Society, Goyang, Korea (2016).

[4] **Kim, J. K.;** Jang, D.-J. "Phototreatment of ZnS Nanobelts for Enhanced Photocatalytic Performances" The 119th National Meeting of the Korean

Chemical Society, Goyang, Korea (2017).

[5] **Kim, J. K.;** Lee, K. S.; Park, T.-H, Jeong.; D.-W.; Kim, Z. H.; Jang, D.-J. "Facile fabrication of silver nanoparticle arrays by optical-induced melting and dewetting of silver paste" The 123th National Meeting of the Korean Chemical Society, Suwon, Korea (2019).

Abstract (Korean)

독창적이고 기능적인 플라즈모닉 귀금속 나노입자의 합성과 광학적 특성에 대해 주로 연구하였다. 다양한 합성방식으로 코어쉘, 속이 빈 껍질, 나노스파이크 그리고 나노입자 어레이 구조를 합성해보았다. 분광광도계와 라만광도계, 전자현미경 등을 이용하여 제작된 나노구조물의 광학적, 구조적 특성을 연구해보았다. 귀금속 나노입자 합성방법과 플라즈모닉 공명현상을 Chapter 1에 간략히 소개하였다.

Chapter 2에서는 금 클러스터가 흡착된 Ag@SiO$_2$ 코어쉘 나노입자의 금속-증강 형광 (Metal-enhanced fluorescence, MEF)에 대해 연구하였다. 금속나노입자는 입사 광에 의해서 표면의 자유전자들이 집단적인 진동하는 표면플라즈몬공명 (surface plasmon resonance, SPR)이라는 독특한 광학적 특성을 가진다. 이러한 현상을 통해 나노입자 표면에서는 입사되는 전자기장의 세기보다 수천~수만 배 더 큰 세기로 증폭될 수 있으며, 이러한 현상을 근접장증폭이라 불리고 있다. 이러한 광학적인 기능성을 가지는 금속나노입자에 실리카 껍질을 두르면, 금속입자 표면이 보호되거나 SPR 현상을 더욱 증강시킬 수 있다. 은 나노입자는 수용액상에서 은 이온의 화학적 환원을 통해 구 형태로 합성한 다음, 실리카 물질의 전구체를 이용한 Stober method를 통해 은 나노입자 표면에 실리카 껍질을 구현하였다. TEOS 양을 달리 함에 따라 실리카 쉘 두께를 변화시켜 각기 다른 Ag@SiO$_2$ 코어쉘 나노입자를 합성한 다음, 거리-의존적인 SPR 현상을 관찰하였습니다.

보통, 나노입자는 열역학적으로 가장 안정한 구(sphere) 형태로 합성된다. 열역학적의 한계를 넘어서 좀 더 고차원적이고 기능성을 가지는 나노입자 제작에 관한 연구가 국내외 연구진에서 활발하게 진행되고 있다. 나노쉘 (nanoshell) 형태의 입자란, 실리카 같은 유전물질이 중심에 존재하고, 그 표면을 금속물질로 껍질처럼 둘러싸인 구조를 말하는데, 나노쉘입자는 구 형

태의 입자보다 SPR 현상을 더욱 강하게 발현시키고, 적외선 영역 쪽에서 광학적 활성을 보이는 고기능성 구조이다. Chapter 3에서는 이전에 보고되지 않았던 구조인, 속이 비어있고 그 안쪽에 표면에 거칠기가 있는 금 나노쉘 입자를 합성에 대해 설명하였다. 나노입자의 표면이 거칠다면, 나노미터 스케일에서 전자기장을 산란시킬 수 있으므로 SPR 효과를 더욱 증강시킬 수 있다. 속이 비어있고 안쪽의 표면이 거친 나노쉘 구조를 만들기 위해 메조포러스 (mesoporous) 실리카 나노입자를 주형으로 이용했는데, 메조포러스 실리카는 입자 내에 CTAB 분자들의 자가조립에 의해서 만들어진 공동이 무수히 존재하는 실리카 입자를 말한다. 메조포러스 실리카 공동에 표면처리를 통해서 자그마한 금 나노입자를 부착시키고, 화학적 환원법을 통해 금 나노입자들을 성장시킨다. 성장되는 금 나노입자들은 입자가 커짐에 따라 실리카 공동구조를 부분적으로 채우게 되고, 추후 실리카를 HF로 에칭함으로서 속이 비어있고 안쪽에 거친 표면을 가지는 금 나노쉘 (hollow and bumpy gold nanoshell, HBA NS) 합성할 수 있었다.

어떠한 금속 나노구조물에 나노스케일의 거칠기나 나노팁 형태를 부여하면 더욱 향상된 플라즈모닉 성질을 보일 수 있다. 음의 유전율을 가지는 귀금속 나노구조물은 입사하는 전자기장을 국부적으로 구속하는 능력이 가지게 되고, 특히나 나노팁과 같이 구조체의 곡률이 심하게 변화하는 곳은 그 효과가 더욱 증폭됩니다. Chapter 4에서는 입자 안의 cavity가 확실히 존재하고 표면에 나노팁이 무수한 입자를 합성하고자 노력하였다. SH-로 표면개질된 실리카 나노입자를 합성한 다음, 아주 작은 크기의 은 나노입자를 실리카 표면에 합성한다. 이후, 점진적인 galvanic replacement 반응을 통해서 실리카 표면 위에 금 나노팁이 무수하게 존재하는 나노성게 입자(spiky Au nanourchins, SANUs)를 합성한다. HAADF-STEM 측정방식을 통해서 SANUs 입자 중간에 실리카 입자가 확실히 보이며, galvanic replacement 반응으로 금 나노껍질이 환

원된 모습이 관찰된다. 또한 EDX line-mapping과 원소분석을 통해서, SANUs 입자는 속이 비어있고 금 성분이 98 wt%로 관찰되는 데 반해, 은 성분은 0.2 wt% 아주 극미량으로 구성되어있음을 확인하였다. 최종적으로 합성된 SANUs 입자에 HF로 실리카 성분을 녹여서 속이 비어있고 나노팁이 무성한 금 나노 성게 (hollow and spiky Au nanourchins, HSANUs)를 얻어보았다. FIB (focused-ion beam) 기법으로 그 단면을 조사하여 HSANUs 입자 안쪽에 확연한 cavity 형태를 확인하여, 중국의 연구진들에 의해 제안된 나노성게 입자의 cavity의 크기가 확연히 비교됨을 확인하였다.

레이저를 이용한 미세구조 가공기술은 레이저 빔의 고집속성 및 시공간적 정밀함으로 인해 반도체, 전자, 메카트로닉스 등의 첨단산업 분야에서 필수적인 기술로서, 신 공정 개발에 기여해왔습니다. 광열적 부작용이 적어서 마이크로-나노 급의 형상 가공이 가능한 극초단파 레이저(ultrafast laser)의 도입과 연구가 활발히 진행되고 있는데, chapter 5에서는 극초단파 레이저 광원을 사용하여 금속 나노구조를 손쉽게 제작한 연구를 설명하였다. 나노세컨드 레이저는 연속파 레이저에 비해 강한 파워를 가짐과 동시에 비교적 열적 영역 (heat-affected zone)이 넓어서 벌크물질에 극심한 형태변화를 유도할 수 있기 때문에 top-down 방식의 제작에 유리하다 판단하였습니다. 1.3 J/cm^{2}의 파워와 50 μm/s의 속도로 레이저를 십자가 형태로 스캔한 (cross-line scanning) 실버 페이스트 필름에서, 균일한 나노입자배열이 십자가의 왼쪽, 오른쪽 가지에 관찰되었고 위, 아래의 가지에서는 이전에 관찰되었던 미세하고 무수한 은 입자들이 제작되었다. 가로방향의 스캔으로 통해 미세하고 무수한 은 나노입자를 제작한 다음, 세로방향으로 스캔 할 때, 불균일한 에너지 분포 형태의 Gaussian form을 가지는 레이저 빔에 의해서 dewetting threshold를 넘어가는 공간적 영역에서는 dewetting 현상이 일어나 나노입자 배열이 제작되는 것을 발견하였다. 십자가 레이저 스캔 모드 양식의 확장으

로서, 그물모양의 레이저 스캔을 시행하면 센티미터급의 대면적의 플라즈모닉 나노구조배열을 얻을 수 있었고 강한 전자기장 증강으로 표면증강라만산란기법 (Surface-enhanced Raman scattering)을 통해서 하여금 분석하고자 하는 물질의 농도가 nM 수준으로 내려가도 충분히 검출 가능한 기능성 기판 제작에 성공하였다.